Department of Civil Engineering and Architecture

A PhD Dissertation in Geotechnical Engineering

Evaluation of rainfall-induced landslide hazards and risk assessment framework

PhD Candidate:
Karol Andrea Pinargote Mendiburo

Advisor:
Prof. Francesco Castelli

Co-Advisor:
Prof. Valentina Lentini

Enna, September 2025

National PhD Program in

Defense against natural risks and ecological transition of built environment

XXXVIII Cycle

PhD Candidate: Karol Andrea Pinargote Mendiburo

Advisors:
Prof. Francesco Castelli
University of Enna “Kore”, Department of Engineering and Architecture

Prof. Valentina Lentini
University of Enna “Kore”, Department of Engineering and Architecture

Administrative seat:
University of Catania, Department of Civil Engineering and Architecture

Affiliations:
University of Enna “Kore”, Department of Engineering and Architecture
University of Dundee, School of Science and Engineering (Visiting Researcher, 3 months)

PhD scholarship funded by the Italian Ministry of University and Research (MUR) under
PNRR – DM 351/2022

Enna, September 2025

You were created in the image and likeness of God (Genesis 1:26–27). Bees should not be able to fly, yet they do. Within you there is greater power and purpose than you can imagine, and it can only be achieved with the help of God.

Declaration

This is to certify that, except where specific reference to other investigation is made, the work described in this thesis is entirely my own work. None of this work has been previously submitted for any other degree at this or any other university.

Karol Andrea Pinargote Mendiburo (Candidate), Catania, (/ /2026)

Dr. Francesco Castelli (Supervisor), Catania, (/ /2026)

Acknowledgements

"*For from Him and through Him and for Him are all things. To Him be glory forever. Amen.*" — Romans 11:36

First and foremost, I want to give thanks to God. Everything in this thesis, every step, every effort, and every achievement exists only because of Him. Without His strength, His wisdom, and the guidance of the Holy Spirit, this work would not have been possible. He gave me the energy, perseverance, and clarity to move forward even in the most challenging moments.

I am deeply grateful to my Mother, the Virgin Mary, who accompanied me with her love and protection throughout this entire journey.

I also want to express my heartfelt gratitude to my earthly family: my father Borys, my mother Maritza, and my sister Karen. Despite the distance, they were always present—calling me, encouraging me, and reminding me that no matter how far we were physically, our unity as a family remained unbreakable. These three years were not easy, but through God's grace and the Holy Spirit we remained strong and close. Thank you for every sincere word, every emotional support, every visit, and every moment you stayed by my side. During the first year of my doctorate, when we faced one of the most difficult phases of our life—a period of uncertainty and hospitalization of my father—we endured it together with faith. I will never forget everything you have done for me. My gratitude to you is eternal.

My sincere thanks go to my professors at the University of Enna "Kore," which became my home during this journey. I am deeply thankful to Professors Francesco Castelli and Valentina Lentini for their constant support, for caring for me during my most difficult moments, and for always being present when I needed guidance. I also thank the entire team from the University—Prof. Freni, Mirko, Elisa, Maria Stella, Stefania, and Antonio—for their collaboration, kindness, and help throughout my research.

To the University of Catania, I am immensely grateful for granting me the scholarship that allowed me, as an international student from Ecuador, to pursue my studies and build a path in Italy. Thank you for the trust, the opportunity, and the guidance you provided.

I also want to thank my reviewers, Professor Guillermo Ponce and Michele Gatto, for their thoughtful comments, support, and contributions that helped improve the quality of this thesis.

I also want to thank my best and closest friends. A very special appreciation goes to Karem Ramos, who has been like a sister to me. Thank you for being there in my most difficult moments, for your messages, your calls, your constant care, and your love despite the distance and your own challenges. Your presence has been a blessing. My gratitude also goes to PhD José Luis Caisapanta. Your emotional support, your video calls that made me laugh even in the hardest days, and your academic guidance—especially regarding the centrifuge work—were invaluable. Thank you for sharing your experience, your advice, and your friendship.

At the University of Dundee, I extend my sincere thanks to Professor Andrew Brennan, to Craig Davidson Sr., to Craig Davidson Jr. —who was always there with a great attitude, willing to help, collaborate, and share conversations that encouraged me—, and to all the students who helped me—especially Tayyib Jawid. Thank you for your support in the project and for helping me move it forward.

Finally, to all my friends in Italy—Anthony, Debora, Adriano, Ana, Gaetano, Maria, Giorgia, Martina, and Barbara together with her mother—thank you for being my family away from home. Your companionship, your help, your physical presence, and your unconditional support carried me through many moments. You welcomed me into your homes and your lives as if I were a member of your own family. These are things I will never forget.

To each person who contributed directly or indirectly to this journey: thank you, from the bottom of my heart.

Abstract

Rainfall-induced landslides represent a major geotechnical hazard for linear infrastructures in geologically complex regions such as Sicily. This research develops and validates an integrated framework for the evaluation of rainfall-triggered landslide hazards and risk assessment, using the April 2015 failure of the Himera I viaduct (A19 Motorway, Sicily) as a representative case study. Comprehensive site characterization was conducted using geological mapping, in-situ investigations, and laboratory testing of Himera I soils to define stratigraphy, pore-water conditions, and mechanical properties. Rainfall intensity–duration thresholds for potential slope failures were derived and compared to national thresholds for Italy (Brunetti et al., 2010), confirming that Himera I's argillaceous lithologies are susceptible to failure under less severe precipitation conditions than previously recognized.

Physical modelling using centrifuge tests reproduced rainfall infiltration and failure mechanisms under controlled conditions. The methodology drew on advanced practices in centrifuge testing slope analysis (Defae & Knappett, 2014), incorporating instrumented models to record pore pressure, displacements, and failure evolution. Results demonstrated the progressive transition revealed a complex and composite behaviour that combined both rotational and translational components under rainfall, with failure surfaces closely matching back-analyses of the April 2015 event. Finite Element simulations were calibrated against experimental data, enabling improved prediction of displacement fields and factor of safety evolution.

A risk assessment framework was implemented by integrating hazard probability, exposure of critical infrastructure, and vulnerability functions (D. M. Cruden & Fell, 1997). The Himera I application showed that adopting combined rainfall thresholds and displacement-based performance metrics allows for proactive mitigation strategies—such as drainage systems and temporary traffic rerouting—that significantly reduce functional and economic impacts.

This study provides a reproducible methodology for linking geotechnical data, physical modelling, and probabilistic risk analysis. Its findings enhance decision-making for the management of rainfall-induced landslide hazards on strategic transport corridors, with implications for regional planning and climate-change adaptation in Mediterranean environments.

Table of Contents

List of Figures

List of tables

Chapter one
Introduction

1.1. Preface

The failure of a mass of soil located beneath a slope is called a slide. It involves a downward and outward movement of the entire mass of soil that participates in the failure.

Slides may occur in almost every conceivable manner, slowly or suddenly, and with or without any apparent provocation. Usually, slides are due to excavation or to undercutting the foot of an existing slope. However, in some instances, they are caused by a gradual disintegration of the structure of the soil, starting at hair cracks which subdivide the soil into angular fragments. In others, they are caused by an increase of the porewater pressure in a few exceptionally permeable layers, or by a shock that liquefies the soil beneath the slope. Because of the extraordinary variety of factors and processes that may lead to slides, the conditions for the stability of slopes often defy theoretical analysis (Terzaghi et al., 1996).

Different natural phenomena impact the stability of slopes and can cause landslides (Correa-Muñoz & Higidio-Castro, 2017). Landslides are complex natural processes that constitute a serious natural hazard in mountainous countries (Malamud et al., 2004). Landslides can occur in various types environments, both on land and under water, in bedrock or on soils, in cultivated land, in barren slopes and in natural forests, in extremely dry or in very humid areas. And depending on the type of movement they can be classified as falls, topples, slides, spreads or flows. Regarding the material type (rock, debris, soil) involved, landslides can be described as rockfall, debris flow and so on (Varnes, 1978 and 1984).

The consequence of the soil instability due to the seismic activity and the hydrogeological problems are the most common and often called landslides. In regions where, urban residential areas coincide with mountainous terrains, as in the case with majority of towns and cities in Sicily, the risk is higher for people and the economic costs include relocating communities and repairing physical structures. Furthermore, considering the analysed route as a lifeline (vital transportation routes), it is essential understanding which sections could be at risk and compromise the transport circulation during a catastrophic natural event (Leonardi et al., 2020).

A potentially harmful physical event that can cause loss of human life or injured, material damages, environmental degradations, social and economic damages it's called as a natural hazard. Growing population and expansion of settlements in hazardous areas have largely increased the impact of natural disasters both in industrialized and developing countries (Leonardi et al., 2020).

Geotechnical engineering plays a pivotal role in ensuring the stability and safety of civil infrastructure, particularly in regions prone to natural hazards such as landslides and/or earthquakes. The complex interaction between geological, geotechnical, and structural factors demands a multidisciplinary approach to comprehensively assess the risk and behaviour of linear infrastructure situated on slopes.

1.2. Motivation

In Italy, historical settlements (including all types of infrastructures) are often built on hilltops suffering from stability issues, therefore requiring the implementation of monitoring systems, as well as expensive maintenance and restoration works (Ciampalini et al., 2012) (Bianchini et al., 2015). Also, the increasing challenges posed by climate change, which include extreme precipitation events leading to a higher frequency of landslides. Additionally, many existing infrastructures have been designed without adequately considering seismic actions, resulting in potential vulnerabilities. The need to address these geotechnical hazards is pressing, as they can cause sudden and extensive damage, affecting vital transportation and communication corridors (Frodella et al., 2018).

For that reason, by developing a comprehensive risk assessment methodology, it´s aim to contribute to the resilience and safety of the infrastructure networks, mitigating the potential socio-economic impacts of geotechnical hazards. The April 2015 landslide at Himera I on the A19 motorway demonstrated how rapid, rainfall-induced slope failure can compromise vital corridors, disrupt regional economies, and necessitate costly emergency interventions. These vulnerabilities, combined with socio-economic pressures to maintain connectivity and reduce downtime, highlight the urgent need for integrated hazard evaluation and risk management frameworks tailored to rainfall-induced landslides.

Traditional deterministic analyses often fail to capture the probabilistic nature of rainfall thresholds, the temporal variability of exposure, and the complex failure mechanisms observed in recent events. By combining detailed geotechnical characterization, advanced numerical modelling, and centrifuge experimentation, this study aims to bridge the gap between empirical rainfall thresholds and performance-based risk assessment. The proposed methodology seeks to improve predictive capabilities and guide proactive mitigation measures—such as drainage installations, monitoring systems, and emergency response planning—to enhance the resilience and safety of critical linear infrastructures like Himera I.

1.3. Aims

1.3.1. General Objective

Develop and validate an integrated methodology for evaluating rainfall-induced landslide hazards and conducting risk assessment for linear infrastructures. The methodology combines site-specific geotechnical characterization, advanced numerical modelling, and centrifuge experimentation, using the Himera I viaduct (A19 Motorway, Sicily) as a representative case study. The overarching objective is to improve predictive capabilities and provide insights for risk assessment and the formulation of mitigation strategies applicable to similar geotechnical contexts.

1.3.2. Specific Objective

- Establish a reliable subsoil model through a comprehensive understanding of geological, geotechnical, geophysical and morphological data with the Himera I case example.
- Implement advanced numerical modelling using finite element analysis to simulate the rainfall infiltration and the effect of the soil the progressive failure mechanisms of the slope (landslides).
- Conduct centrifuge tests replicating rainfall infiltration and slope failure to analyse displacement patterns and failure evolution to validate numerical simulations with the physical behaviour observed at Himera I.
- Integrated and provide insights to validated methodologies and strengthen the framework for landslide risk assessment and management, thus minimizing potential risks and inconvenience to the population.

Chapter two
Literature Review

2.1. Landslide mechanisms

The landslide problem is dominated by uncertainty, whether it be a natural slope or an excavation. Uncertainty arises at all stages in the resolution of a problem, from site characterization to material property evaluation to analysis and design, through to consequence assessment. Success in practice overcomes some of these limitations by the application of the observational method, a form of consequential risk analysis.

Nevertheless, this success is far from perfect. Many failures are encountered that might be avoided by a more focused approach to uncertainty and new questions are being put to the Geotechnical Engineer that cannot be answered in terms of Factors of Safety alone. At the same time, the landslide problem entails considerable diversity and it is prudent to promote new approaches cautiously least one discredit the whole enterprise.

Landslides also involve a wide variety of materials. Restricting considerations to soils alone, Morgenstern (1992) presented a classification of soils that highlighted the different degrees of confidence associated with establishing the operational strength of a soil for purposes of evaluating slope stability. The classification is reproduced as Figure 1. If a text-book soil is regarded as one where the process of undisturbed sampling and laboratory testing leads directly to parameters that control design, there are very few text-book soils.

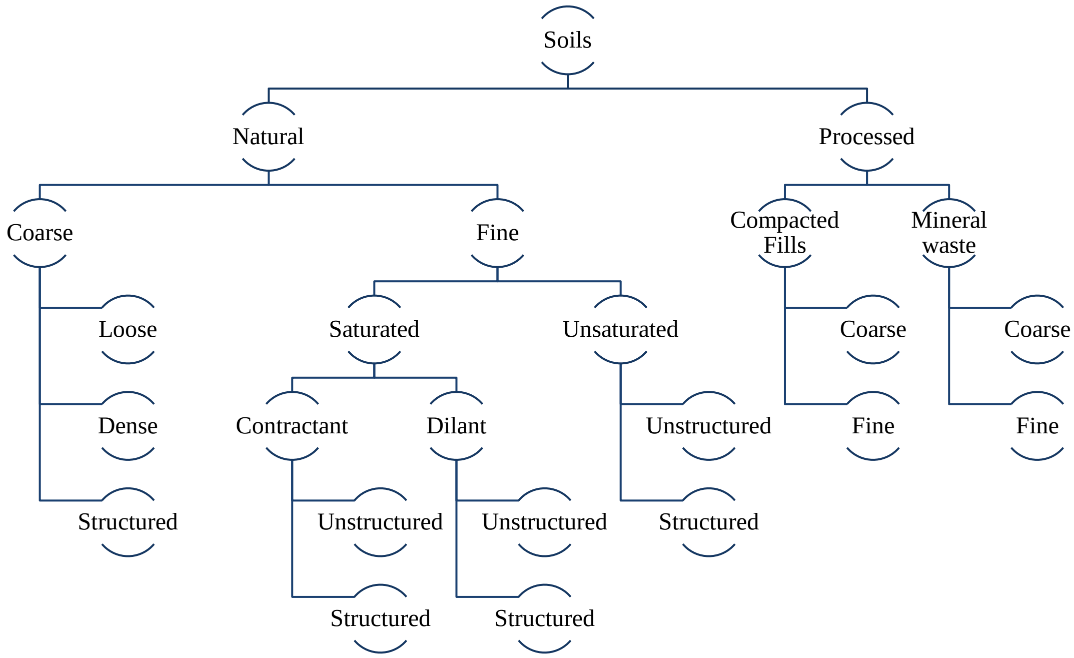

***Figure 1**. A Problem oriented classification of Soils (Morgenstern, 1992).*

The role of the Factor of Safety in slope design is complex. One well-recognized role is to account for uncertainty and to act as a factor of ignorance with regard to reliability of the inputs to the analysis. However, an additional major role of the Factor of Safety is that it constitutes the empirical tool whereby deformations are limited to tolerable amounts within economic restraints. The choice of the appropriate Factor of Safety is greatly influenced by the accumulated experience with a particular soil or rock mass and the experienced designer recognizes this diversity. Morgenstern (1991) has provided examples to stress that traditional stability analyses with sometimes traditional values of Factor of Safety are not always capable of inhibiting undesirable behaviour.

It is timely to evaluate the potential of risk assessment procedures applied to landslides. The intent of this presentation is to explore how progress might be made at the interface between theory and practice in order to encourage change among practitioners (D. M. Cruden & Fell, 1997).

The probability of landsliding can be expressed in terms of:

- the number of landslides of a certain characteristic that may occur in a study area per year.

- the probability of a particular slope experiencing landsliding in a given period, e.g. a year.
- the driving forces exceeding the resistant forces in probability or reliability terms, without relating this to an annual frequency.

There are several ways of calculating probability (D. M. Cruden & Fell, 1997):

- Historic data within the area of study, or areas with similar characteristics, e.g. geology, geomorphology.
- Empirical methods based on correlations in accordance with slope instability ranking systems.
- Use of geomorphological evidence (coupled with historic data, or based on judgement).
- Relationship to the frequency v intensity of the triggering event, e.g. rainfall, earthquake.
- Direct assessment based on expert judgement, which may be undertaken with reference to a conceptual model, e.g. use of a fault tree methodology.
- Modelling the primary variable, e.g. piezometric pressures versus the triggering event, coupled with varying levels of knowledge of geometry and shear strength.
- Application of formal probabilistic methods, taking into account the uncertainty in slope geometry, shear strength, sliding mechanism, and piezometric pressures. may be done either in a reliability framework or taking into account the frequency (usually by considering pore pressures on a frequency basis).
- Combinations of the above methods.

These involve an increasing degree of analysis, and rigor, but not necessarily an increasing accuracy in the assessment of probability.
It is important to link the subjective information with the measured data. This can be done formally or informally. To do this is important since one

can supplement a limited set of data with experience, and vice versa, make more general experience, more specific (D. M. Cruden & Fell, 1997).

There has been extensive research into formal probabilistic analysis of slopes. The state of the art for these calculation methods is well established, and the methods can be applied with confidence. The application of such methods should include consideration of the following aspects to give realistic outcomes (D. M. Cruden & Fell, 1997):

- surface and subsurface geometry
- hydrogeology
- variation of pore water pressures with time
- material strengths
- discontinuities in rocks, including persistence
- spatial variation of parameters.

In addition, the problem must be viewed as a system of potential failure surfaces rather than just a single, sometimes critical, failure surface. Various "levels" of data on uncertainty should be used, these range from pure judgmental to statistically robust parameter estimation.

It should be noted that often the greatest area of uncertainty is the prediction of pore pressures in a slope, and no degree of sophistication on the uncertainty in shear strength and geometry can give realistic answers unless a defensible, properly modelled, assessment is made of pore pressures. In other cases, properties, such as defect persistence are most critical, and most be modelled correctly.

This is difficult to achieve, and leads back to the more subjective methods, or a combination of subjective and analytical methods.

2.1.1. Types of landslides and triggering factors

Landslides are defined as the downward and outward movement of slope-forming materials, including rock, soil, artificial fill, or a combination of these. According to the classic classification proposed by Varnes (1978), landslides can be categorized into five main types based on the type of movement and material involved: falls, topples, slides (rotational and translational), spreads, and flows. Each of these types exhibits different kinematic behaviours and poses varying degrees of risk to built infrastructure.

Rotational slides typically occur in homogeneous clayey slopes and are characterized by a concave slip surface. Translational slides involve more planar surfaces and are often associated with layered soils. Flows, including debris flows and earth flows, involve fluidized materials and are particularly destructive due to their high velocity and mobility.

Landslides are triggered by various natural and anthropogenic factors. The most common natural triggers include:

- Heavy or prolonged rainfall, which increases pore water pressure and reduces soil shear strength (Iverson, 2000);
- Earthquakes, which induce cyclic loading and can lead to liquefaction or loss of soil strength (Seed & Idriss, 1982);
- Weathering processes, which degrade rock masses and reduce slope stability;
- Rapid snowmelt or changes in groundwater levels.

Human-induced triggers include excavation at the toe of slopes, deforestation, poor drainage design, and loading on the slope crest. In the Mediterranean region, shallow landslides are often associated with intense and short-duration rainfall events, particularly in clay-rich soils (Cascini et al., 2008).

2.1.2. Slope movement types and processes

Since all movement between bodies is only relative, a description of slope movements must necessarily give some attention to identifying the bodies that are in relative motion. For example, the world slide specifies relative motion between stable ground and moving ground in which the vectors of relative motion are parallel to the surface of separation or rupture; furthermore, the bodies remain in contact. The world flow, however, refers not to the motions of the moving mass relative to stable ground, but rather to the distribution and continuity of relative movements of particles within the moving mass itself (Varnes, 1978a).The state of the art for analysis of the mechanics of travel distance and velocity varies considerably, depending on the classification of the landslide.

In a general sense, the following applies (Schuster & Krizek, 1978):

- Falls - Relatively sophisticated methods are available, with the initial phases of movement better modelled than later stages.
- Topples — Models are poor after movement begins.
- Flows — Models of the mechanics exist, but there are limitations due to the difficulty of estimating input parameters, the properties varying in different parts of the flow, e.g. a debris flow may have a front part consisting of boulders and trees, a main mass of silt/sand/gravel; and a finer, higher water content layer at the base. The properties, and the volume of the material often alter during the event.
    - Flows in bedrock
    - Flows in debris and earth
- Slides and Spreads — Models are poor after movement begins. For these, it is important to be able to estimate travel distance, velocity and differential movements, because these influence damage considerably.
    - Rotational slides
    - Translational slides
    - Lateral spreads
- Complex —More often than not, slope movements involve a combination of one or more of the principal types of movement described above, either within various parts of the moving mass or at different stages in development of the movement.

Some of the various combinations of movements and materials are shown in the Table 1.

Table 1. *Abbreviated classification of slope movements. Materials are divided into two classes: rock and engineering soil; soil is further divided into debris and earth (Schuster & Krizek, 1978).*

<table>
<tr><td colspan="3" rowspan="3">TYPE OF MOVEMENT</td><td colspan="3">TYPE OF MATERIAL</td></tr>
<tr><td rowspan="2">BEDROCK</td><td colspan="2">ENGINEERING SOILS</td></tr>
<tr><td>Predominantly coarse</td><td>Predominantly fine</td></tr>
<tr><td colspan="3">FALLS</td><td>Rock fall</td><td>Debris fall</td><td>Earth fall</td></tr>
<tr><td colspan="3">TOPPLES</td><td>Rock topple</td><td>Debris topple</td><td>Earth topple</td></tr>
<tr><td rowspan="3">SLIDES</td><td>ROTATIONAL</td><td rowspan="2">FEW UNITS</td><td>Rock slump</td><td>Debris slump</td><td>Earth slump</td></tr>
<tr><td rowspan="2">TRANSLATIONAL</td><td>Rock block slide</td><td>Debris block slide</td><td>Earth block slide</td></tr>
<tr><td>MANY UNITS</td><td>Rock slide</td><td>Debris slide</td><td>Earth slide</td></tr>
<tr><td colspan="3">LATERAL SPREADS</td><td>Rock spread</td><td>Debris spread</td><td>Earth spread</td></tr>
<tr><td colspan="3" rowspan="2">FLOWS</td><td rowspan="2">Rock flow (deep creep)</td><td>Debris flow</td><td>Earth flow</td></tr>
<tr><td colspan="2">(soil creep)</td></tr>
<tr><td colspan="2">COMPLEX</td><td colspan="4">Combination of two or more principal types of movement</td></tr>
</table>

2.1.3. Vulnerability of linear infrastructure

Linear infrastructures are inherently exposed to spatially distributed hazards due to their extensive footprint. Unlike point-based infrastructures, linear systems interact with a wide range of geological, geotechnical, and hydrological conditions. Their vulnerability stems not only from the frequency and intensity of hazardous events but also from their strategic importance in maintaining connectivity and mobility.

Several studies have examined the vulnerability of transportation corridors to landslides. For example, Hungr et al. (2005) highlighted the importance of incorporating landslide susceptibility into the planning and maintenance of transportation networks. Petschko et al. (2013) emphasized the need to identify high-risk segments through landslide inventories and susceptibility mapping. In Italy, Castelli et al. (2016) analyzed landslide-prone zones in Sicily, recommending geotechnical instrumentation and numerical simulation as tools for long-term infrastructure management.

Moreover, vulnerability assessment is increasingly being integrated into multi-risk frameworks, combining landslide hazard with seismic risk and flood exposure. This approach is particularly relevant for bridges and viaducts located on or near unstable slopes, where the failure of a single element can cause cascading effects across the network (Lentini et al., 2018).

2.2. Slope stability analysis

Static slope stability analysis provides the fundamental framework for assessing landslide hazard. It is rooted in the balance between resisting and driving forces along a potential slip surface. Classical slope stability analysis treats failure as the loss of equilibrium of a potential sliding mass when the available shear strength along a kinematically admissible surface becomes insufficient to resist driving stresses.

In static conditions, the Factor of Safety, FS, is defined as the ratio between available shear strength and mobilized shear stress along the candidate slip surface. Limit-equilibrium methods (LEMs) remain the most widely used tools because they offer transparent mechanics, modest data requirements, and compatibility with codes and practice (e.g., Fellenius/Swedish circle, Bishop simplified, Janbu, Morgenstern–Price, Spencer). Textbooks and design monographs provide robust implementations and guidance on method selection and reliability (Abramson et al., 2002) (Duncan & Wright, 2005) (Krahn, 2004) (R. F. Craig, 2012).

For purely granular soils, infinite slope models under dry conditions show that stability depends essentially on slope angle and friction angle, that means an infinite slope with an inclination ($\beta°$) is assumed, and it is necessary to evaluate the stability and recognize its potential failure surface, in which the forces involved are represented in Figure 2.

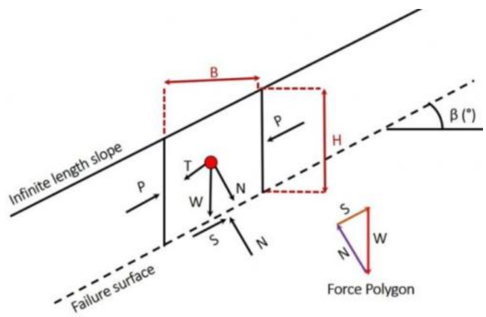

Figure 2. *Slope stability analysis of granular soil in dry conditions (GeoEngineers)*

The weight of the soil block is calculated as:

$$W = \gamma_{dry} \cdot B \cdot z \cdot \left(\frac{kN}{m}\right) \tag{2.1}$$

which the $\gamma_{dry}$is the total unit weight of the soil, B is the length along the slip plane between the two ends of the block and z is the vertical depth of the shear plane.

And given the inclination of the slope, the weight is analyzed into two components, where the N is the vertical reaction anting on the section:

$$N = W\cos(\beta) \tag{2.2}$$

$$T = W\sin(\beta) \tag{2.3}$$

The maximum shear stress that can be developed along the failure plane is the following:

$$S = N\tan\varphi \tag{2.4}$$

where the φ is the friction angle of the soil. By combining the equations 2.5, the factor of safety can be written in terms of effective stresses as:

$$FS = \frac{S}{T} = \frac{N\tan\varphi}{W\sin(\beta)} = \frac{W\cos(\beta)\tan\varphi}{W\sin(\beta)} = \frac{\tan\varphi}{\tan\beta} \tag{2.5}$$

This exact relation is used by Al-Defae (2014) to check static stability of cohesionless slopes prior to subsequent analyses, explicitly reporting for the dry case in terms of drained conditions ($c^{'} = 0, u = 0$).

However, many natural and engineered slopes include cohesive materials, such as clays, silty clays, and residual soils, where shear strength incorporates not only frictional resistance but also effective cohesion. In these cases, the Mohr-Coulomb criterion govern shear strength:

$$\tau_f = c' + \sigma'\tan\varphi' \tag{2.6}$$

where c' is effective cohesion, σ' the effective normal stress, and φ' the effective friction angle. The corresponding Factor of Safety (FS) for an infinite slope at depth z is:

$$FS = \frac{c' + (\gamma z cos^2\beta - u)\tan\varphi'}{\gamma z \sin\beta\cos\beta} \tag{2.7}$$

In saturated slopes, rainfall infiltration raises u, reducing σ' and therefore decreasing FS. Take et al. (2004) demonstrated through centrifuge modelling of fill slopes that rainfall infiltration progressively destroys suction in loose silty sands and decomposed granites, causing wetting collapse and reducing shear resistance even without complete liquefaction.

Cohesive soils may retain stability longer than granular soils, but once pore pressures rise or cracks propagate, failures can occur suddenly and extensively. Rainfall infiltration modifies the hydro-mechanical response of cohesive soils through coupled processes of pore pressure increase, suction reduction, and softening of weak layers. Unlike cohesionless soils, clays and silty clays display apparent cohesion from suction and interparticle bonding; when wetting progresses, both effective cohesion and friction angle can degrade. This reduction in strength is a central mechanism driving rainfall-induced landslides.

Field and laboratory studies show that matric suction provides additional shear strength to partially saturated cohesive soils. As rainfall infiltrates, suction decreases sharply, eroding the apparent cohesion component. Wang et al. (2010) observed that in homogeneous clay slopes, rainfall induced a delayed suction drop, whereas in weak-layered slopes the reduction was faster and deeper, leading to earlier initiation of instability.

This finding highlights that rainfall can penetrate preferentially along fissures or weaker strata, accelerating the loss of strength. The soil–water characteristic curve (SWCC) of the clay tested demonstrated that even a small increase in water content (1%) could correspond to a suction decrease of more than 7 kPa, underscoring the sensitivity of cohesive soils to wetting. Another important thing is the presence of weak layer, that greatly modifies infiltration patterns. The weak layers, due to their higher permeability and compressibility, allowed rainfall to infiltrate more rapidly and deeper into the slope body (Figure 3), creating localized zones of saturation and loss of shear strength. Thus, rainfall not only decreases the intrinsic shear resistance of clays but also promotes structural weaknesses that localize deformation (R. Wang et al., 2010).

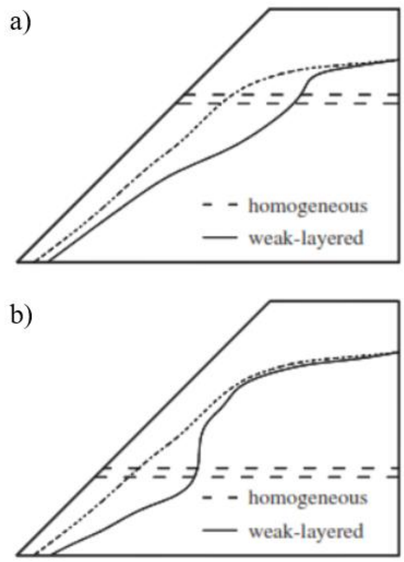

Figure 3. *Comparison between the position of the weak layer in the slope: a) upper weak-layer slope vs. homogeneous slope; b) lower weak-layered slope vs. homogeneous slope. (Wang et al., 2010).*

The progressive failure process in cohesive soils under rainfall is closely linked to the formation of shear zones. In the centrifuge models, shear zones widened initially as pore pressures rose, but later localized, coinciding with slope failure. In slopes with weak layers, these shear zones became discontinuous at the layer interfaces, reflecting the reduction in cohesion and stiffness of the saturated weak layer seams. Ultimately, rainfall-induced weakening concentrated strain into narrow shear bands that transformed into slip surfaces.

Hudacsek et al. (2015) confirmed similar behaviour for clay embankments, showing that climatic effects (wetting and drying cycles) significantly affect pore pressure profiles and stability, with rainfall leading to softening and reduced factors of safety. In clayey slopes, the interplay between cohesion, permeability, and long-term suction recovery is critical for assessing hazard.

2.2.1. Geotechnical parameters influencing slope stability

The stability of natural and engineered slopes is fundamentally controlled by the geotechnical parameters that govern soil strength, hydraulic behaviour, and deformation characteristics. In static conditions, slope failure occurs when the mobilized shear stress along a potential slip surface exceeds the available shear strength of the soil, as described by the Mohr–Coulomb criterion. However, the soil's capacity to resist failure is not determined by a single property, but rather by the combined effect of multiple parameters, which are in turn influenced by environmental conditions such as rainfall infiltration.
Key parameters that include:

1. *Shear strength parameters*

- Cohesion (c'), which provides an intercept in the shear strength envelope, crucial for stability of clay-rich slopes and engineered embankments. Laboratory and field studies show that even modest cohesion values can significantly increase FS under unsaturated conditions. However, rainfall infiltration reduces apparent cohesion associated with matric suction, leaving only the effective cohesion component (Fredlund & Rahardjo, 1993; Rahardjo et al., 2005);
- Friction angle (φ'), is dominant in sandy soils, in cohesive soils its role is still essential. Residual clays exhibit reduced friction after prolonged shearing, leading to progressive failures. Rahardjo et al. (2005) demonstrated that incorporating effective stress analysis with suction-controlled shear strength provides more accurate predictions of slope failure under rainfall;
- Unit weight (γ), which directly affects the driving forces; cohesive soils exhibit lower permeability, so pore pressure dissipation is slow. This can create delayed instabilities after rainfall, with FS decreasing progressively over days or week;

2. *Hydraulic conductivity and pore-pressure response*

Pore-water pressures (u) and matric suction, which govern the effective stress state, especially in unsaturated or partially saturated soils. The hydraulic conductivity and anisotropy of the soil dictate infiltration rates and the build-up of pore pressures during rainfall, while stratigraphy and discontinuities create preferential slip surfaces that localize deformation. Suction contributes to "apparent cohesion" in unsaturated cohesive soils. When rainfall infiltrates, suction decreases rapidly, triggering slope weakening. Rahardjo et al. (2005) modelled this effect and demonstrated that shallow failures often initiate once suction falls below a critical threshold;

3. *Structure and plasticity*

Plasticity, and structure influence both hydrological response and long-term strength degradation under wetting or cyclic loading, cohesive soils often contain fissures, desiccation cracks, or heterogeneities that act as preferential pathways for infiltration. Low permeability layers and perched water tables create rapid pore-pressure rises during storms, while fissures act as preferential flow paths. Take et al. (2004) emphasized how layering and seepage concentration create transient pore pressures, triggering slips even before full saturation

4. *Vegetation and surface cover*

Vegetation reduces erosion and provides root reinforcement but can also increase infiltration locally, altering subsurface hydrology.

Understanding how these parameters interact is essential for reliable slope stability analysis. For example, rainfall infiltration reduces matric suction and increases pore-water pressures, simultaneously lowering apparent cohesion and effective stress, thereby decreasing the factor of safety. Cohesive soils may retain strength longer due to cohesion, but once saturation occurs, strength loss can be abrupt. By contrast, granular soils respond rapidly to pore-pressure changes but exhibit more predictable frictional resistance.

Therefore, a detailed review of geotechnical parameters is indispensable, as it provides the foundation for both analytical models and risk assessment frameworks. The following subsections discuss these parameters systematically, highlighting their role in slope stability under static conditions, with emphasis on rainfall-induced changes.

2.3. Rainfall-induces slope failures

Rainfall-induced landslides represent one of the most recurrent and destructive natural hazards affecting mountainous and hilly regions worldwide. Infiltration processes associated with rainfall events modify the hydro-mechanical state of the soil by increasing pore water pressure and decreasing matric suction in unsaturated layers (Iverson, 2000). This reduction in effective stress leads to a progressive loss of shear strength, particularly in fine-grained and weathered soils. With sustained or intense rainfall, pore pressure build-up may initiate local failure, which can propagate downslope, leading to large-scale instability. Such progressive failure mechanisms are especially relevant in slopes with pre-existing discontinuities or unfavourable stratigraphic configurations.

The evaluation of rainfall-induced landslide hazards requires a comprehensive understanding of infiltration dynamics, soil mechanical response, and the critical rainfall conditions that initiate instability. The scientific community has addressed these issues through both process-based physical models (Montgomery & Dietrich, 1994)(Crosta & Frattini, 2003) and empirical rainfall thresholds (Caine, 1980)(Guzzetti et al., 2008). While physically based models quantify the response of pore water pressure to rainfall infiltration and its effect on slope stability, empirical thresholds derive statistical relationships between rainfall intensity, duration, and landslide occurrence.

2.3.1. Rainfall as the dominant trigger of landslides

Rainfall is widely recognized as one of the most pervasive and destructive triggers of landslides worldwide. Intense or prolonged precipitation alters the hydrological balance of slopes by increasing pore water pressures, reducing effective stress, and initiating progressive failure mechanisms in soil and rock masses. Internationally, several catastrophic events illustrate the role of rainfall as the primary destabilizing factor. For instance, in Taiwan, Typhoon Morakot (2009) generated cumulative rainfall exceeding 2,800 mm in three days, which induced large-scale landslides and devastating mudflows in Taitung County, including the Daniau Creek watershed where over 300,000 m^3 of sediment was mobilized, burying houses and destroying infrastructure (J.-B. Peng & Lu, 2013). Similarly, in the United States, debris flows in Yosemite Valley (California) have been repeatedly triggered by rainfall events, with numerical back-analyses showing that infiltration-driven pore pressure increases, and channelized runoff facilitated debris-flow initiation and long runouts (Bertolo & Wieczorek, 2005). A comparable situation has also been documented in Ecuador, where in the province of Cañar, persistent rainfall combined with inadequate surface drainage contributed to the progressive saturation of slopes near the PC2 sector, leading to erosion, shallow sliding, and local roadway instability, as reported in the corresponding geotechnical assessment (Pinargote, 2022). These international examples highlight the commonality of rainfall thresholds as critical precursors for slope instability, irrespective of geological setting.

In Italy, these phenomena are particularly pervasive due to the country’s complex geological, geomorphological, and climatic conditions. National inventories report more than 500,000 landslides across the Italian territory, with an average density of approximately 1.6 failures per square kilometre (Trigila, 2007). Historical records confirm that rainfall-induced slope instabilities are responsible for significant societal impacts, including more than 6,000 fatalities, missing persons, or injuries between 1950 and 2009 (Guzzetti, 2000)(Guzzetti et al., 2005). High-intensity storms have likewise produced destructive debris flows, such as the Fella River event of 2003 in northeaster Italy (in the European Alps), where more than 1,000 shallow failures and debris flows were mobilized during a single storm delivering nearly 400 mm of rainfall in less than 12 hours (Boniello et al., 2010).

A particularly illustrative case in central Italy is the Sarno debris flow disaster of May 1998, where 160 landslides were triggered by cumulative rainfall of 200–300 mm in less than 48 hours, claiming more than 150 lives (Aleotti & Polloni, 2003)(T. Peng & Lu, 2013). The Sarno event epitomizes how infiltration processes, coupled with colluvial soil mantles and steep slopes, can rapidly evolve into catastrophic flows once rainfall thresholds are exceeded. Comparable conditions have been documented in the Abruzzo region, where regional thresholds defined by Brunetti et al. (2010) were systematically lower than national averages, underscoring the importance of local lithological and hydrological conditions in modulating slope response to rainfall.

The country’s complex topography and diverse lithologies make it particularly susceptible to rainfall-induced slope failures. National databases and empirical analyses have led to the definition of rainfall intensity–duration (ID) thresholds, establishing probabilistic limits beyond which landslide initiation is highly likely (Caine, 1980)(Guzzetti et al., 2008)(Brunetti et al., 2010).

In their seminal work, Brunetti et al. (2010) analyzed more than 750 rainfall-induced landslides across the Italian territory, demonstrating that landslides may be triggered even under relatively modest rainfall conditions, with mean intensities of only 1–2 mm/h sustained over 12–24 hours. These findings underline that both short intense storms and long-duration moderate rainfall events are capable of destabilizing susceptible slopes. The nationwide statistics compiled by Brunetti et al. (2010) confirm that about 70% of documented rainfall-induced landslides occurred in northern Italy, 20% in central regions, and only 10% in the south (Figure 4a). This spatial imbalance partly reflects data availability rather than a true absence of failures in Sicily.

In fact, recent studies demonstrate that Sicily is highly susceptible to rainfall-induced instabilities. A more localized perspective is provided by recent studies in central Sicily, which demonstrate that the region is highly susceptible to rainfall-triggered slope failures. In particular, a detailed landslide inventory prepared for the Enna province highlights the essential role of systematic mapping in hazard assessment. The inventory incorporates information on landslide type, volume, travel distance, state of activity, and date of occurrence, thereby enabling the identification of existing failures and their controlling factors (Figure 4b). On this basis, a series of rainfall-induced events was reconstructed and classified with respect to their timing and triggering conditions, providing valuable insights into the relationship between rainfall patterns and slope response (Castelli et al., 2016).

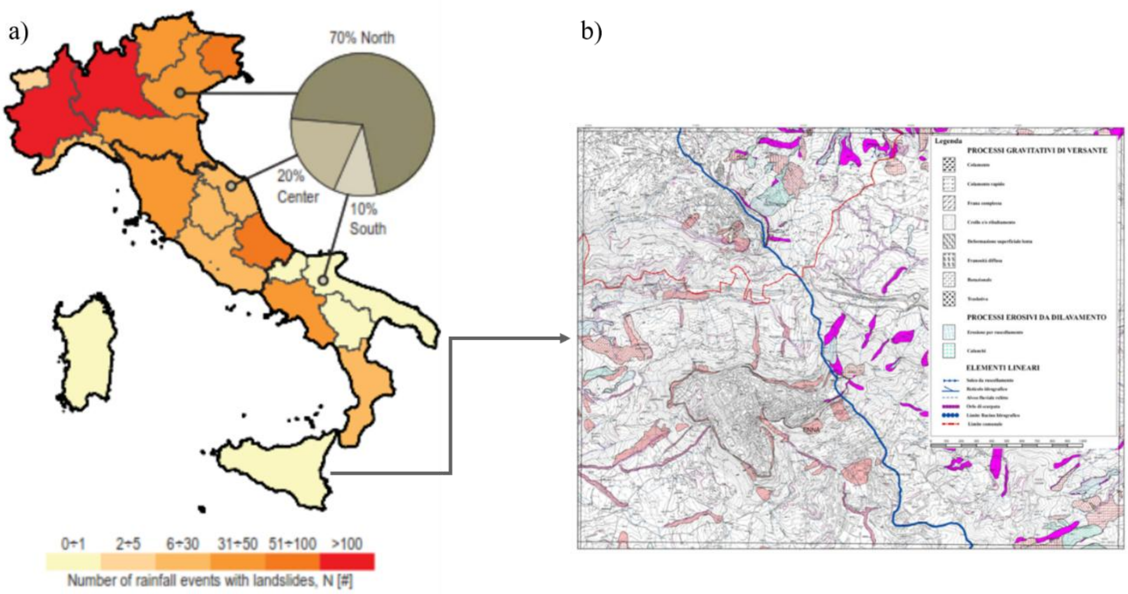

Figure 4. a) Landslide and rainfall information in Italy (Brunetti et al., 2010), b) landslide inventory applicate to Enna area in Sicily (Castelli et. al., 2016).

For example, the landslide of 2 February 2014 in Enna was initiated after cumulative rainfall of 116.6 mm over 30 days, exceeding a critical threshold of 109.9 mm (Castelli et al., 2016). This relatively moderate precipitation input was enough to destabilize slopes in the Enna area, disrupting transport infrastructure and confirming the vulnerability of Sicilian terrain to both short and intense storms as well as prolonged moderate rainfall.

Similarly, in eastern Sicily, the Messina event of 1 October 2009 caused by ~230 mm of rain in less than nine hours triggered more than 500 shallow landslides and debris flows within an area of 60 km², leading to 37 fatalities and widespread structural damage (Maugeri & Motta, 2011). Together, these Sicilian case studies confirm that both short, high-intensity rainfall and prolonged moderate precipitation represent critical triggers of slope instability. They also underscore the importance of developing localized rainfall thresholds and hazard assessment frameworks, complementing the national-scale thresholds derived by Brunetti et al. (2010).

2.3.2. Hydro-mechanical response

The mechanisms by which rainfall destabilizes slopes are well established in geotechnical and hydrological literature. Rainfall infiltration alters soil water content, increasing pore pressure in saturated zones and reducing matric suction in unsaturated zones (Fredlund & Rahardjo, 1993)(Iverson, 2000). The progressive reduction of effective stress decreases shear strength along potential slip surfaces, particularly where permeability contrasts or fissures enhance preferential flow. Unsaturated soil mechanics frameworks emphasize the role of suction in providing apparent cohesion, which can be rapidly lost during prolonged wetting events. Field and laboratory studies confirm that fine-grained colluvium and pyroclastic soils are especially susceptible to rapid reductions in shear resistance under rainfall infiltration (Crosta & Frattini, 2003).

A seminal contribution to rainfall threshold analysis was provided by Caine (1980), who proposed a global intensity–duration (ID) threshold curve for shallow landslides:

$$I = \alpha D^{-\beta} \tag{2.8}$$

where I is rainfall intensity (mm/h), D is rainfall duration (h), and α, β are empirical parameters. Subsequent studies adapted this framework to national, regional, and local contexts. Process-based models complement empirical thresholds by simulating infiltration and slope stability evolution. Iverson (2000) proposed a one-dimensional model linking infiltration rates, pressure head propagation, and slope stability.

Similarly, Crosta & Frattini (2003) introduced distributed hydrological–geotechnical models for shallow landslide susceptibility mapping. These models consistently show that rainfall duration is as critical as intensity, with antecedent soil moisture playing a decisive role in determining threshold exceedance.

The integration of empirical rainfall thresholds with process-based models forms the basis of advanced risk assessment frameworks. Probabilistic approaches, as demonstrated by Brunetti et al. (2010), allow the definition of multiple thresholds associated with different exceedance probabilities, which can be incorporated into early warning systems. Such schemes have direct relevance for civil protection, as they improve predictive capabilities and enable timely interventions to safeguard infrastructure and populations.

2.4. Landslide risk management

2.4.1. Introduction

Many systematic or formal approaches to landslide risk assessment and management exist. They range from mapping procedures to procedures employing decision analysis. A landslide risk mapping was reviewed and a corresponding decision analysis procedure was proposed in a paper presented at the Fifth International Symposium on Landslides in Lausanne (Einstein, 1988). Since this or similar formal procedures have been adopted or recommended in a number of regions (US, Himalaya-Hindukush, France, Switzerland, Scandinavia), the most important aspects will be summarized below.

Landslide risk assessment and management procedures start with assessing the state of nature and end with actions which include a variety of active or passive countermeasures to cope with landslides (Roberds et al., 1997).

2.4.2. Definitions

Landslides, like other events such as floods, earthquakes and avalanches, are natural phenomena which are often difficult to predict, because they are uncertain, and which have potentially detrimental consequences. "Phenomena", "uncertainty" and "potential consequences" need to be captured by mapping and other systematic description procedures. The sequence in which the terms have been mentioned is also the sequence followed by most assessment procedures Figure 5. The phenomenon has to be described, then it is necessary to deal with its unpredictability and finally, it has to be related to the consequences. The expressions "danger", "hazard" and "risk" will be used to characterize phenomena, uncertainty and consequences:

Danger: The natural phenomenon, in this case the landslide, is geometrically and mechanically characterized. This essentially corresponds to descriptions or classifications such as those by (Varnes, 1978)(UNESCO Working Party on World Landslide Inventory (WP/WLI), 1993). Cruden & Varnes (1996) but includes an association with a particular location. The danger can be an existing one such as a creeping slope or it can be a potential one such as a rock fall. The characterization of the danger does, however, and this is very important, not include any forecasting.

Hazard: The limited predictability of the danger, in other words, its uncertainty can be dealt with by formally assessing probabilities to a particular phenomenon. Thus:

Hazard = probability that a particular danger occurs within a given period of time.

The definition in Varnes (1984) is somewhat different in that it states "natural hazard means the probability of occurrence within a specified period of time and within a given area of a potentially damaging phenomenon". The difference is in the geometric definition which Varnes (1984) specifically includes in the hazard definition while here it is specifically included in the danger definition.

The latter is preferable since it makes a rigorous description of geometry and mechanisms as used in the World Landslide Inventory (UNESCO Working Party on World Landslide Inventory (WP/WLI), 1993) possible, and since it can be logically transferred into analytical expressions. Landslide susceptibility as used in many mapping procedures (e.g. Brabb et al., 1972) corresponds to hazard by equating spatial probabilities to temporal probabilities.

<u>Risk:</u> Since the same hazard can lead to entirely different consequences depending on the use of the affected terrain risk is introduced here as:

Risk = hazard x potential worth of loss.

Loss can involve loss of life and injuries, capital loss or non-monetary environmental effects. It is, however, necessary to make a few more comments regarding the terms risk and hazard: The definition of the term "risk" varies amongst disciplines. The above used definition "hazard x worth of loss" or otherwise expressed, "probability of an event x the consequences if the event occurs" is that of statistical decision theory. In the insurance business, risk is often only the monetary component, i.e. only the consequences (see e.g. Vanmarcke & Bohnenblust, 1982; Baecher & Christian, 2005). Another definition of risk is "the uncertainty about the occurrence of an event" (see Ioannou, 1984). Also, it often may be informative to use the terms "damage" or "consequences" instead of "worth of loss".

Vulnerability: This is a term which has been introduced by Varnes (1984) to represent the fact that an endangered "element" (e.g. a house) may suffer different degrees of loss from a particular danger. Vulnerability which is expressed on a scale between 0 and 1 is thus the uncertainty of suffering a particular loss. As will be shown later, vulnerability can be formulated as a conditional probability (Roberds et al., 1997).

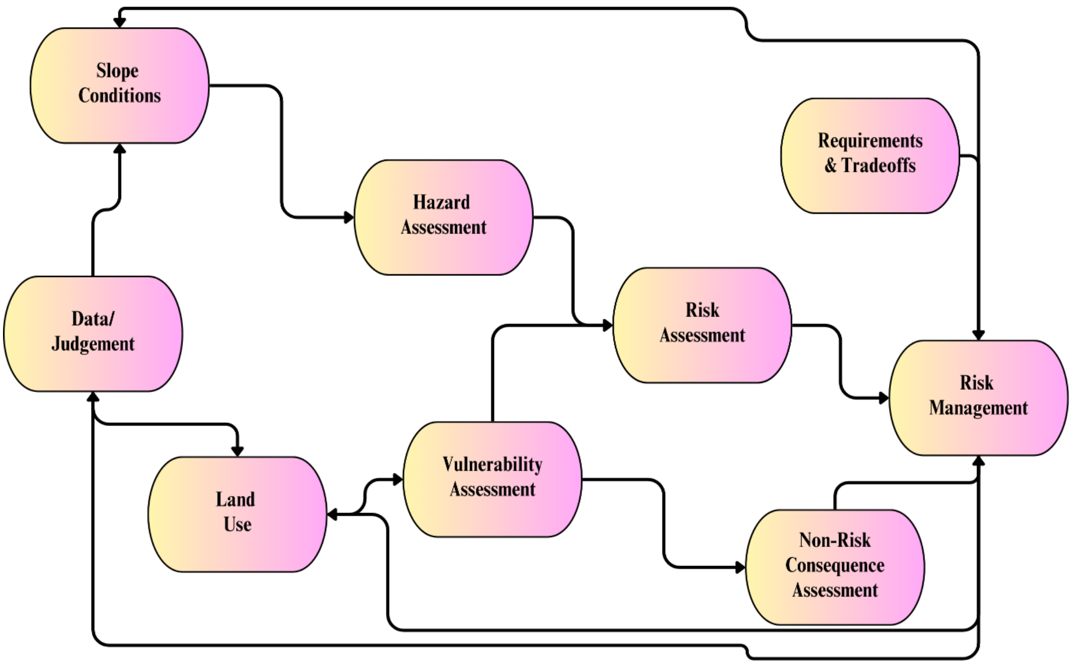

Figure 5. *Integrated Risk Assessment and Risk Management approach (Roberds et al., 1997).*

2.4.3. Mapping procedure

According to Einstein (1997) this procedure, which is based on a sequence of mapping steps or-levels leading all the way to specifying countermeasures, is well established (Varnes, 1984)(Brabb, 1984)(Anbalagan & Singh, 1996)(Alger & Brabb, 1985). The individual levels are the following:

– Level 1 - State of Nature Maps

Basic information describing the state of nature is collected in the field and from the literature. This information includes topographic maps, geological (surface, bedrock, structural) maps; vegetation maps, hydrologic (rainfall, drainage, groundwater) maps; geotechnical maps, profiles, test results; displacement measurements; water level observations; visual observations.

The basic information is largely "analytical" (Varnes, 1984) and does, therefore, usually not include any synthesis or interpretation. In some instances it does, however, include some interpretative aspects such as interpolation between outcrops or boreholes; in such cases the maps should state this fact. Also, surface geologic maps and geotechnical maps often include indications on existing landslides. This basic information is very often condensed in a single map. So, called engineering geologic maps (see e.g. Lozińska-Stępień, 1979) are examples of such condensed maps in which significant information (not necessarily landslide oriented) is represented while other information is left out. Today's digitizing and data base management procedures offer a wide range of possibilities of collecting and representing the basic information.

- Level 2 - Danger Maps

In these maps which are often called "inventories", existing and potential slope instabilities are identified. They represent a particular form of terrain analysis maps. Danger maps are usually developed from Level 1 maps and make use of additional information on slope instabilities. If possible, detailed geometric and mechanical descriptions are given which include the type of slope instability, for instance, using the classification schemes by Varnes (1978), UNESCO (1993), D. Cruden (1996). It is important to record, if applicable, that different instability phenomena occur under the same surface area such as surface creep above a deep rotational slide. Also, potentially affected zones such as runout zones or drop zones and the rate of movement should be mapped.

Danger maps do not include any forecasting in the strict sense such as return periods or probabilities of events but they do indicate possible events. Examples are the DUTI danger maps (DUTI, 1985), landslide inventories (Wieczorek, 1982)(Wieczorek, 1984), landslide incidence maps (Radbruch-Hall et al., 1982)(F. Taylor & Brabb, 1986).

– Level 3 - Hazard Maps

In hazard maps, the danger (potential event) and its probability of occurrence are combined. Hazard will usually be expressed on a scale. This can be in form of probabilities or in form of other scales both quantitative and qualitative (e.g. none, low, high, very high). Mapping of hazard levels is often done with different colours, symbols or a combination of both. Rather than landslide hazard maps, such maps are often called maps of relative landslide susceptibility. The estimation of probabilities or other analogous expressions can be done objectively or subjectively or through a combination of both. The best-known maps in this category are probably the French ZERMOS maps (Humbert, 1977)(Humbert, 1972)(Antoine, 1978) and various landslide susceptibility maps in the US Brabb et al. (1972); Nilsen et al. (1979); Brabb (1984). But there are many others: Viberg (1984); Dumas et al. (1984); Soulé (1980); Malgot & Mahr (1979); LPC (1978).

– Level 4 - Risk Maps

Hazard and its potential consequences are documented in these maps where consequences can be those affecting human life, having economic effects or causing environmental changes for instance. A particular surface area subject to the same hazard can face a variety of consequences, depending on land use. Usually several risk maps will, therefore, have to be developed for the same area.

The simplest and most common approach is through the overlay of land use maps on hazard maps. It is not only possible that the same danger (hazard) produces different risks dependent on the land use but the reverse, namely, different dangers (hazards) affecting the area. This is not only so with regard to landslide as mentioned earlier (surface creep, deep seated movement) but completely different hazards such as landslides, avalanches and floods may affect the same area. Risk maps can reflect this. A good example of a landslide risk map is the one produced by Bernknopf et al. (1988).

As just stated, risk maps can be produced by overlaying a hazard map with a lands map or more explicitly with a map reflecting property values. Such a map combination would not only be politically explosive but may actually oversimplify the information. It is for the reason that in many cases, actual risk maps are not produced but one proceeds direly on the hazard map to actions in form of management maps and countermeasures.

– Level 5 - Landslide Management Maps and Procedures

Hazard and risk maps are rarely the end product of landslide mapping, but they are the basis for decision making. These decisions are usually in the form of technical countermeasures, regulatory management or combinations of the two. Classic examples of regulatory management are zoning maps which, for instance, exclude some areas from habitation.

Regulatory management is often quite intricate in prescribing different permit procedures which may include detailed evaluations and additional exploration or even go so far as to prescribing particular designs (slope grades e.g.). The latter is actually a combination of regulatory and technical management. Technical mitigating measures range from a variety of stabilizing measures to protective measures such as rockfall galleries to warning devices.

To conclude this section on the mapping procedure, it is important to emphasize that in order to arrive at the management procedures or technical countermeasures, it is not necessary to go through all the preceding steps. It was already mentioned that risk maps are often omitted; similarly, zoning maps can be produced directly from hazard maps. In some cases, management procedures follow directly after danger mapping.

Chapter three
Physical modelling methodology

3.1. Introduction of geotechnical centrifuge

Geotechnical centrifuge modelling is today a consolidated experimental technique for investigating soil behaviour, slope stability, and hazard mitigation under controlled yet realistic stress conditions. Since its first applications in Cambridge during the 1960s (Schofield, 1980a), the method has expanded worldwide. More than 70 large geotechnical centrifuges are now in operation, distributed across Asia, Europe, North America, and Oceania (Fang et al., 2023). Among the largest facilities are:

- The Beijing Geotechnical Centrifuge (China), with a beam radius of 5 m and capacity up to 250 g.
- The National Research Institute for Earth Science and Disaster Resilience centrifuge (Japan), designed for seismic and rainfall-related studies.
- The UC Davis centrifuge (USA), part of the NEES/GEER network, which has contributed extensively to liquefaction and slope stability research.
- The Dundee beam centrifuge (C67-2, UK), with a 3 m radius and high versatility for both static and dynamic soil–structure problems.
- Additional facilities exist in France, Germany, Australia, and Canada, many of which are used for environmental geotechnics and rainfall-induced landslide simulations.

This global network of centrifuges reflects the growing importance of physical modelling in hazard assessment (Figure 6). Each facility differs in capacity, maximum acceleration, and payload, but all share the same objective: to reproduce prototype stress fields in reduced-scale models, thereby enabling realistic simulation of soil behaviour and failure mechanisms.

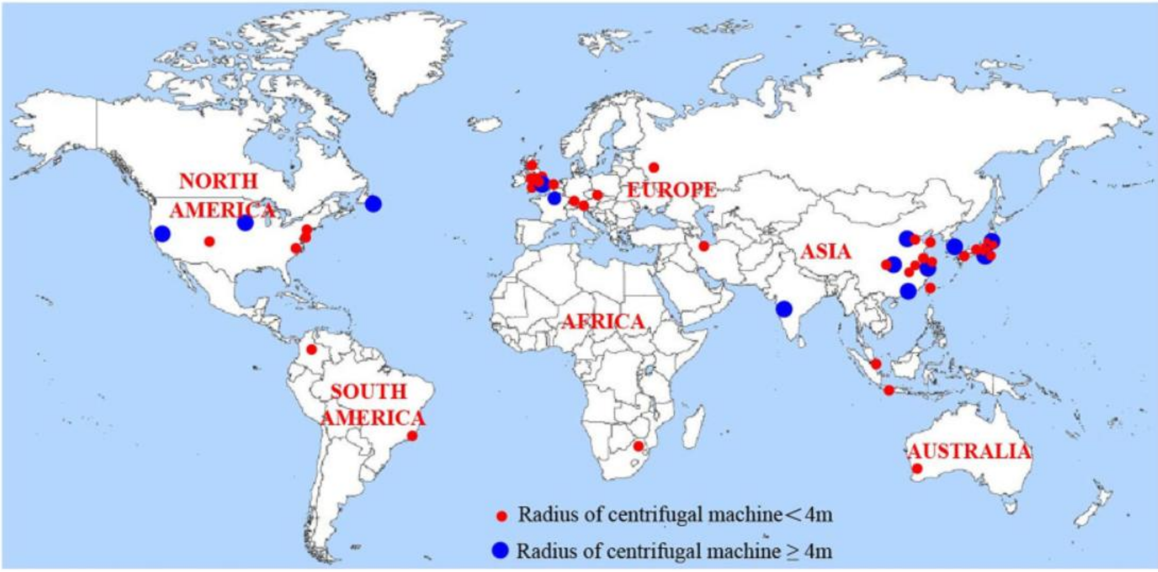

Figure 6. *Countries that have conducted centrifuge landslide tests worldwide (Fang et al., 2023).*

What distinguishes the centrifuge method is that it allows small-scale investigation of stress-controlled problems such as consolidation, rainfall infiltration, pore-water pressure generation, and progressive failure processes. Fang et al. (2023) emphasize that, compared to 1g tests, centrifuge modelling ensures realistic stress conditions, enabling highly non-linear parameters such as stiffness, strength, and dilatancy to develop with the same stress dependency as in the prototype.

In the field of landslide hazard, several physical modelling campaigns have been conducted to evaluate:

- Initiation of debris flows triggered by rainfall (Milne et al., 2011).
- Effectiveness of countermeasures such as drains and reinforcements (Fang et al., 2023).
- Interaction of foundations and piles in unstable slopes (Defae & Knappett, 2014).

All these studies confirm the value of centrifuge modelling not only for understanding instability mechanisms but also for generating experimental data with which advanced numerical models can be validated.

Rainfall infiltration and the resulting pore-water pressure changes are stress-dependent and time-dependent processes. In small 1g models, the overburden stresses are too low, leading to exaggerated apparent cohesion, incorrect infiltration velocities, and unrealistic suction dissipation rates. Centrifuge modelling solves this problem because:

- Stresses are scaled correctly, meaning shear strength, pore pressure generation, and collapse behaviour match prototype conditions.
- Timescales of infiltration and consolidation scale as $1/N^2$, so rainfall duration, wetting front propagation, and delay in failure initiation can be represented accurately.
- Hydrological boundary conditions, such as rainfall intensity or surface runoff, can be applied at model scale and translated to prototype scale with confidence.

As Fang et al. (2023) emphasize, centrifuge testing has become a unique tool for landslide hazard assessment and mitigation design, because it allows the testing of slope reinforcements (e.g., piles, drainage systems, retaining structures) under controlled rainfall events.
Facilities in China, Japan, and the UK have tested rainfall thresholds, initiation of debris flows, and countermeasures such as horizontal drains and geosynthetic reinforcements. This international experience confirms that centrifuge modelling not only reproduces the initiation mechanisms but also quantifies hazard reduction provided by mitigation strategies.

3.2. Principles of centrifuge testing

Geotechnical model testing in engineering problems is typically conducted at a (1:N) scale, where N is the scaling factor. The use of small-scale (1-g) models is generally limiting in geotechnical engineering, since soil behaviour depends on effective stress, and these stresses are N times smaller in a 1:N scale model (Wood, 2004). To preserve the correct prototype soil behaviour (i.e., identical stress and strain conditions in the model), a centrifuge can be used to increase the gravity field magnitude (by a factor of N) to offset the stress reduction caused by the smaller size Figure 7.

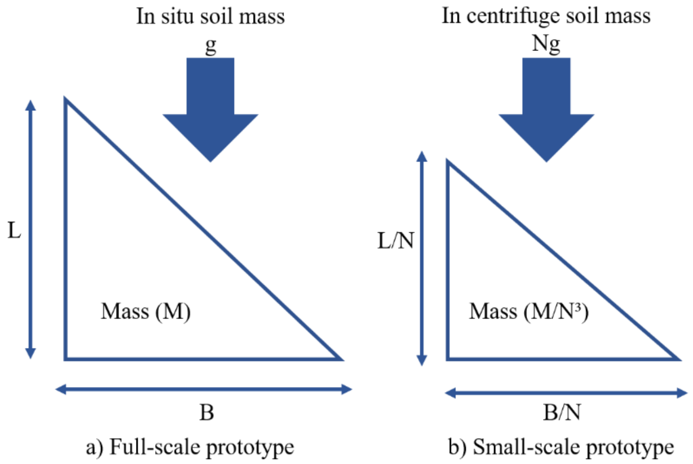

Figure 7. *Basic principal of centrifuge testing of reduced scale models (Defae & Knappett, 2014).*

The fundamental principle of centrifuge modelling is stress similitude. In a real/full scale prototype, the vertical total stress σ and the vertical strain ε in the soil mass are:

$$\sigma = \frac{M \cdot g}{LB} \tag{3.1}$$

and

$$\varepsilon = \frac{\Delta \mathrm{L}}{L} \tag{3.2}$$

In a reduced/small-scale model if it is tested at Ng, in the centrifuge with all dimensions reduced by the N, the stress and strains become:

$$\sigma = \frac{\frac{M}{N^3} \cdot N \cdot g}{\frac{L}{N} \cdot \frac{B}{N}} = \frac{M \cdot g}{L \cdot B} \tag{3.3}$$

$$\varepsilon = \frac{\frac{\Delta \mathrm{L}}{N}}{\frac{L}{N}} = \frac{\Delta \mathrm{L}}{L} \tag{3.4}$$

so the stress and strain in the centrifuge are equivalent to that in the full scale prototype. This means that the soil in the model experiences the same level of stress as in the prototype, allowing the reproduction of the same strength, deformability, and hydro-mechanical behaviour.

The force involved during operation is subjected to a centrifugal acceleration to the soil model by spinning the model in the centrifuge in a horizontal plane at a prescribed angular velocity at a centrifuge radius r:

$$a_r = \omega^2 r \tag{3.5}$$

where ω is the angular velocity. This means that the bottom of the soil model, located further from the axis of rotation, experiences a slightly greater acceleration than the top.

Consequently, vertical stress in the model increases non-linearly with depth, producing what is known as radial distortion, the resultant acceleration acting on the model is:

$$a = \sqrt{(\omega^2 r^2)^2 + g^2} \tag{3.6}$$

For a 1: N scale model, the angular velocity is selected such that:

$$a = N \cdot g \tag{3.7}$$

Defae & Knappett (2014) show that this effect becomes significant only when the model height is a large fraction of the centrifuge radius. In Table 2, the conventional scaling laws between model parameters and their full-scale prototype equivalents are summarized, taking into account that $g^* = {}^{1}/_{L^*} = N$.

Table 2. *Scaling laws for centrifuge testing (Schofield, 1981;Kutter, 1994; Defae & Knappett, 2014).*

Parameter General	Dimensions	Scaling laws Model/ Prototype	
Length	L	$\frac{1}{N}$	$L^* = {}^{L_m}/_{L_p} = {}^{1}/_{N}$
Area	L^2	$\frac{1}{N^2}$	
Volume	L^3	$\frac{1}{N^3}$	
Density	$\frac{M}{L^2}$	1	$\rho^* = {}^{\rho_m}/_{\rho_p} = 1$
Mass	M	$\frac{1}{N^3}$	$M^* = (L^*)^3 = \left({}^{1}/_{N}\right)^3$
Stress/ Moduli/ Pressure	$\frac{M}{LT^2}$	1	$\sigma^* = {}^{\sigma_m}/_{\sigma_p} = 1$
Strain	-	1	
Force	$\frac{ML}{T^2}$	$\frac{1}{N^2}$	$F^* = (L^*)^2 = \left({}^{1}/_{N}\right)^2$
Bending moments	$\frac{ML^2}{T^2}$	$\frac{1}{N^3}$	
Seepage velocity	$\frac{L}{T}$	$\frac{1}{N}$	

Dynamic Events			
Acceleration	$\frac{L}{T^2}$	N	$a^*_{dyn} = g^* = {}^1/_{L^*} = N$
Velocity	$\frac{L}{T}$	1	$v^*_{dyn} = \frac{L}{T} = \frac{{}^1/_N}{{}^1/_N} = 1$
Time (dynamic)	T	$\frac{1}{N}$	$t^*_{dyn} = L^* = {}^1/_N$
Time (consolidation/ seepage/ diffusion)	T	$\frac{1}{N^2}$	$t^*_{con/see/dif} = (L^*)^2 = ({}^1/_N)^2$
Frequency	$\frac{1}{T}$	N	
Displacement	L	$\frac{1}{N}$	

The Dundee centrifuge has the following technical specifications (Figure 8):

- C67-2 machine by Actidyn (France);
- Radius of 3 m, acceleration range of 5–130 g;
- Maximum payload capacity of 1500 kg at 100 g;
- Platform size of 0.8 × 1.0 m, usable height of 1.5 m;
- Data transmission via up to 80 electrical channels and optical fibre at 100 MHz;
- Automatic balancing within ±20 kN.

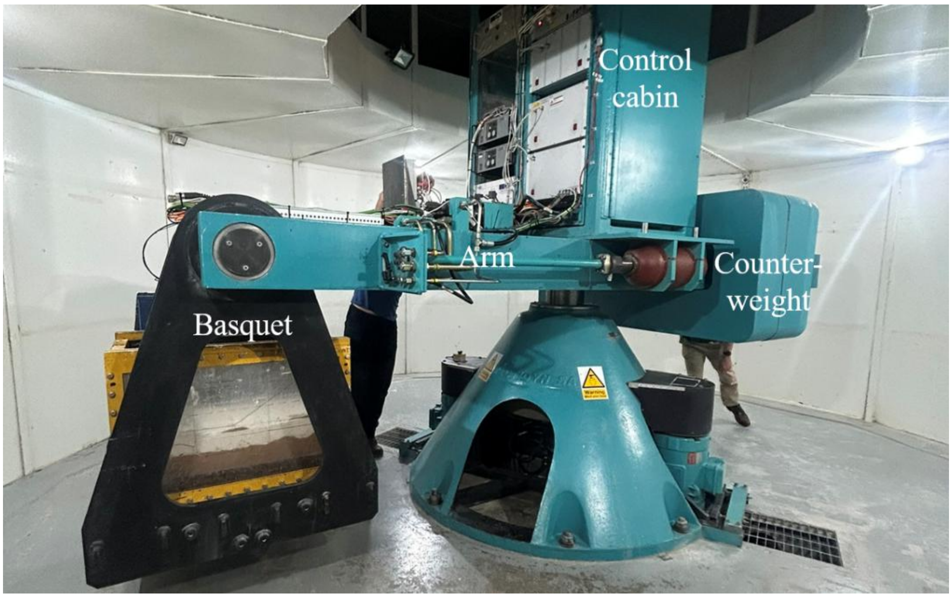

Figure 8. *University Dundee geotechnical centrifuge.*

3.3. Centrifuge considerations

3.3.1. Particle size

One of the fundamental considerations in centrifuge modelling is the relationship between particle size and model scale. Soil must be treated as a continuum for similitude to hold, which requires that the representative dimensions of the model (slope height, embankment thickness, or drainage layer) are significantly larger than the average particle size. If the model dimensions are not sufficiently scaled relative to the grain size, scaling errors arise, leading to unrealistic strength, permeability, or deformation behaviour.

Ovesen´s (1979) classical work suggested that a minimum ratio of model dimension to particle size of about 15–20 is required to avoid scale effects. In practice, many centrifuge facilities—including Dundee—recommend ratios closer to 30–50 for sandy soils to ensure realistic seepage and shear banding. Defae & Knappett (2014) notes that this criterion is critical when using uniform silica sands such as HST95, whose median diameter $D50 \approx 0.12$ mm easily satisfies the continuum requirement for models scaled at 1:50 or 1:100.

For rainfall-induced slope failures, particle size considerations become even more relevant because infiltration rates depend on hydraulic conductivity, which is a function of grain size distribution. As Fang et al. (2023) point out, centrifuge modelling of rainfall-triggered landslides must balance two competing requirements: (i) using natural or synthetic soils whose particle-size distribution is representative of field conditions, and (ii) ensuring that grain size does not impose artificial drainage behaviour at model scale. For this reason, well-characterised sands (HST95) and engineered mixtures (KSS541) are widely used, since they replicate both the mechanical and hydraulic behaviour of natural slopes under scaled stresses.

3.3.2. Radial distortion

In centrifuge modelling, the acceleration field is not perfectly uniform but varies with radius. This means that the bottom of the soil model, located further from the axis of rotation, experiences a slightly greater acceleration than the top. Consequently, vertical stress in the model increases non-linearly with depth, producing what is known as radial distortion. As shown by Stewart (1989), vertical stress variation depends on the squared difference between the radius to the model surface and that to a given point (z), in accordance with the equation:

$$\sigma_v = \rho\omega^2 = \int_{r_1}^{r_2} r dr = \frac{1}{2}\rho\omega^2(r_2^2 - r_1^2) \tag{3.8}$$

where r_1 denotes the radius from the centrifuge rotation axis to the top of the model, and r_2 corresponds to the radius measured to depth z within the model (Figure 9).

Kutter (2024) and Knappett (2010) reinforces this by demonstrating mathematically that the difference in acceleration across a typical model depth is minimal for beam centrifuges, provided model depth < R/10, where R is the radius measured to the base of the container. In Dundee tests the maximum model depth (~280 mm) satisfies this for R = 3.5 m.

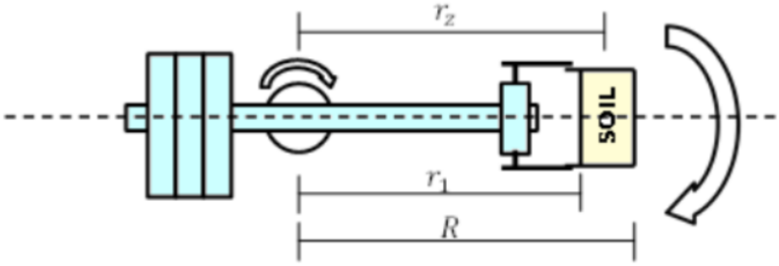

Figure 9. *Radii definition for radial stress field distortion of the University Dundee geotechnical centrifuge (Defae & Knappett, 2014).*

For rainfall tests, radial distortion must be considered carefully because pore-pressure profiles are depth-dependent. A non-uniform acceleration could, in principle, alter infiltration gradients and consolidation behaviour. However, Fang et al. (2023) and Milne et al. (2011) report that in practice the effect is negligible for rainfall-induced slope failures, since hydrological processes are more sensitive to hydraulic conductivity and rainfall intensity than to the minor stress deviations introduced by radial distortion.

Thus, while radial distortion is a theoretical limitation of all centrifuges, its impact in rainfall-infiltration modelling at Dundee is minimal and can be safely ignored if geometric ratios are respected.

In free-swinging platform centrifuges (beam centrifuges), such as the Dundee C67-2, the platform automatically aligns so that the resultant acceleration remains perpendicular to the base of the model, thereby avoiding gravitational distortion.

3.3.3. Gravitational distortion

Another source of potential error in centrifuge testing is gravitational distortion, which arises when the resultant acceleration vector is not perfectly perpendicular to the model base. In beam centrifuges with a free-swinging platform (such as the C67-2), this problem is effectively eliminated: the platform aligns itself so that the resultant of centrifugal and gravitational accelerations acts vertically relative to the model container.

Kutter (2024) illustrates that gravitational distortion is primarily a concern for fixed-platform centrifuges, where off-axis loading introduces artificial shear stresses. In contrast, beam centrifuges correct automatically through swing-arm alignment. Defae & Knappett (2014) confirm that angular distortion in Dundee’s centrifuge is minimal (on the order of 2–3° for typical model widths), ensuring that slope models are subjected to a uniform acceleration field normal to their base.

For rainfall-induced slope studies, the elimination of gravitational distortion is essential because infiltration fronts and wetting lines must propagate in a truly vertical hydraulic gradient. If distortion were significant, water could migrate laterally, creating artefacts in suction and pore-pressure distribution. By using a free-swinging platform, Dundee ensures that infiltration processes during rainfall simulation follow the correct prototype vertical gradient.

3.4. Soil properties and preparation

3.4.1. Sand HST95

The HST95 sand, widely used in centrifuge model testing, has been the subject of extensive constitutive modelling studies aimed at replicating its mechanical response under drained conditions. Brinkgreve et al., (2010) highlight that the relative density (RD) plays a pivotal role in defining both stiffness and strength parameters for quartz sands, and consequently for HST95. The relative density is defined as:

$$RD = \frac{e_{max} - e}{e_{max} - e_{min}} \cdot 100\% \tag{3.9}$$

where e is the current void ratio, e_{max} the maximum void ratio (loosest state), and e_{min} the minimum void ratio (densest state).
From RD, it is possible to derive approximate unit weights:

$$\gamma_{unsat} = 15 + 4.0\frac{RD}{100}\left[{}^{kN}/_{m^3}\right] \tag{3.10}$$

$$\gamma_{sat} = 19 + 1.6\frac{RD}{100}\left[{}^{kN}/_{m^3}\right] \tag{3.11}$$

These values illustrate the direct link between density state and mechanical response, which is fundamental when scaling centrifuge models where sand density is carefully controlled.

Similarly, the reference stiffness moduli for primary loading, unloading/reloading, and oedometer compression are expressed as linear functions of RD, while the initial shear modulus is adjusted by:

$$E_{50}^{ref} = 60000 \cdot \frac{RD}{100}\left[{}^{kN}/_{m^2}\right] \tag{3.12}$$

$$E_{oed}^{ref} = 60000 \cdot \frac{RD}{100}\left[{}^{kN}/_{m^2}\right] \tag{3.13}$$

$$E_{ur}^{ref} = 180000 \cdot \frac{RD}{100}\left[{}^{kN}/_{m^2}\right] \tag{3.14}$$

$$G_{0}^{ref} = 60000 + 68000 \cdot \frac{RD}{100}\left[{}^{kN}/_{m^2}\right] \tag{3.15}$$

For the strength parameters Brinkgreve et al. (2010) also provide empirical formulas linking RD to effective friction angle and dilatancy:

$$\varphi' = 28 + 12.5\frac{RD}{100}\ [°] \tag{3.16}$$

$$\psi = 2 + 12.5\frac{RD}{100}\ [°] \tag{3.17}$$

In addition, the failure ratio R_f, which governs the mobilization of strength in HS_{small}, is expressed as:

$$R_f = 1 - \frac{RD}{800} \tag{3.18}$$

These formulations capture the well-established increase in strength and dilatancy with increasing relative density. For medium-dense states, dilatancy remains modest, while very dense states approach significant volumetric expansion upon shearing.

The advantage of using these empirical relations is that they allow direct translation of laboratory-determined relative density into FEM constitutive parameters without extensive calibration. This is particularly relevant for centrifuge tests, where sand is pluviated or compacted to a target RD to replicate in-situ density conditions. In the case of HST95, applying Brinkgreve et al.´s formulations ensure consistent scaling between physical and numerical models, enabling a more realistic reproduction of stiffness degradation, shear band formation, and overall slope stability behaviour.

Table 3 summarizes the values obtained for HST95 sand at three representative densities, illustrating the variation of stiffness and strength parameters. These results confirm the well-established trend that denser sand exhibits higher stiffness, frictional strength, and dilatancy, consistent with experimental observations and numerical modelling requirements.

Table 3. *Estimated stiffness and strength parameters for HST95 sand (Brinkgreve et al., 2010).*

Relative Density RD	γ_{unsat} $\left[{}^{kN}/_{m^3}\right]$	γ_{sat} $\left[{}^{kN}/_{m^3}\right]$	E_{50}^{ref} $\left[{}^{kN}/_{m^2}\right]$	E_{oed}^{ref} $\left[{}^{kN}/_{m^2}\right]$	E_{ur}^{ref} $\left[{}^{kN}/_{m^2}\right]$	G_{0}^{ref} $\left[{}^{kN}/_{m^2}\right]$	φ' [°]
40%	16.6	19.6	24000	24000	72000	87200	33.0
60%	17.4	20.0	36000	36000	108000	102800	35.5
80%	18.2	20.3	48000	48000	144000	116400	38.0

These density-dependent formulations are particularly valuable for centrifuge modelling, where relative density can be controlled through air pluviation or compaction. They ensure that the adopted constitutive parameters in numerical simulations, such as those conducted with PLAXIS, are representative of the physical model behaviour (Brinkgreve et al., 2010).

HST95 (Congleton) silica sand is a uniformly graded, rounded fine sand widely used in Dundee modelling. The HST95 silica sand, according to Defae & Knappett (2014), has been extensively characterized in terms of its physical properties. The material has a specific gravity (G_s) of 2.63 and is composed of rounded particles, reflecting its origin and preparation. Its particle size distribution is relatively uniform, with characteristic diameters of D_{10}=0.09, D_{30}=0.12, and D_{60}=0.17 mm, yielding a coefficient of uniformity (C_u) of 1.9 and a coefficient of curvature (C_z) of 1.06. The sand exhibits a maximum dry density of 17.58 kN/m³ and a minimum dry density of 14.59 kN/m³, with an optimum dry density of 15.35 kN/m³ under standard compaction conditions. Correspondingly, the void ratio ranges from e_{max}=0.769 to e_{min}=0.467. These parameters confirm that HST95 is a fine, uniformly graded silica sand, well suited for centrifuge model preparation due to its consistent packing behaviour and reproducible density states.

In centrifuge modelling, achieving a controlled and uniform soil density is essential for ensuring reproducible behaviour across tests. ***Air pluviation*** was the primary technique used to place granular soils such as HST95 silica sand into the model container. Although this research focuses on cohesive soils, understanding the placement of granular layers is relevant because they often form part of engineered mixtures or drainage strata within slope models.

The pluviator consisted of a 540 mm slot capable of covering the full width of the strongbox, with a hopper mounted on a linear guide frame. This allowed the hopper to be moved at approximately constant speed along the container, maintaining a consistent drop height—an important factor for achieving uniform density across the slope surface. The sand was deposited using a slot pluviator (Figure 10), a device widely employed at Dundee and previously adopted by Lauder (2011) and Bertalot (2013).

Figure 10. *Sand deposited with slot pluviator at the Laboratory of Geotechnical University of Dundee.*

Relative density was adjusted by varying the slot opening: calibration tests in a controlled-volume box were performed to establish the relationship between slot width, drop height, and resulting density. This calibration ensured that soil placement was both uniform and repeatable, thereby reducing preparation-related variability in the model response. In Al-Defae´s work it was air-pluviated to ~55% relative density using a calibrated slot pluviator to achieve uniform density.

Although HST95 features prominently in dynamic studies, it also serves in static (rainfall-related) models as a granular drainage layer or upper crust where needed, in this test was used as a granular drainage layer.

3.4.2. Mix KSS541

While granular soils such as HST95 are typically placed in centrifuge models by air pluviation, cohesive soils require a different preparation method to ensure uniformity and reproducibility. The KSS541 mixture, developed and frequently used at the University of Dundee, consists of 50% Kaolin clay, 40% HST95 silica sand, and 10% Silica silt (A50) by dry weight. The mixture is prepared as a ***slurry*** at an initial moisture content of 50%, which allows the soil to be poured into the strongbox in a fluid state, eliminating the risk of segregation and enabling controlled subsequent consolidation.

The material properties were characterised through a suite of laboratory tests, including drained triaxial compression tests to establish effective strength parameters, and critical state analysis to define the soil's long-term stress–strain behaviour.

From the triaxial results, the critical state friction angle of the mixture was determined as approximately 25°, while the drained effective strength parameters were measured as ϕ'=18.2° and c'=5.2 kPa. The saturated unit weight was reported as around 18.8–19.1 kN/m^3, with typical values of 18.8 kN/m^3 at 100 mm depth after consolidation. These values provide a reliable baseline for the stability analysis of slopes subjected to rainfall infiltration.

The soil behaviour can be interpreted from two key graphical representations:

Critical State Line (CSL): in the Figure 11 plots the deviatoric stress q against the mean effective stress p'. The CSL obtained from drained triaxial tests shows a linear relation with a slope M=0.746, expressed as q=0.75p' with $R2$=1.00. This perfect fit confirms the consistency of the critical state framework for the KSS541 mixture, indicating that the soil reaches a well-defined shear strength envelope at large strain. The CSL is fundamental for constitutive modelling, as it defines the boundary between stable and failure states.

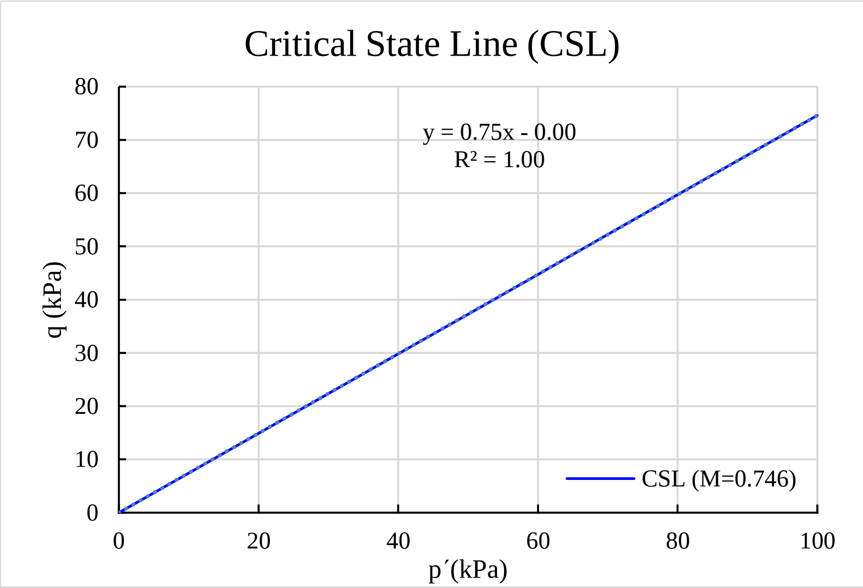

***Figure 11**. Critical State Line (CSL) for the KSS541 mixture obtained from drained triaxial compression tests. The relationship between deviatoric stress q and mean effective stress p' defines a linear CSL with slope M=0.746, confirming the critical state behaviour of the soil.*

Mohr–Coulomb failure envelope: in the Figure 12 presents the drained strength envelope in τ-σ' space, constructed from the Mohr's circles of the triaxial test results. The line represents the effective shear strength criterion τ=c'+σ'tanϕ', with c'=5.2 kPa and ϕ'=18.2°. This envelope illustrates that the mixture possesses moderate effective cohesion, typical of kaolin-based materials, and relatively low friction angle compared to clean sands, consistent with its cohesive character. The location of the Mohr's circles confirms that failure stresses align well with the predicted linear envelope, providing confidence in the parameter selection for slope stability modelling.

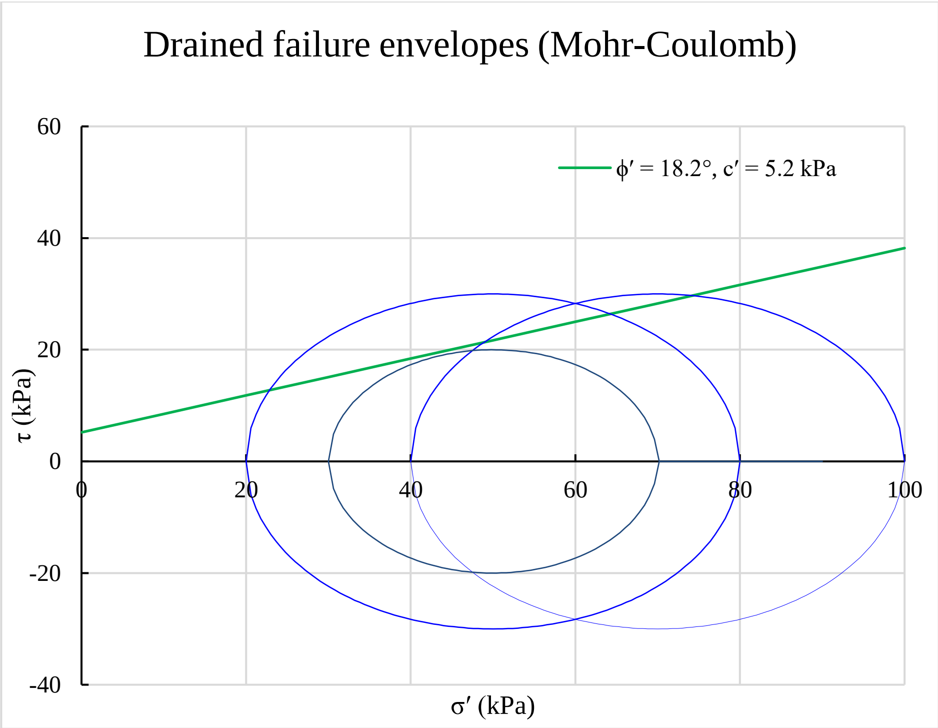

***Figure 12**. Drained Mohr–Coulomb failure envelope for the KSS541 mixture. The effective strength parameters (ϕ'=18.2°, c'=5.2 kPa) were derived from drained triaxial tests, with Mohr's circles showing good agreement with the linear failure criterion.*

The relatively high cv of KSS541 shortens in-flight consolidation, enabling practical replication of saturated cohesive slopes prior to controlled wetting. Its clay fraction and measured critical/friction parameters allow calibration of hydro-mechanical models that track suction loss and strength degradation during infiltration.

A critical step in preparing cohesive soils for centrifuge modelling is in-flight consolidation. After deposition as a slurry, the KSS541 layer undergoes self-weight consolidation under the elevated g-level, reducing its thickness from an initial ~390 mm to ~300 mm, corresponding to a 25% reduction in height.

This process replicates the stress history of natural clays that have been subjected to decades of loading in the field. The importance of consolidation lies in producing a soil deposit with realistic effective stresses, pore-water distribution, and stiffness comparable to that of a clay slope in situ.

The centrifuge allows researchers to accelerate geological time. Because consolidation and other diffusion-controlled processes scale with $1/N2$, where N is the g-level, the elapsed model time corresponds to a much longer prototype time.
For example, at 50 g, one hour of consolidation in the centrifuge is equivalent to approximately $50^2 = 2500$ hours (≈ 104 days) at prototype scale. Thus, 8 hours of centrifuge consolidation at 50 g corresponds to more than 830 days, or approximately 2.3 years, of natural consolidation time. This time scaling explains why in-flight consolidation is indispensable: it allows the centrifuge model to replicate soil conditions that would otherwise require decades to develop in the field.

3.5. Instrumentation

3.5.1. Rainfall equipment

The rainfall system used in this study consists of a pressure-fed distribution rail with eight interchangeable outlet positions mounted beneath the strongbox lid. The outlets (fine spray nozzles) can be reconfigured on a circular bolt-pattern to alter plan-view spacing and coverage; for the present programme the central positions were selected to promote spatial uniformity over the slope crest and face (Figure 13).

Water is supplied from a pressurized pump through a manifold with inline pressure gauge and quick-release couplings, allowing precise control of discharge and easy re-positioning of individual outlets. The eight jets impinge on the model surface as a fine spray, forming a quasi-uniform artificial precipitation that can be scheduled in sequences to replicate short, intense storms or longer, moderate events.

Figure 13. *Rainfall equipment: aluminum lid with service ports and manifold (leak-check under pressure); distribution rail and quick-connects; eight downward-facing nozzles; assembled strongbox with rainfall rail and instrumentation mounts.*

Design choices and calibration follow best practice from centrifuge rainfall simulators. First, nozzle arrays are widely adopted because they are robust at elevated g, and their discharge can be controlled by pump pressure and orifice size; uniformity is verified by spatial catchment tests and is typically summarized by the Christiansen coefficient of uniformity (CU) (e.g., nozzle-type simulators for landslide studies) (Whittle et al., 2012).

Second, pressurized systems facilitate stable, repeatable flow and allow intensity to be indexed to both pump setting and g-level; pressure losses along the feed line and the relationship between line pressure, nozzle flow rate, and delivered rainfall at up to 100 g have been documented in centrifuge environmental-chamber developments for infrastructure resilience testing, providing a template for calibration curves (pressure → prototype mm h^{-1}) (Lee et al., 2020).

Third, several centrifuge groups report environmental chambers that combine water input with air control to manage evaporation and temperature, thereby enabling long, multi-event hydrologic programmes; Dundee's climatic chamber work on clay embankments is a representative example, demonstrating controlled inundation/evaporation and long-term cycling under high-g conditions (Hudacsek et al., 2015).

Alternative rainfall devices exist—e.g., perforated-hose arrays placed just above the slope surface, where intensity depends on g-level and supply flow rate; these devices confirm that simple, modular systems can reliably trigger slope failures in centrifuges when properly calibrated (S. Wang & Idinger, 2021). More sophisticated air-atomizing nozzles based on a modified Mariotte principle have also been used to minimize "blind zones" and Coriolis effects on droplet trajectories, again emphasizing the need to match nozzle layout to box planform and test objectives (Bhattacherjee & Viswanadham, 2018).

3.5.2. Data acquisition

High-g testing requires data systems that remain stable under rotation and provide synchronous, low-noise signals. Canonical centrifuge Data Acquisition System (DAQ) architectures route transducer outputs (pore-pressure, displacement, strain) to strain amplifiers, then through electro-optic converters and multi-port fibre-optic rotary joints to the control room for digitization and storage; such layouts were standardized in large facilities in the late 1990s and continue to underpin modern systems, ensuring reliable transmission during spin. A data flow typical of these systems (dynamic and static channels, electro-optic conversion, rotary joint, workstation logging) is documented in Centrifuge 98 (Kimura et al., 2000) and remains a relevant reference architecture for present practice.

For optical displacement measurement, centrifuge groups have long used on-board cameras with image processing to obtain quantitative kinematics. The classical workflow comprises (i) in-spin image capture at fixed frame intervals, (ii) digitization, (iii) image processing and feature tracking (from fiducial targets or natural texture), and (iv) derivation of vector displacement fields and strain contours; Davies & Jones (1998) developed image acquisition with on-board film cameras, digitizing frames and processing them with CAD software to derive displacement vectors and strain fields.

Their experiments demonstrated how photographic frames could be transformed into displacement plots of sand and clay slopes, capturing progressive deformation. Subsequent advances introduced camera calibration and multi-camera bundle adjustment to correct for perspective and refraction errors, yielding precise 3D displacement fields (Cooper & Robson, 1996).

These methods complement point transducers: while sensors provide high-resolution pore pressure or strain data, image-based systems capture global deformation patterns, particularly relevant for rainfall-induced failures where instability evolves progressively (Fang et al., 2023).

Chapter four

Development of FEM-based model for determining slope stability

4.1. Numerical modelling tools and approaches

The finite element method (FEM) provides a rigorous continuum-mechanics framework to analyse slope stability under complex geometries, stress paths, and hydro-mechanical coupling. Zienkiewicz et al. (2014) and Potts & Zdravkovi'c (1999) formalised the governing equations for deformation, seepage, and consolidation, enabling stress–strain computation up to failure and beyond. Compared with traditional limit-equilibrium methods, FEM does not assume a predefined slip surface and can capture progressive failure, strain localisation, and the influence of pore-pressure transients driven by infiltration (Zienkiewicz et al., 2013)(Potts & Zdravkovi'c, 1999).

Modern geotechnical codes operationalise these theories with robust algorithms and soil models. PLAXIS 2D, for example, is a specialised FEM program for deformation, stability, and groundwater flow analyses under plane-strain or axisymmetric conditions. It incorporates fully coupled flow–deformation calculations (including unsaturated flow with van Genuchten–type soil–water characteristic curves) and strength-reduction stability assessment (Bentley Systems, 2018b)(Bentley Systems, 2023).

Various numerical platforms are available for geotechnical analysis, including FLAC/FLAC3D (Itasca), GeoStudio/SLOPE-W, ABAQUS, MIDAS GTS NX and OpenSees, each offering different capabilities for advanced constitutive modelling, hydro-mechanical coupling, or full 3D representation. For this research, PLAXIS was selected owing to its widespread use in geotechnical engineering practice, its accessibility within the hosting institution, and its well-established modules for seepage, consolidation and soil–structure interaction. This combination of availability, modelling versatility, and computational efficiency made PLAXIS particularly suitable for integrating the centrifuge test observations with the numerical simulations developed for the Himera I case study.

4.1.1. 2D and 3D modelling

Two-dimensional (2D) models are widely used in geotechnical practice because they provide a balance between computational efficiency and accuracy. Under the plane strain assumption, 2D models are particularly suitable for long slopes with relatively uniform conditions along their width. Numerous studies show that 2D FEM combined with strength reduction can provide reliable estimates of factor of safety and deformation patterns for rainfall-induced failures (Potts & Zdravkovi'c, 1999)(Khan, 2023). However, 2D analyses neglect out-of-plane effects such as lateral confinement, irregular slope geometry, and localised drainage, which may lead to conservative or non-conservative results depending on the geometry.

Three-dimensional (3D) models overcome these limitations by explicitly simulating slope width, lateral variability in geology, and interaction with structural elements such as piles or bridge piers. Wu et al. (2024) and Z. Wang et al. (2020) demonstrated that 3D probabilistic analyses can yield factors of safety that differ significantly from 2D predictions, especially in cases of heterogeneous soils or complex boundaries. Nevertheless, 3D analyses demand substantially higher computational effort and more detailed site data. For this reason, a pragmatic workflow is to adopt 2D FEM for parametric analysis and back-analysis and use 3D FEM selectively where geometry and infrastructure interaction justify it.

Constitutive soil models

The choice of soil model is as critical as dimensionality. In PLAXIS 2D, widely used models include (Table 4):

- Mohr–Coulomb model (MC): The simplest elastoplastic model, defined by five parameters:
  - effective cohesion (c'),
  - friction angle (ϕ'),
  - dilatancy angle (ψ),
  - Young's modulus (E), and
  - Poisson's ratio (ν).

  It assumes perfectly plastic behaviour with linear failure envelope and constant stiffness. Advantages include simplicity, transparency, and direct linkage with classical soil mechanics parameters. However, it cannot represent stress-dependent stiffness, strain hardening/softening, or creep, and tends to overpredict plastic zones in soft soils (Brinkgreve et al., 2010)(Potts & Zdravkovi'c, 1999). Despite these limitations, Mohr–Coulomb is widely adopted in slope stability assessments and remains appropriate for back-analyses and first-order evaluations, particularly when field data are limited.
- Hardening Soil model (HS): A more advanced model incorporating stress-dependent stiffness through three moduli: secant stiffness in drained triaxial loading (E50), oedometer stiffness (Eoed), and unloading/reloading stiffness (Eur). It accounts for plastic strain hardening in shear and compression, better simulating stiffness nonlinearity and dilatancy (Brinkgreve et al., 2010). HS is superior for predicting settlements, progressive failure, and cyclic loading, but requires extensive laboratory testing (triaxial, oedometer) for calibration.
- Hardening Soil with Small-Strain stiffness (HS_{small}): Extends HS by including small-strain stiffness decay with strain level, allowing accurate reproduction of shear modulus at small deformations (G_{max}). This is important in seismic and vibration analyses but less critical for rainfall-induced static failures.

– Other advanced models: The Soft Soil and Soft Soil Creep models capture time-dependent consolidation and creep in clays, while Hypoplasticity and Bounding Surface Plasticity models reproduce complex cyclic behaviour. These models are generally unnecessary for first-order rainfall-induced slope analysis but may be applied in long-term consolidation studies.

Table 4. *Comparative table of the soil constitutive models (Bentley Systems, 2023).*

Model	Key Parameters	Advantages	Limitations	Typical Applications
Mohr-Coulomb (MC)	c', φ', ψ, E, ν	Simple, robust, few parameters; direct link to classical soil mechanics; widely used for slope stability and back-analysis.	Linear failure envelope; constant stiffness; cannot capture strain softening, stiffness degradation or creep.	More complex calibration; parameters often unavailable in routine investigations; not always necessary for static rainfall-induced failures.
Hardening Soil (HS)	E50, Eoed, Eur, c', φ', ψ, ν	Captures stress-dependent stiffness and strain hardening; more realistic settlements and progressive failure; suitable for advanced slope and foundation analysis.	Requires extensive lab testing (triaxial, oedometer) for calibration; higher computational demand.	Foundation settlement, excavation support, embankments, progressive failure analysis.
Hardening Soil Small-Strain (HSsmall)	E50, Eoed, Eur, c', φ', ψ, ν, G0 (small-strain stiffness)	Includes small-strain stiffness decay; accurately models Gmax and shear modulus reduction curves; important for cyclic and dynamic problems.	More complex calibration; parameters often unavailable in routine investigations; not always necessary for static rainfall-induced failures.	Seismic and vibration problems, dynamic soil–structure interaction, cyclic loading studies.

Advantages and limitations

The Mohr–Coulomb model's main advantage lies in its simplicity, robustness, and clear interpretability, making it suitable for the back-analysis of the Himera I slope, where the objective is to reproduce the overall failure mechanism induced by rainfall rather than to simulate small-scale deformation details. Its parameters are well constrained by the available geotechnical dataset, which includes effective shear strength values but lacks the detailed stress–strain information required to reliably calibrate more advanced constitutive models. For this reason, Mohr–

Coulomb provides an appropriate balance between model transparency, computational efficiency, and consistency with the centrifuge observations used to guide the numerical calibration.

However, important limitations must also be acknowledged. The Mohr–Coulomb constitutive law represents soil behaviour using a linear strength envelope and constant stiffness parameters, which restricts its ability to capture strain-softening, stiffness degradation, pore-pressure–dependent stiffness, or progressive failure mechanisms typically observed in slopes subjected to prolonged infiltration. Furthermore, although the FEM framework enables hydro-mechanical coupling, the adopted model cannot reproduce detailed strain localisation or the development of shear bands with the same accuracy as more advanced formulations such as Hardening Soil, Hardening Soil Small, or other stress-path–dependent plasticity models. The numerical model is also implemented in a two-dimensional plane-strain configuration, which inherently neglects potential three-dimensional effects associated with the geomorphological setting of the Himera I slope.

Additional limitations arise from the calibration process itself. Since the FEM model was calibrated using centrifuge test data, scale-related uncertainties may affect the reproduction of pore-pressure build-up and deformation patterns, particularly in relation to hydraulic heterogeneities or preferential flow paths that are difficult to fully represent numerically. Boundary conditions must also be idealised to replicate the experimental scenarios, meaning that natural spatial variability in permeability and structure is not fully captured. These constraints emphasise that the FEM simulations presented here should be interpreted as approximations of the physical processes rather than exact replications of prototype behaviour.

Despite these limitations, the Mohr–Coulomb model was considered adequate for the aims of this research: identifying the key rainfall-induced triggering mechanisms, analysing the evolution of pore pressures and deformations that precede failure, and reproducing the global instability mode observed in the centrifuge and at the Himera I site. Future work may benefit from the implementation of more advanced constitutive models to refine the deformation predictions or to investigate post-peak behaviour, but such enhancements would require a more extensive laboratory database and additional numerical calibration efforts.

Calculation type

In PLAXIS, a calculation type specifies the governing field equations that the finite-element (FE) solver activates in a given phase, and how those equations are time-integrated and coupled (or not) with groundwater flow. Typical choices are:

- Plastic (deformation);
- Consolidation;
- Safety (SSR);
- Dynamics;
- Fully coupled flow–deformation;
- Dynamics with consolidation

Each type implies a different set of unknowns, constitutive updates, damping/viscous terms, and boundary-condition handling, and therefore is suited to different geotechnical problems (PLAXIS BV, 2004)(Bentley Systems, 2024).

The most basic calculation option is the *Plastic (deformation) analysis*, which evaluates static equilibrium under external loads. Here, the finite element formulation solves the balance equation:

$$\nabla \cdot \sigma + b = 0 \tag{4.1}$$

where σ is the stress tensor and b is the body force vector (e.g., gravity).

In this case, soil behaviour is governed by an elastoplastic constitutive model, but transient pore-water effects are ignored, that means no time-dependent storage term from the fluid phase. This approach is appropriate when pore pressure changes are negligible (flow can be "switched off" (drained)), or when a steady-state water distribution is prescribed (assigned heads/lines), that means quasi-static deformation under staged construction with no transient pore-pressure calculation; such as in short-term excavation stages, embankment construction under drained conditions, or retaining walls with fixed groundwater levels. The outputs that can be obtained are displacements, stresses, plastic strains; optional steady seepage results if a steady head distribution is imposed (Bentley Systems, 2016).

A more advanced option is the *Consolidation analysis*, which incorporates time-dependent dissipation of pore pressures and soil deformation through the Biot consolidation framework (Terzaghi–Biot style) The formulation couples the equilibrium of the soil skeleton with fluid mass conservation:

$$\nabla \cdot \sigma + b = 0, \frac{\partial u}{\partial t} + \nabla \cdot (k \nabla h) = 0 \tag{4.2}$$

where u is the pore-water pressure, k the hydraulic conductivity, and h the hydraulic head. This enables simulation of primary consolidation under loads, staged construction on soft clay, settlement under embankments, pore pressure dissipation after rapid drawdown, rainfall-infiltration transients where deformation–pore-pressure feedback is important but full nonlinearity of unsaturated flow is moderate

The main advantage is the capacity to reproduce both mechanical and hydraulic transients, although unsaturated conditions are simplified compared to more advanced flow formulations. PLAXIS implements a u–p formulation with Richards-type unsaturated flow options; the time step controls diffusion. The outputs that can be obtained are time histories of settlement, pore pressures, degree of consolidation; consolidation coefficients inferred from response (Bentley Systems, 2018a).

For problems where rainfall infiltration or suction loss is central, PLAXIS provides the *Fully coupled flow–deformation analysis*. This calculation type solves the full Biot equations together with Richards' equation for unsaturated flow, where the degree of saturation and permeability are functions of matric suction. The simultaneous solution ensures that changes in pore pressure and soil deformation are computed in a strongly coupled manner at each time step. This is particularly suited to rainfall-induced slope failures, where pore-pressure build-up in the vadose zone leads to progressive loss of shear strength. The governing equations capture both the hydraulic boundary conditions (rainfall flux, evapotranspiration) and the mechanical response of the slope (Tsegaye, 2019)(Pradhan et al., 2022).

Stability assessment is often performed through the *Safety analysis*, which employs the shear strength reduction (SSR) technique. In this method, the soil strength parameters are gradually reduced as:

$$c' \longrightarrow \frac{c'}{\Sigma M_{sf}} \tag{4.3}$$

$$\tan\varphi' \longrightarrow \frac{\tan\varphi'}{\Sigma M_{sf}} \tag{4.4}$$

where c' is the effective cohesion, φ' the effective friction angle, and ΣMsf the strength reduction multiplier. The analysis continues until numerical non-convergence indicates global failure, and the factor of safety (FS) is defined as the critical value of ΣMsf. Displacements accumulated during SSR are numerical artefacts, but incremental shear strains and displacements in the last converged step map the failure surface; plotting ΣMsf versus a nodal displacement is a practical way to identify the critical step. This technique is widely used to quantify slope stability at different stages of loading or hydraulic conditions, also in excavations, embankments—either on initial states or after transient phases (Bentley Systems, 2017).

Dynamic problems require the *Dynamics calculation type*, where the equilibrium is written in the time domain as:

$$M\ddot{u} + C\dot{u} + Ku = f(t) \tag{4.4}$$

with M the mass matrix, C the damping matrix, K the stiffness matrix, u the displacement vector, and $f(t)$ the applied time-dependent load.

The *dynamic analysis (without consolidation)* is based a time-domain wave propagation and inertia effects (earthquakes, vibrations, impacts) with prescribed or frequency-dependent damping; pore pressures are usually kept constant (drained/undrained options via constitutive model). Rayleigh damping, expressed as a combination of mass- and stiffness-proportional components, is typically used to match target damping ratios at given frequencies. This option is essential for modelling seismic site response, machine foundations with vibrations, or dynamic soil–structure interaction where inertia dominates, and flow is secondary (Bentley Systems, 2019).

Extend dynamics to include generation/dissipation of pore pressures during shaking—needed for problems involving cyclic pore-pressure build-up, post-seismic settlements, or liquefaction analyses in more advanced constitutive models, that is the *dynamics with consolidation*. Its commonly used in the seismic analysis in saturated soils where hydromechanical coupling matters. Dynamic equilibrium plus fluid mass balance (Biot) solved in time, with appropriate damping and permeability scaling (Bentley Systems, 2019).

4.1.2. Soil-structure interaction

A key advantage of FEM is its ability to simulate Soil–Structure Interaction (SSI). For slopes with retaining systems, piles, or viaduct piers, FEM allows modelling the load transfer between soil and structural elements through interface elements and nonlinear constitutive laws (Brinkgreve et al., 2010). Studies have shown that SSI controls stabilising and destabilising mechanisms in slopes and must be considered in cases where foundations or structural loads affect slope kinematics (Ou, 2006)(Won et al., 2005).

Correctly modelling SSI requires a consistent representation of both the soil domain and the structural components, together with appropriate interface formulations to capture relative displacements and shear transfer.

The key requirements for FEM-based SSI analysis include:

- Soil constitutive model: the soil must be represented with a realistic stress–strain law. For practical slope analyses, the Mohr–Coulomb model is widely used for its simplicity, but Hardening Soil (HS) or HSsmall provide more accurate representation of stress-dependent stiffness (Brinkgreve et al., 2010). The choice of model determines how soil deformations, pore pressures, and load transfer evolve during slope failure.
- Structural representation: the structural elements can be modelled as:
  - Plates or beams: for thin elements such as retaining walls, piles, or slabs, with bending and axial stiffness defined by section properties (E, I, A).
  - Volume elements: for massive piers or foundations, where 3D models may be more appropriate.
  - Embedded pile elements: a PLAXIS feature that simulates piles as beam elements coupled with surrounding soil springs, calibrated via p–y, t–z, and q–z curves (Fellenius, 2018).
- Interface elements: to correctly simulate frictional or cohesive interaction, interface elements are introduced along the contact between soil and structural surfaces. In PLAXIS, these are governed by a reduction factor (R_{inter}), which scales the shear strength of the soil along the interface to account for roughness and potential slip. Calibrating R_{inter} is crucial, as it controls load transfer and mobilisation of shear forces at the soil–structure boundary (Potts & Zdravkovi’c, 1999).
- Hydro-mechanical coupling: in rainfall-induced failures, infiltration alters pore pressures around structural foundations. Coupled flow–deformation analyses must therefore be performed to capture reduction in effective stresses and softening of soils supporting piles or walls. This requires defining boundary conditions for rainfall

infiltration and permeability contrasts at soil–structure contacts (Ng & Shi, 1998).

- Load conditions: external loads applied on structures (traffic loads, self-weight of piers, surcharge on retaining walls) must be considered. These loads interact with the soil domain, redistributing stresses and affecting stability. In back-analyses, such loads must reflect the real conditions at the time of failure.

Accurate SSI analysis requires detailed geotechnical and structural parameters, reliable laboratory and in situ tests for soil calibration, and knowledge of foundation geometry and stiffness. Numerical convergence can be problematic in post-failure stages, especially when large relative displacements occur at interfaces.

4.1.3. Static and dynamic analysis

While dynamic FEM analyses are necessary in seismic-prone regions, rainfall-induced failures are governed primarily by static hydro-mechanical processes. Fully coupled flow–deformation analyses in PLAXIS 2D allow simulation of infiltration, suction loss, and pore-pressure build-up, providing insight into how rainfall duration and intensity influence stability (Khan, 2023). The software offers both effective stress and total stress formulations; however, it is widely recommended to rely on effective stress analyses for rainfall-induced problems, as total-stress (c_u) analyses may not capture time-dependent strength changes (Bentley Systems, 2023).

4.1.4. Post-failure modelling

Classical small-strain FEM is limited to identifying the onset of failure, usually detected by non-convergence or via the strength reduction method. To study run-out behaviour and large deformations, advanced methods such as large-deformation FEM (LDFE) or the Material Point Method (MPM) have been developed Wu et al. (2024). These methods reproduce flow-like movements, strain softening, and post-failure mobility in sensitive clays or debris flows, complementing traditional FEM pre-failure analyses.

4.2. Case Study: Himera I

4.2.1. Premise

The region of Caltavuturo (PA) is situated in the southern part of the Madonie mountain range and features a complex geological setting. This complexity arises from the presence of various geological formations and a geological-structural framework shaped by multiple tectonic events, including compressive, transpressive, and relaxing phases. The area's hilly terrain predominantly consists of clayey (pseudo-coherent) soils, which support a detrital hydrographic network that channels water into the Northern Imera river.

In 2005, a persistent landslide front on this slope rendered provincial road 24, which connected Scillato to Caltavuturo and passed directly beneath the “Himera I” viaduct of the A19 motorway, inoperable. A significant reactivation of this landslide occurred on April 10, 2015, at around 4:20 PM. This reactivation was triggered by heavy rainfall that affected the Scillato area (PA) and the upper side of the A19 Palermo-Catania motorway, specifically at km 57+500, just 500 meters from the Scillato junction.

The landslide caused rotation at the base of one of the piers of the “Himera I” viaduct toward Catania, impacting at least two additional piers. Figure 14 illustrate the conditions of both viaducts and the state of the roadway toward Catania immediately following the landslide event. The rotation of certain piers resulted in the spans of the viaduct toward Catania colliding with the viaduct toward Palermo, which caused additional stress on it.

Figure 14. *Flanking of the carriageways and state of the carriageway towards Catania of the "Himera" viaduct I" following the landslide of April 2015 (ANAS, 2016).*

In response to this incident, ANAS (Azienda Nazionale Autonoma delle Strade S.p.a.), the managing body of the A19 motorway, ordered the closure of the motorway in both directions between the Tremonzelli and Scillato exits. This closure had severe socioeconomic impacts on the entire region served by the motorway. Initially, there were considerations to demolish both viaducts; however, to mitigate the disruption, the actual course of action taken involved demolishing only the damaged section of the viaduct toward Catania while monitoring the viaduct toward Palermo to assess its potential reopening for traffic.

The significant landslide movement, triggered in the upper left bank of the F. Imera, rapidly advanced to the valley floor, causing extensive damage to several piers of the viaduct on the Catania side, resulting in the destruction of both the piles and scaffolding. Consequently, the damaged section of the viaduct was demolished, with plans for a new structure to be constructed in its place.

4.2.2. Data acquisition and site identification

The study area lies on the right (DX idraulica) side of the Imera Settentrionale valley, immediately upslope of the A19 "Palermo–Catania" viaduct between Piers 16 and 22 (Figure 15). ANAS' executive geology report frames the objective as reconstructing the Catania-bound carriageway after the 10-April-2015 landslide, while maintaining continuous geomorphological–geotechnical monitoring of the slope adjacent to the bridge works.

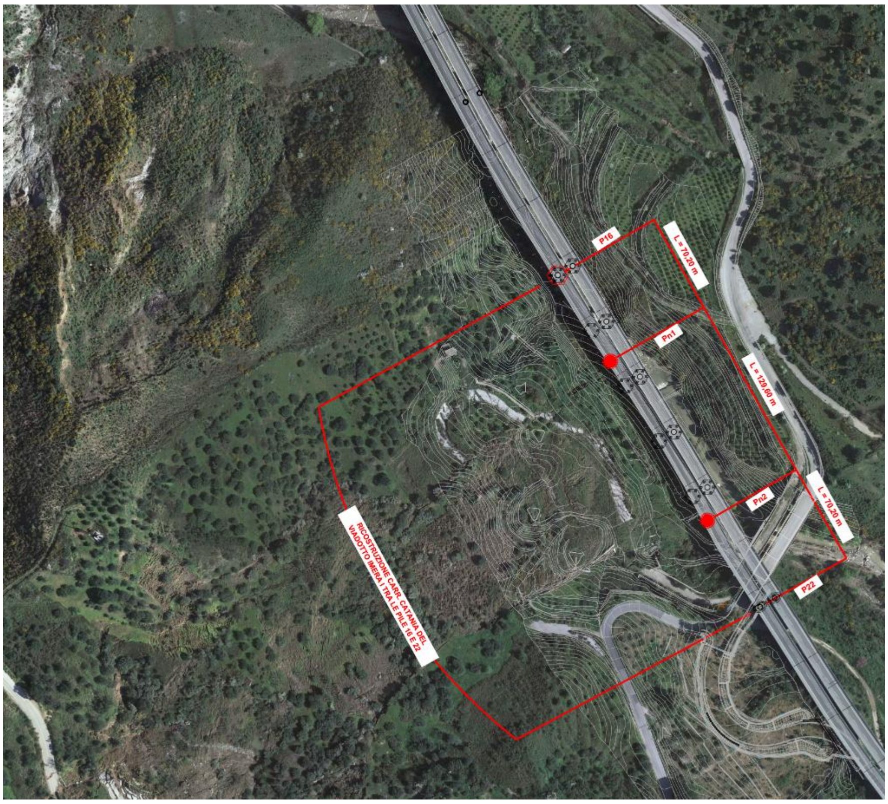

Figure 15. *Project plan on orthophoto - Reconstruction of the Catania direction carriageway of the Imera I viaduct between piers No. 16 and 22 (ANAS, 2016).*

The baseline ground model was assembled from 2015–2016 geognostic campaigns (core drilling, SPT, undisturbed sampling) and integrated with historical investigations performed for the 2015 demolition works. In 2016 alone, 17 boreholes were drilled (8 cored to ~20–40 m; 9 cross-hole to ~20–35 m), with in-situ SPTs and lab testing on undisturbed samples; the shallow sequence consistently showed 3–4 m of alluvium overlying Numidian Flysch.

Automated and manual monitoring included inclinometers and multi-level piezometers along four alignments on the active landslide and adjacent works (Bretella, SP-24, and the viaduct corridor), as mapped in the project's monitoring plan.

Within this compilation the following relevant information has been obtained:

- Geotechnical Report and attachments (Executive Project)

Drilling number: 8 (2015) and 25 (2016)

Made by: ANAS

Date: June 2016

– Geological-technical notes

Drilling number: 1 (near Pile 16)

Made by: HYMERA LAVORI S.c.a.r.l.

Date: January 2019

– Detailed geological map with geomorphology elements

Made by: ANAS

Date: 2016

– Geological sections along the landslide slope

Made by: ANAS

Date: 2016

– Piezometer readings

Made by: ANAS

Date: 2016

The characterization of the Himera I landslide required integrating multiple data sources at different spatial and temporal scales. Historical archives and previous reports confirmed the presence of ancient dormant landslide deposits, which had been partially stabilised but remained susceptible to reactivation under critical rainfall conditions. This combination of remote sensing, field data, and monitoring provided a comprehensive basis for setting up numerical models.

4.2.3. Site characterization

Topography

Topographic surveys were carried out using aerial photogrammetry, terrestrial laser scanning, and drone-based reconnaissance, which allowed the delineation of the main scarp, displaced mass, and secondary scarps. These methods were essential to quantify surface displacements and to identify morphological indicators of slope reactivation (Casagli et al., 2017).

The area under intervention lies within the Sicilian mountain system (Figure 16) of the Madonie, which represents a segment of the Sicilian chain formed by the stacking of a succession of tectonic units emplaced after the Early Miocene, resulting from the deformation of original paleogeographic domains identified during the Mesozoic extension phases. The landslide body occupies a west–east trending hillslope that drains toward the Imera river.

The geological, stratigraphic, and structural characteristics are those found in both the extreme western sector (Monti di Palermo and Trapani) and the eastern and southern areas (Nebrodi and Fossa di Caltanissetta).
The outcropping areas of structurally complex formations with a strong pelitic component (varicolored clays associated with the Sicilide Complex; Numidian Flysch, etc.) are generally characterized by gently sloping sides, with a high density of landslides of various types and states of activity (from active to inactive, including ancient and paleo landslides), with a predominance of rotational slides, slumps, and flows, as well as complex phenomena like slide-flow.

The affected slope extends approximately 700 m downslope from the Madonie range, with an average slope inclination between 20° and 25°. The slope surface is characterised by a sequence of rotational scarps at the crown and translational movements along mid-slope benches. The A19 motorway viaduct intersected the landslide body, with several piers founded directly within the moving mass. High-resolution digital elevation models (DEMs) showed clear deformation of the viaduct alignment, corroborating the link between slope instability and structural distress.

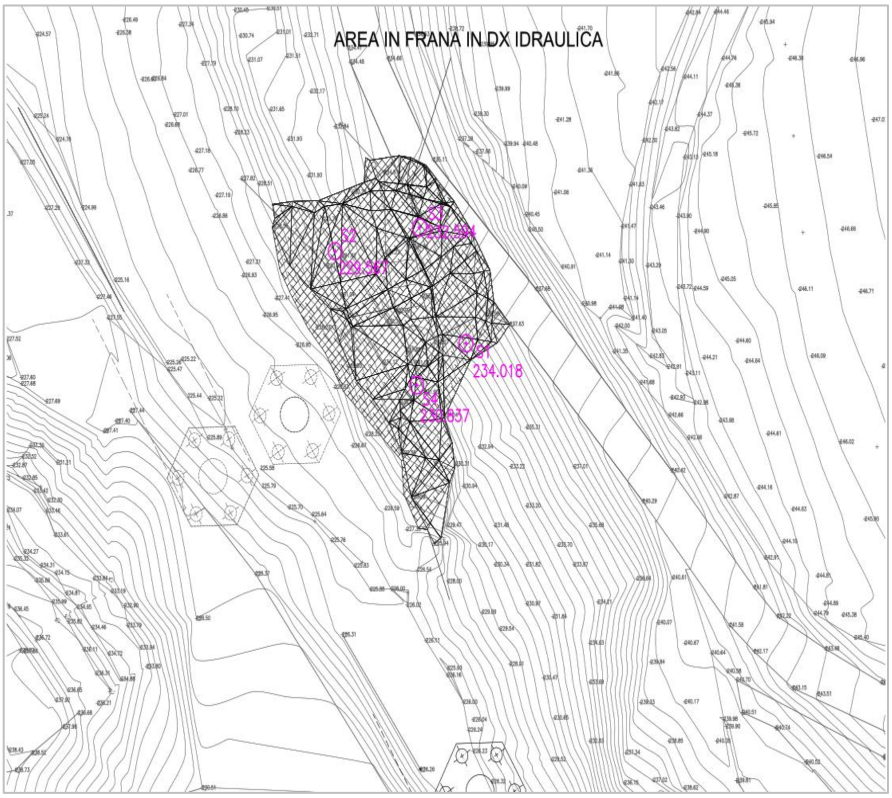

Figure 16. *Topography of the study area DX idraulica (ANAS, 2016).*

Piezometer reading

Hydrological monitoring revealed a strong correlation between rainfall intensity and pore-pressure rise. During the weeks preceding the April 2015 failure, cumulative rainfall exceeded seasonal averages, resulting in groundwater levels rising by more than 3 m within clay-rich horizons. Piezometer readings confirmed the formation of perched water tables above low-permeability strata, reducing effective stress and mobilising shear along pre-existing slip surfaces. This response is consistent with findings from other rainfall-induced failures in clay-rich formations in Italy (Brunetti et al., 2010)(Boniello et al., 2010).

For this project, 18 piezometers were placed throughout the study area to monitor and control the piezometric level as shown in Table 5 and Figure 17.

Table 5. *Information on the piezometers placed in the study area.*

Data Acquisition Unit [UAD]	Instrument code	Installation date	Depth [m]
UAD - SC2	SC2-PZ1	27/09/2016	25
	SC2-PZ2	27/09/2016	14.5
UAD - SC3	SC3-PZ1	28/09/2016	24.5
	SC3-PZ2	28/09/2016	14
UAD - SD4bis	SD4bis-PZ1	27/09/2016	13
	SD4bis-PZ2	27/09/2016	23.5
UAD - SD5	SD5-PZ1	28/09/2016	26
	SD5-PZ2	28/09/2016	20.5
UAD - SD6	SD6-PZ2	28/09/2016	14.5
	SD6-PZ3	28/09/2016	20.8
UAD - SD7	SD7-PZ1	28/09/2016	24.5
	SD7-PZ2	28/09/2016	8.5
UAD - SE2	SE2-PZ1	29/09/2016	23.5
	SE2-PZ2	29/09/2016	12.5
UAD - SE3	SE3-PZ1	29/09/2016	24.5
	SE3-PZ2	29/09/2016	13.5
UAD - SE5	SE5-PZ1	28/09/2016	23.5
	SE5-PZ2	28/09/2016	13.5

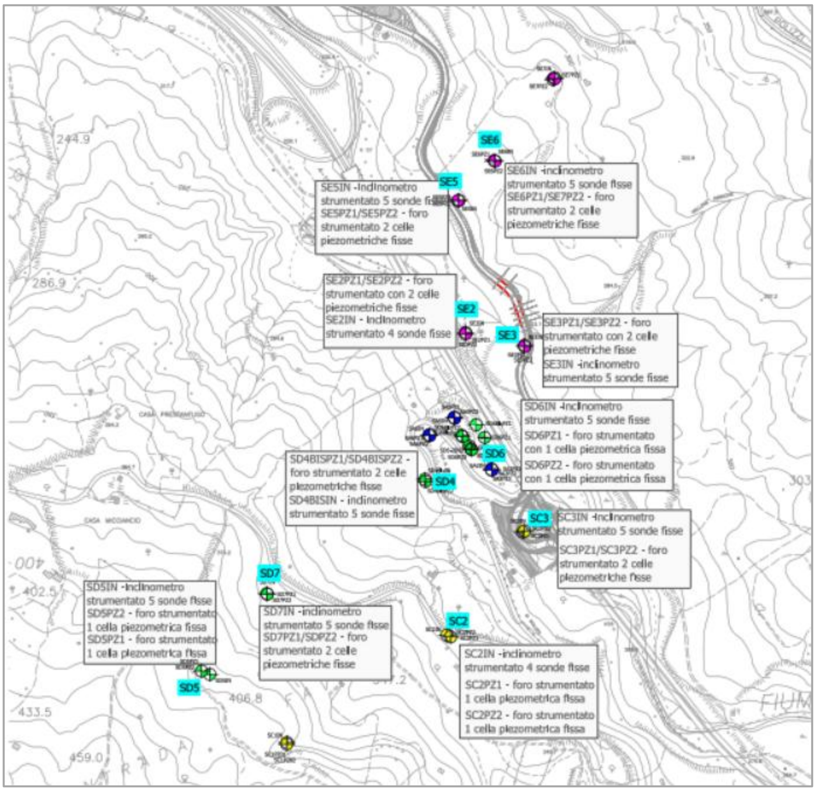

Figure 17. *Location of the piezometers placed in the study zone (ANAS, 2016).*

In order to better understand the dynamics of the event, it is particularly relevant to establish a connection between the evolution of the landslide process and the rainfall regime in the area during that period, making reference to the data recorded at the two nearest pluviometric stations, Scillato and Caltavuturo. It should be noted that between January and April 2015, the cumulative precipitation recorded at both stations was considerably higher than the average seasonal rainfall for the same period, indicating an exceptional hydrological condition that contributed to the predisposing factors of the slope failure, suitable for extracting seasonal oscillations and defining hydrogeologic boundary conditions for the FEM model.

The review of the Technical–Geological Report prepared by geologist Basile of the Regional Department of Civil Protection, drafted in the aftermath of the April 10 landslide, reconstructs the rainfall conditions that preceded the event. By analysing the charts (Figure 18), the report highlights several episodes of significant precipitation. Among them, the period from February 21 to 28 was especially remarkable, with cumulative rainfall of approximately 130 mm at the Caltavuturo Station and 140 mm at the Scillato Station. This was immediately followed by another rainfall event between March 5 and 8, with cumulative amounts of about 70 mm and 110 mm, respectively. The final notable precipitation episode occurred between March 27 and 29, when 60 mm were recorded at Caltavuturo and 65 mm at Scillato.

These consecutive rainfall episodes coincided with the initial signs of instability along Provincial Road SP 24. The earliest indications were reported on March 3, 2015, and the situation worsened considerably between March 23 (source: Municipality of Caltavuturo, prot. n. 3222 of 23.03.2015) and April 4 (source: www.madoniepress.it, 04.04.2015), by which time the landslide had already destroyed the provincial road in that sector. Although no rainfall was recorded on April 10, the date of the paroxysmal collapse, Basile pointed out that by then the cumulative rainfall totals had reached unprecedented values. Specifically, Caltavuturo Station registered 574 mm compared with the seasonal average of 330 mm for January–April, while Scillato Station measured 603 mm compared with its average of 354 mm. This represents an increase of about 80–90% above the seasonal mean, a condition that significantly contributed to the progressive saturation of the slope and the subsequent failure.

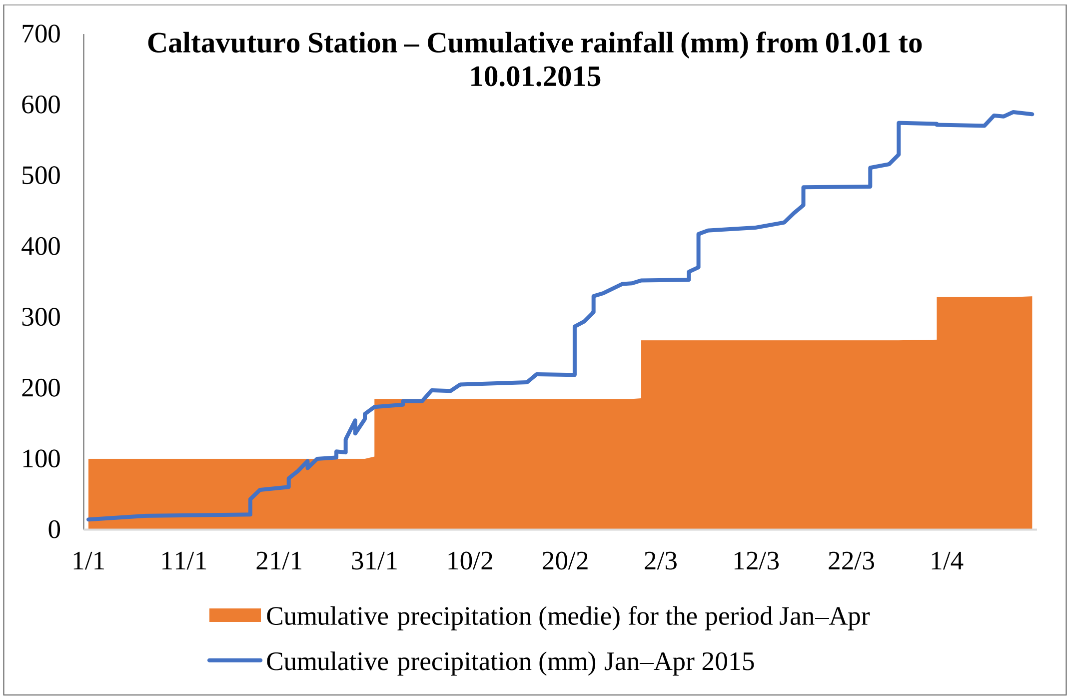

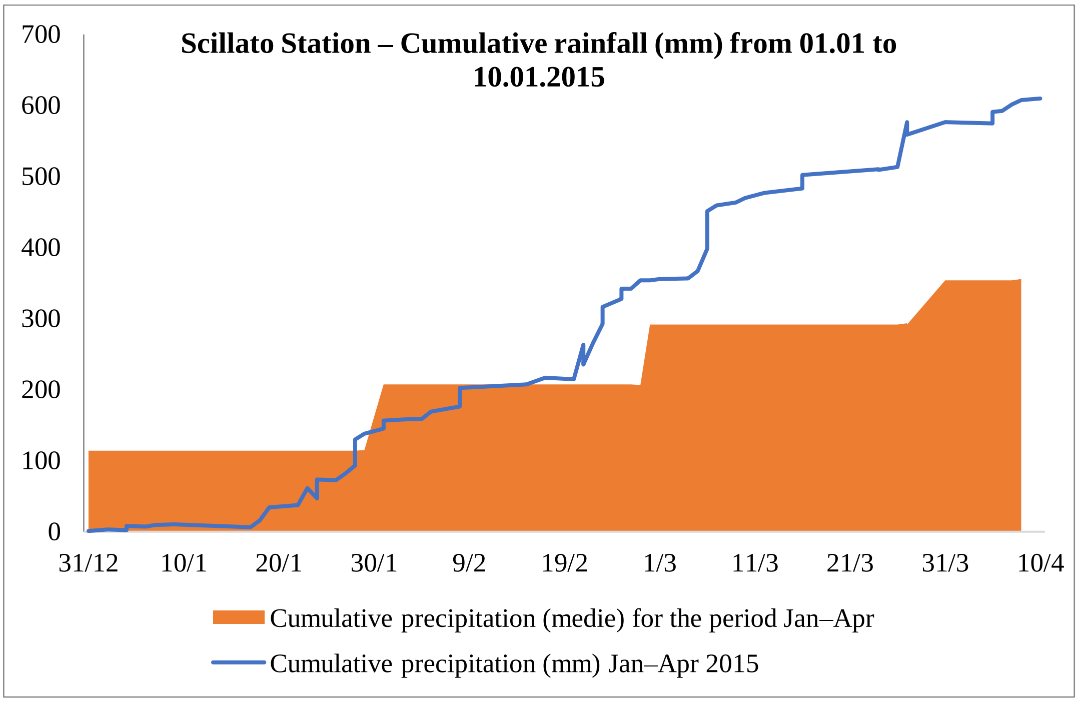

Figure 18. *Rainfall charts for the Caltavuturo and Scillato stations from January to April 2015.*

The project documents compile both one-off depths to water (Sept-2016) and automated time series (2016–2019). Example zero-readings show groundwater at ~8.5–24.5 m below ground across SE/SD stations (e.g., SD6-PZ2 = 14.5 m; SD6-PZ3 = 20.8 m; SD7-PZ1 = 24.5 m; SD7-PZ2 = 8.5 m; SE3-PZ1 = 24.5 m; SE3-PZ2 = 13.5 m; SE5-PZ1 = 23.5 m; SE5-PZ2 = 13.5 m; all 28–29/09/2016).

Past load conditions (Geology)

The geomorphological layout of the Madonie group is extremely varied and results from the shaping caused by different morphogenetic processes on the various exposed lithologies, as well as the interaction of these processes with the tectonic and neotectonic vicissitudes undergone by the area, together with the climatic changes that occurred during the Quaternary period, which have led to the alternation of morphoclimatic systems with changing characteristics; in this context, karst areas are particularly important.

From a geomorphological perspective, the Madonie range presents varying contexts: of rugged limestone nature in the centre, softer in the peripheral areas of clayey-sandy origin; as a result, it exhibits imprecise profiles, poorly defined slopes, irregular altimetric distribution, and includes several main cores deeply marked by valleys and depressions that intersect it in all directions, with numerous watercourses, predominantly of a torrential nature, flowing at their base (Figure 19).

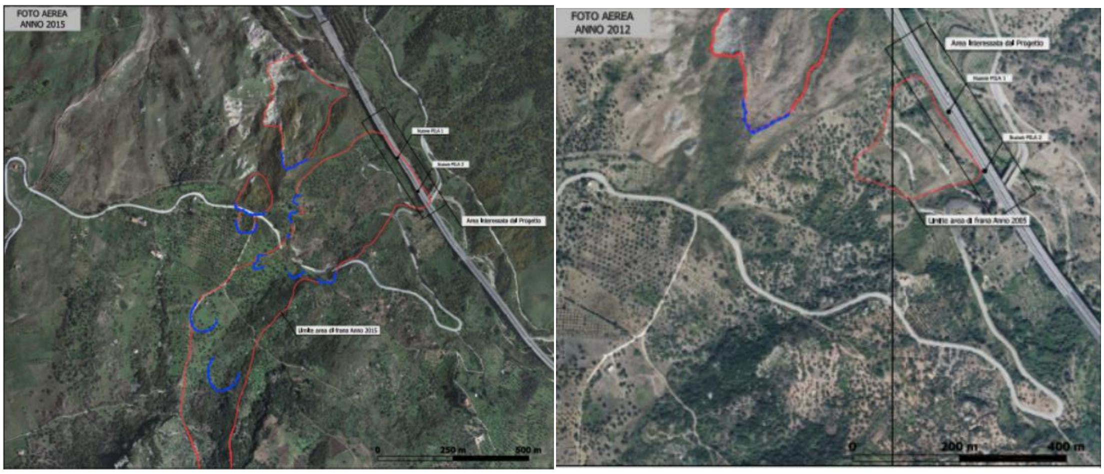

Figure 19. *Comparative photos of the before and after of the landslide caused by the April 2015 rain: left side in 2015 after the event and right side in 2012 before the event. (ANAS, 2016).*

In summary, from a formational point of view, the area under examination is characterized by the outcrop of the following units, from the oldest to the most recent (Figure 20):

- Crisanti Formation (CRI), represented by a thick succession of thin-bedded radiolarites alternating with siliceous clays and interbedded clastic-carbonate bodies; the formation is divided into four members, of which Member 4, known as the "Rudist Breccia Member," outcrops in the area. This member is characterized by grey calcirudites and calcarenites with rudists and orbitolines in coarse beds and centimeter-thick layers of grey-green calcarenites and marls that thin upwards.
- Caltavuturo Formation (CAL), composed of calcilutites and marly limestones alternating with clayey marls, sometimes flaky, in wine-red, pinkish, and greyish colors, in centimeter-thick layers with parallel laminations and nodules or bands of black or red chert. Thickness ranges from 50 to 150 m.
- Numidian Flysch (Portella Colla Member – FYN2): brown pelites, sometimes manganiferous, with plane-parallel lamination, interbedded with graded quartzose sandstones. Thickness ranges from 100 to 300 m. It crops out to the north and east of the site, in tectonic window conditions, or in thrust sheets underlying the Sicilide units.
- Lower Varicolored Clays (AVF), flaky-structured clays and varicolored marls, often chaotic, with jasper and quartz-mica sandstones, greenish calcilutites, and levels of biocalcarenites containing macroforaminifera and mollusk fragments. Thickness varies between 70 and 200 m. The lower boundary is tectonic in nature over the terms of the Numidian Flysch and Polizzi Formation.
- Alluvial deposits of the northern Imera river (b1): valley-bottom alluvium with grain size ranging from sandy-gravelly to silty-clayey, predominantly in the marginal areas relative to the riverbed.

- Landslide deposits (a1): with chaotic structure and predominant pelitic matrix, containing heterogeneous lithoid elements, within landslide bodies mainly resulting from flow, exhibiting various stages of activity.

Regarding hydrogeological aspects, the various geological units can be grouped into two complexes:

1. Limestone-dolomitic complex
2. Impermeable complex, generally composed of clays, claystones, and marls.

Groundwater circulation within the limestone-dolomitic complex occurs exclusively through fracture networks and karstic conduits. Additionally, it is influenced by the lithostratigraphic characteristics of the sequences and by the geometries of thrust fronts, which act as permeability boundaries and thresholds.

The relative relationships between clayey covers and carbonate sequences define the geometry of the hydro structures. When the limestone-dolomitic and calcareous-siliceous-marly structure tectonically overlies the clayey sequences of the Numidian Flysch, multiple water emergence fronts are formed, where high-yield springs are found. Furthermore, when the impermeable Numidian terrigenous cover follows the calcareous complex in stratigraphic succession, the aquifer becomes confined and remains in contact with the unconfined aquifer present in the recharge areas.
Regarding the geomorphological features characterizing the intervention area, it predominantly affects clayey lithotypes with pseudo-coherent behaviour, primarily composed of clays from the "Numidian Flysch" and, to a lesser extent, the "Varicolored Clays," as well as gravity-induced landforms with varying degrees of activity.

Therefore, it can be stated that the area predominantly involves clayey lithotypes, which, under the influence of exogenous agents, are easily shaped and, due to the existing slopes and observable hydrogeological complexity, are highly susceptible to gravitational movements.

The geomorphological evolution of these slopes is thus largely dependent on the rheological characteristics of the affected soils and on soil erosion processes linked to rainfall. Surface runoff exerts an erosive action on the weathered mantle of the geological formations in situ (Numidian Flysch and Varicolored Clays), while groundwater infiltrates the permeable horizons of these formations, altering the neutral pressure regime and facilitating the formation of preferential slip surfaces.

Due to the combined effects of exogenous agents, particularly of intense meteorological precipitation and water discharges from upstream areas, complete saturation of the weathered mantle occurs, resulting in significant gravitational movements relative to the thickness and areal extent of the weathered layer and the topographic surface gradient.

The landslide event in April 2015 notably exhibits these characteristics: the landslide body extends approximately 700 m from the detachment niche at the top to the toe of the landslide, which affected the piles of the highway viaduct. The landslide has an average width of 170 m in the upper areas and 210 m in the accumulation zones, with detachment niche heights averaging close to 4 m.

The first detachment niche formed as a result of a landslide in March 2015 has an average height of about 4-5 m and is located approximately 240 m upstream of the former provincial road interrupted by the landslide itself. The second detachment niche, also approximately 4 m in height, is situated at an elevation close to 350 m above sea level, still upstream of the provincial road.

Continuing downstream, in the area beneath the provincial road, transverse bulges are found, attributable to accumulation zones of overlapping gravitational events, along with radial cracks which generally arise due to the differing behaviour of materials with varying elasticity involved in the movement. Following this, at distances ranging from 250 m to 300 m from the highway axis, a series of secondary detachment niches appear, with heights between 1 m and 3 m, partially affecting the accumulation zones downstream, which are located at elevations between 260 m and 290 m above sea level.

Finally, the entire toe of the landslide, within a band ranging from 200 to 230 m above sea level and the highway axis, is affected by a dense network of longitudinal cracks formed due to the varying speed of mobilization of the mobilized material, as well as transverse cracks essentially created by the compression and subsequent expansion of the accumulated material.

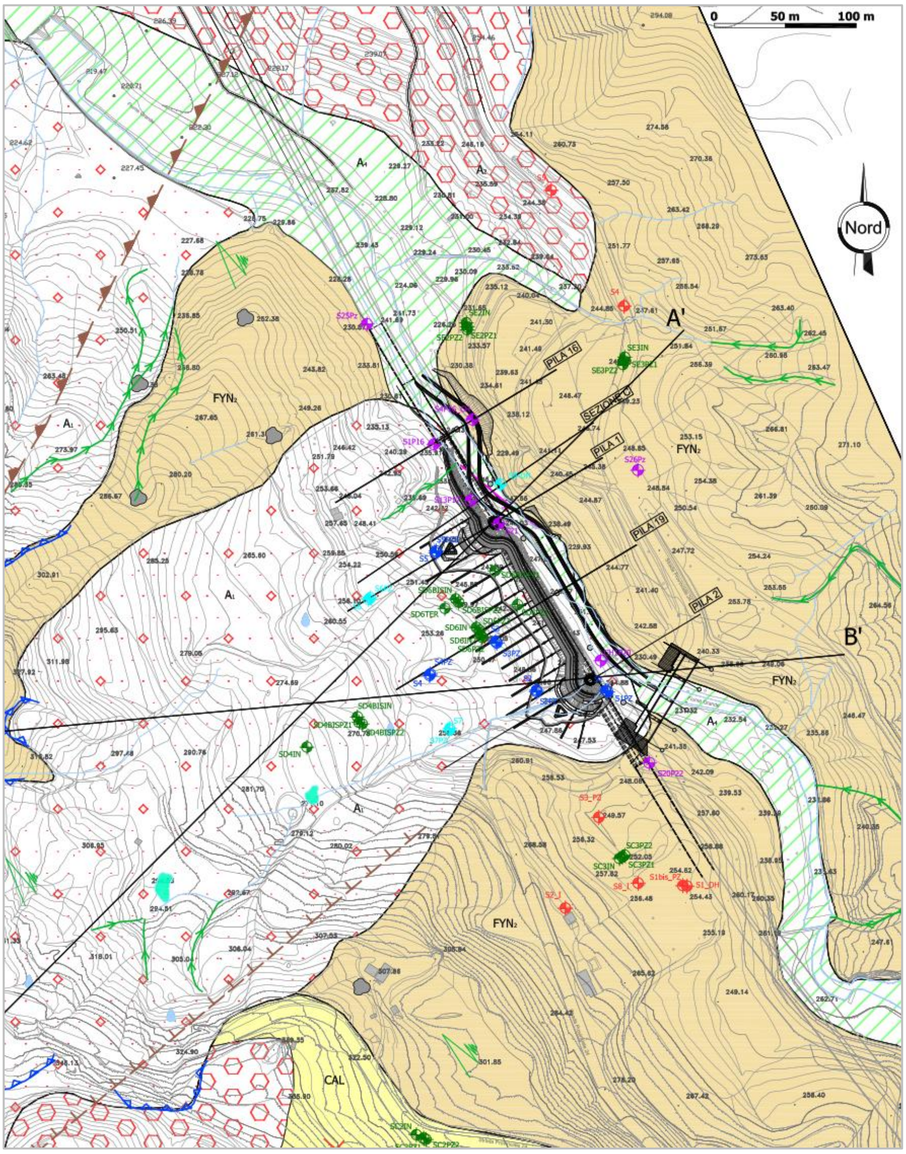

Figure 20. *Geological map of the study zone with the geomorphological elements (ANAS, 2016).*

So, the site geology is dominated by the Numidian Flysch formation, comprising alternating sandstones, marls, and clays. The clayey members, with low permeability and plastic behaviour when saturated, acted as the principal failure surfaces. The landslide reactivation occurred within ancient landslide deposits, meaning that the mass had already undergone significant displacement in the past, with residual shear strength governing stability. This geological inheritance explains the relatively low mobilised strength parameters observed during back-analysis.

4.2.4. Geotechnical characterization

Geological and geotechnical investigations included boreholes, trial pits, and laboratory testing on representative samples of flysch soils and weathered clays. These data established stratigraphic layering and mechanical properties (e.g., unit weight, shear strength, permeability).

As illustrated in the geological framework, the area affected by the route in question is characterized by the presence of a substrate of compact flyschoid materials, which present upwards a level of homogeneous thickness of the same altered material. At the roof of such materials the destructured material that constitutes the landslide deposit is present. At the foot of the alluvial deposits of the Imera river are located on the slope. Based on the findings from the investigations and considering the intervention in question, the following soil types are identified for design purposes (from the most superficial to the deepest) (Figure 21):

1. Alluvial deposits (SG-type soils), at the foot of the slope, with a thickness of approximately 5.0 m;
2. Landslide deposit (CF-type soils), consisting of flysch-origin material in destructured, altered, and chaotic conditions, with a variable thickness from about 9 to 20 m in the area of interest;
3. Altered flysch (Ar1-type soils), consisting of the alteration of the substrate, with a thickness of about 5 m;
4. Flysch in argillaceous facies (Ar-type soils) or arenaceous facies (Ar-Num-type soils) as the base formation, occasionally of lithoid nature (Ar-lit-type soils).

On 06/01/2019 occurred a landslide event, so a geognostic survey was carried out relating to the "Reconstruction Project of the carriageway towards Catania of the Imera 1 Viaduct between Pile 11 and 22 Motorway A19 Palermo – Catania" called Landslide area on the hydraulic (Area in frana in dx idraulica), that name was imposed by reason that this landslide be affecting the right bank of the Imera River at Pier 16.

A deviation of the riverbed was planned, involving the creation of a meander by retreating the right bank approximately 15 meters and reshaping the slope profile to around 45°. A continuous core geognostic borehole located near the crest of the landslide, in accordance with accessibility and safety considerations for personnel and equipment: the borehole was drilled, however, prior to the assignment given to the undersigned, behind the actual landslide area due to obvious accessibility and safety concerns.

The lithology identified through the geognostic borehole, corresponding on a medium-large scale to the Numidian Flysch, can be summarized as follows (elevations are relative to the borehole opening):

- 0.00-12.50m – Predominantly silty-clayey lithotype, with a weak sandy fraction and brecciated sandstone inclusions. It appears to have a chaotic structure, moderately consistent, but highly altered. In general, it resembles a superficial detrital layer, but specifically, two very saturated, softened levels are observed at elevations of approximately 3.00-4.00m and 7.50-8.50m. The physical-mechanical parameters measured on the collected samples indicate extremely low shear strengths in terms of effective stresses.
- 12.50-15.00m – Lithotype resembling a siliceous rock mass, intensely fractured. It could correspond to the rock mass currently exposed at the landslide's base within the riverbed (see the area marked with a red arrow in the previous photos), though it may also represent part of an ancient paleo-channel of the Imera River.
- 15.00-20.00m – Decimetric alternation of dark gray marly clays and black quartz-siltstones with a foliated structure. The foliation

surfaces are subconchoidal in shape, often with a translucent surface. The lithotype appears very consistent in the terrigenous portion; the lithoid portion is fractured, but the individual elements are very hard and thus extremely brittle.

According to data provided by the client, the water table was encountered at -12.50m from the borehole opening during drilling.
The lithostratigraphic sequence identified through the borehole consists of an approximately 12.50m thick surface detrital layer with at least two very saturated levels at about -3.00m and -7.50m, resting on a rock bed approximately 2.50m thick. Given the texture and depth in the borehole, it may represent the original paleo-channel of the Imera River.

The entire sequence rests on an alternation of consistent clays and quartz-siltstones: considering the textural and structural characteristics, this portion could represent the in-situ lithotype, and thus, in terms of the typical physical-mechanical characteristics of flysch formations, the geotechnical bedrock.

Based on field surveys and the lithology identified through the investigations, it is presumed that the slope movement can be categorized as a rotational-translational landslide.

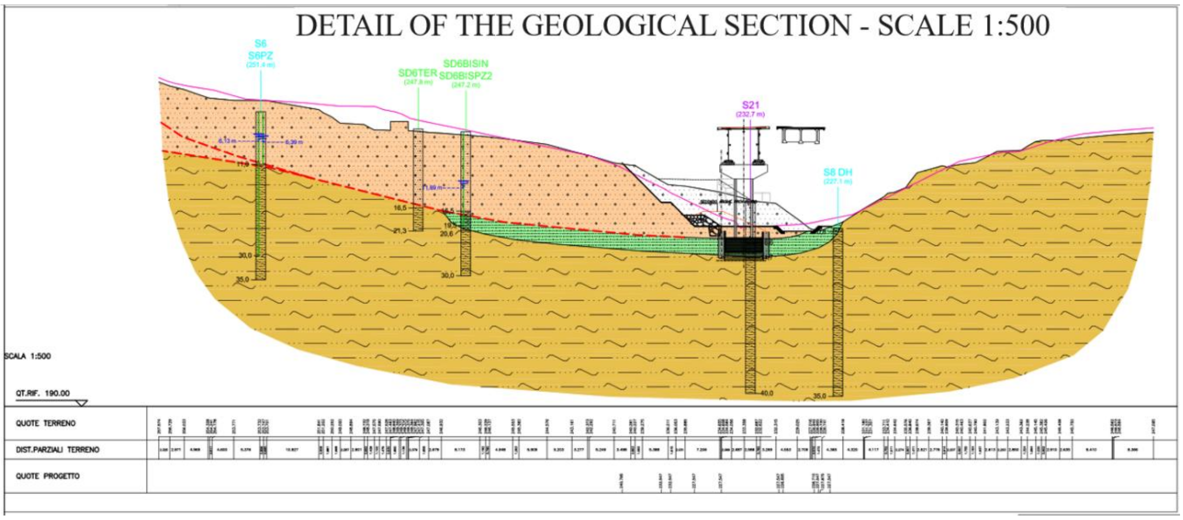

Figure 21. *Lithological identification of the strata found according to surveys and geology of the site (ANAS, 2016).*

The general geotechnical parameters of the Himera I slope were derived from laboratory triaxial tests, oedometer tests, and in situ borehole data. Key properties included:

- Unit weight (γ): 18–20 kN/m³ (saturated).
- Effective cohesion (c'): 5–10 kPa.
- Effective friction angle (φ'): 18–22°.
- Elastic modulus (E): 5–15 MPa, depending on depth and degree of saturation.
- Permeability (k): between 1×10^{-7} and 1×10^{-8} m/s in clayey layers.
- Poisson's ratio (ν): typically 0.3–0.35.

These values are consistent with weak, saturated clays in Mediterranean flysch formations, where rainfall infiltration rapidly leads to pore-pressure build-up and reduction of shear strength. Notably, the low cohesion and moderate friction angle values align with residual strength conditions often observed in reactivated landslides (Lupini et al., 1981).

For modelling purposes, the Mohr–Coulomb constitutive model was adopted as it captures first-order strength properties and requires only five parameters (c', φ', E, γ). This choice allowed for a transparent calibration process against observed field behaviour, while acknowledging that more advanced constitutive models (e.g., Hardening Soil) may provide improved predictions of stiffness nonlinearity.

Based on the results of the tests performed and in accordance with the geological and lithostratigraphic evidence, the reference geotechnical parameters reported as characteristic values in Table 6 are identified for every layer.

Table 6. *Characteristic geotechnical parameters of the soils.*

Typical terrain	$\gamma\left[{}^{kN}/_{m^3}\right]$	$\varphi'[°]$	$c'[°]$	$E'[MPa]$
SG	21	28	0	50
CF	20	24-26	5-10	15
Ar	21	28	10	50

4.2.5. Slope stability analysis

FEM modelling in PLAXIS 2D was applied to reproduce the failure mechanism. The slope profile was discretized with a fine mesh. Mohr–Coulomb soil models were used for first-order analysis, consistent with the available soil strength parameters. Boundary conditions simulated rainfall infiltration through transient pore-pressure increases.
The strength reduction method (SRM) was adopted to compute factors of safety under varying rainfall intensities.

For rainfall-triggered landslides such as Himera I, the modelling workflow typically combines Fully coupled flow–deformation to capture the infiltration and pore-pressure rise during rainfall, followed by Safety analysis (SSR) to evaluate the evolving factor of safety at critical times. This sequence balances hydrological realism with stability assessment and has been successfully employed in recent case studies (Pradhan et al., 2022)(Bentley Systems, 2024).

Back analysis

Back-analysis was performed by iteratively adjusting soil strength parameters to match observed field behaviour to reproduce the observed failure mechanisms at the Himera I landslide. This approach allowed for the calibration of geotechnical parameters and the validation of the constitutive soil models adopted. These values are consistent with residual strength conditions typical of reactivated landslides in clayey flysch (Skempton, 1985). The analysis confirmed that rainfall-induced pore-pressure rise was the dominant trigger.

The modelling process followed a structured procedure, beginning with the definition of the soil domain and continuing through mesh generation, boundary conditions, groundwater flow conditions, and staged construction analyses.

The first step consisted of defining the geometry of the model. The stratigraphy of the case study was reproduced using soil polygons, which allowed the assignment of different material properties to each geological unit as show in the Table 6.

The soil behaviour was represented using the Mohr–Coulomb constitutive model, which provides a satisfactory approximation of shear strength and stiffness for stability analyses. Input parameters such as effective cohesion, friction angle, Young's modulus, and Poisson's ratio were derived from laboratory and in-situ tests, while hydraulic conductivity was included in both vertical and horizontal directions to allow the simulation of seepage. All soil units were modelled as drained materials, ensuring compatibility with the coupled flow–deformation calculations adopted later in the analysis.

Once the geometry and materials were assigned, the finite element mesh was generated. A medium element distribution was initially selected to balance accuracy and computational efficiency. Local mesh refinements were then applied in zones where strong stress or pore pressure gradients were expected, particularly around the slope toe, the interface with the groundwater table, and along potential slip surfaces. This approach improved the accuracy of the results while keeping the overall model size computationally manageable.

Standard boundary conditions were applied to confine the soil body. The base of the domain was fully fixed in both vertical and horizontal directions, while the vertical boundaries were restricted only in the horizontal direction, permitting settlement but preventing rigid body displacement. The upper boundary was left free to deform. These fixities are considered standard practice in geotechnical modelling and ensure that the simulated behaviour reflects real slope deformations rather than artefacts of the numerical domain.

The groundwater regime was then incorporated. An initial phreatic line was introduced, corresponding to site observations, and transient rainfall infiltration was applied as a boundary condition along the ground surface.

This was defined using a discharge function, $q(t)$, describing rainfall intensity as a function of time. The initial stress state of the soil was generated through the K_0 procedure, which provides a realistic geostatic equilibrium before additional loading is introduced.

The calculation itself was performed in several phases following a staged construction approach. In the first phase, the model was brought to equilibrium under self-weight and initial pore pressures, establishing a reference condition for the subsequent analyses. Rainfall infiltration was then introduced in Phase 2. To improve numerical stability, this phase was subdivided into three consecutive steps (2A, 2B, and 2C). Each sub-phase represented a portion of the total rainfall event, allowing pore pressures to increase gradually and avoiding abrupt hydraulic changes that could otherwise cause the calculation to stop prematurely. The rainfall intensity curves used in these phases were based on realistic temporal distributions and implemented as time-dependent surface fluxes, with the total time of rain that were occurring before the trigger event, that means 40 days of continues but low-intensity rainfall and were placed in each phase as Phase 2A for 5 days (0-5), Phase 2B for 10 days (5-15) and Phase 2C for 25 days (15-40), following the details of the $q(t)$ in Table 7.

Table 7. *Time-dependent rainfall infiltration function q(t) applied as boundary condition in the Phase 2.*

Time (day)	$\Delta \boldsymbol{q}$ ($\boldsymbol{m^3}/\boldsymbol{day}$)
0	0.000
0.2	0.002
1.0	0.004
2.0	0.006
5.0	0.008
10.0	0.010
20.0	0.010
30.0	0.010
40.0	0.010

A third calculation phase was added to simulate a triggering event, representing an additional episode of rainfall or groundwater rise. This was also modelled using fully coupled flow–deformation analysis with a time-dependent rainfall curve, which promoted further pore pressure increase and reduced effective stresses in the slope body, thus favouring failure initiation. With a total of 10 days with the following q(t) shows in the Table 8. Finally, a strength reduction analysis was performed using the phi–c reduction method to determine the global factor of safety. In this approach, shear strength parameters are progressively reduced until failure is reached, allowing the identification of the critical slip mechanism and the corresponding safety factor.

Table 8. *Time-dependent rainfall infiltration function q(t) applied as boundary condition in the Phase 3.*

Time (day)	$\Delta \boldsymbol{q}$ ($\boldsymbol{m^3}/\boldsymbol{day}$)
0	0.05
1.0	0.0056
10.0	0.0056

Throughout the analysis, particular attention was paid to numerical convergence. Infiltration phases were subdivided into smaller time intervals to ensure that the prescribed calculation time was reached. Local mesh refinements were verified to avoid poorly shaped elements, and drained behaviour was consistently assigned to all soils to prevent mismatches between phases. These adjustments eliminated common numerical issues such as singular stiffness matrices or premature failure of the solver, ensuring robust results.

The outputs of the model included pore pressure distributions during rainfall, hydraulic fields, displacement fields, and global stability curves, which highlighted the progressive development of failure mechanisms within the slope.

In the Figure 22 presents the groundwater head distribution where the calculated hydraulic head field shows maximum values of 39.5 m and minimum values of 18.5 m, highlighting a strong hydraulic gradient from the upper slope towards the valley bottom. This distribution confirms the presence of recharge in the head area and discharge at the toe, producing elevated pore pressures in deeper regions of the slope. These pore pressures reduce the effective stresses, thereby decreasing the available shear strength of the soil mass.

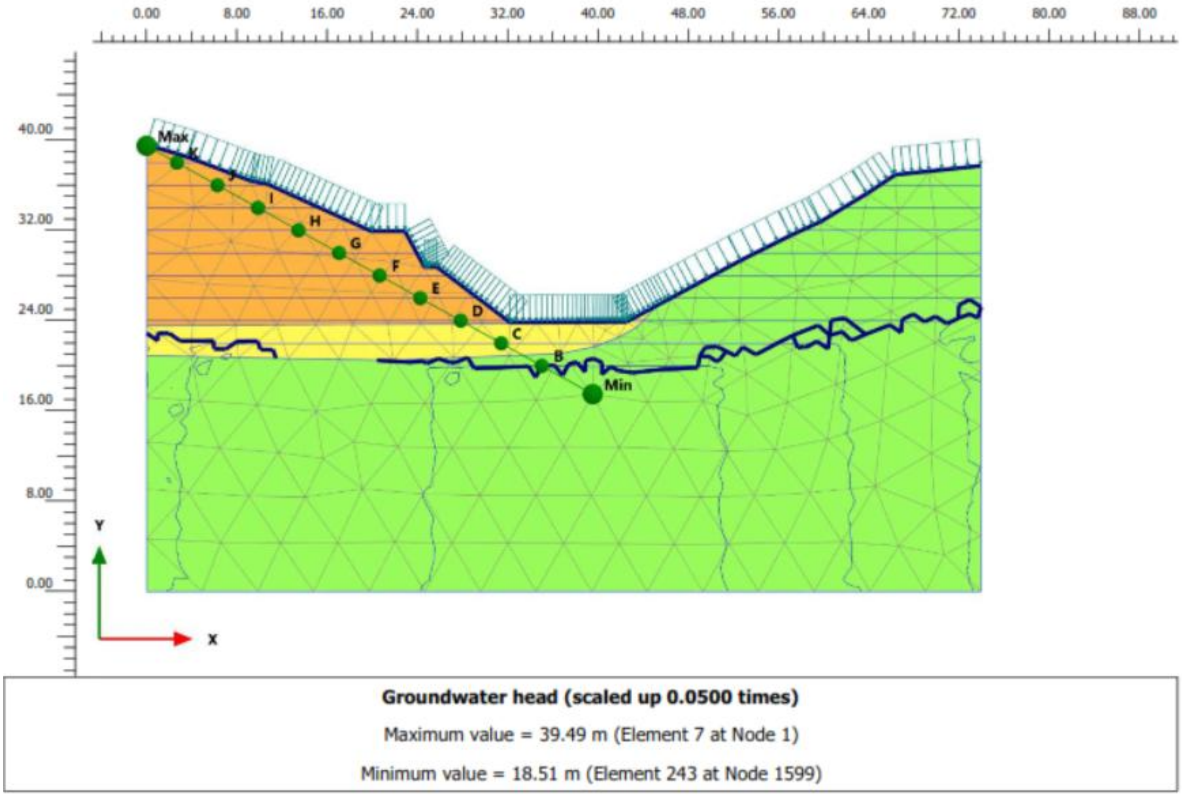

Figure 22. *Hydraulic head distribution obtained from the coupled flow–deformation analysis. Maximum head values are observed in the upper slope, with progressive dissipation towards the toe, consistent with rainfall infiltration and groundwater flow patterns.*

In the Figure 23 the computed field of active pore pressures (p_{active}) ranges from 0 kPa (at the phreatic surface) down to –241 kPa (representing suction in the unsaturated zone). This result clearly differentiates saturated areas, where pore pressure is positive or zero, from partially saturated zones, where negative pore pressures prevail. The presence of suction provides apparent cohesion and temporarily increases soil strength in shallow layers. However, under prolonged rainfall infiltration, suction progressively dissipates, which facilitates the initiation and propagation of slope failure.

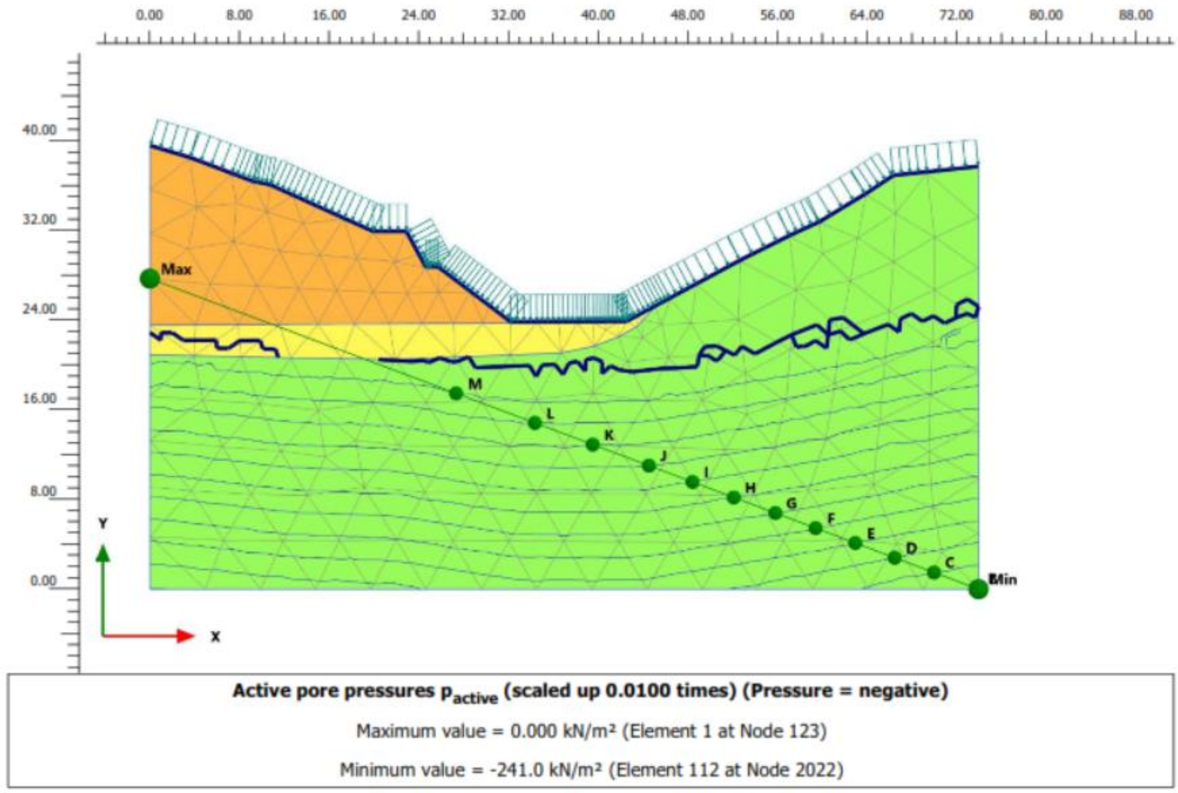

Figure 23. *Active pore pressure (p_{active}) field illustrating the hydro-mechanical response during infiltration.*

Meanwhile, the $|u|$ plot corresponding to the triggering phase reveals a wedge of large displacements developing on the left slope, propagating downslope toward the channel. The red/yellow zone delineates the concentration of the superficial sliding mechanism within the orange soil layer and extends into the yellow–green interface, representing the softer depositional unit (Figure 24). Indicating the development of a sliding mass moving downslope towards the valley. The mechanism corresponds to a combined rotational–translational landslide, initiating at the interface between superficial deposits and the underlying weaker layer. The inferred failure surface coincides with the zone where active pore pressures transition from negative to values approaching zero, consistent with the hydrogeological interpretation.

It is important to note that the annotation in the legend reports a maximum displacement value of 5106 m, which is clearly non-physical. This arises from the way PLAXIS scales and labels the legend in this output (the figure is displayed as "scaled up 0.500×10^{-3} times"). Therefore, this numerical value should be regarded as a plotting artifact. The relevant information is the shape and position of the displacement cluster, not the absolute magnitude reported in the legend.

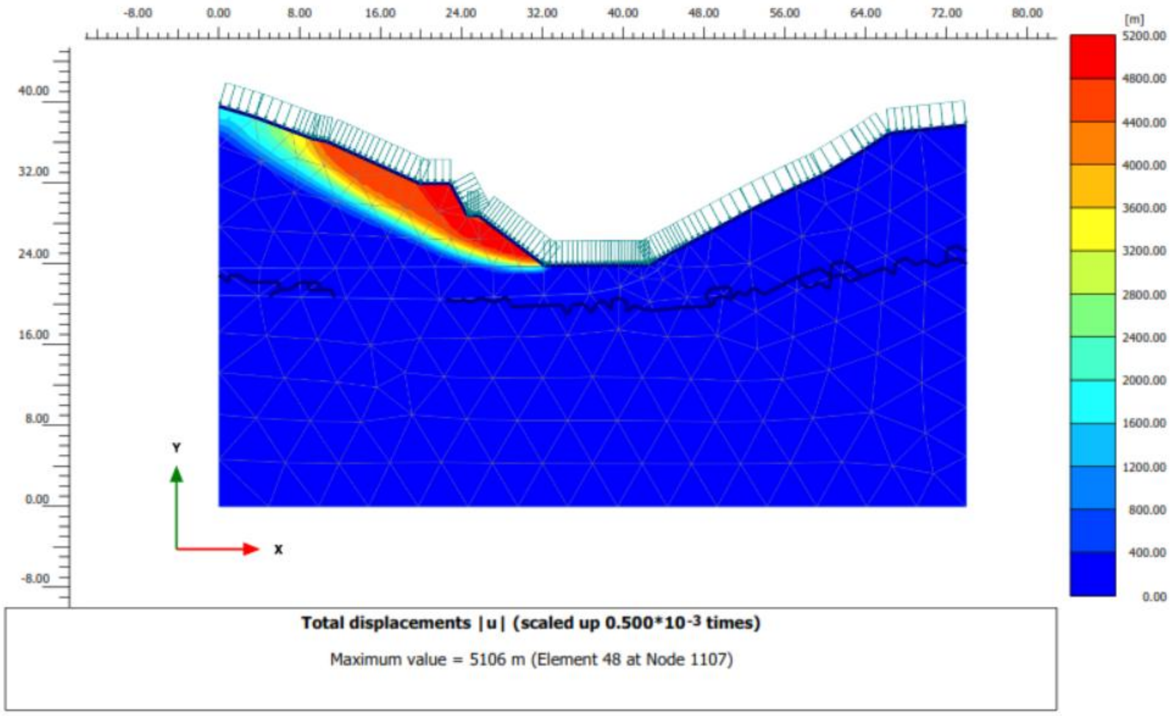

Figure 24. *Displacement vectors and failure mechanism identified in the triggering phase. The results highlight the initiation of a rotational–translational landslide on the left slope sector, with maximum deformations concentrated along the inferred failure surface.*

The obtained curve (Figure 25) illustrates the relationship between the strength reduction multiplier (ΣMsf) and the total displacement magnitude $|u|$. The values of ΣMsf stabilize in the range of 1.0–1.3 even for very small increments of displacement (on the order of 10−3–10−2 m). This rapid stabilization indicates that the model reaches a plastic collapse state almost immediately after loading, with little reserve capacity before failure is mobilized. In the framework of PLAXIS, the safety factor (FS) is directly interpreted as ΣMsf, which means that the system is operating with a factor of safety close to unity. Such a value reflects a condition of critical equilibrium, where the resisting shear strength is nearly exhausted, and the slope cannot sustain additional external actions without failing. The negligible safety margin implied by these results suggests that the slope is highly vulnerable to external perturbations, particularly rainfall infiltration that elevates pore water pressures and reduces effective stresses. Consequently, the numerical analysis provides clear evidence of the slope's high susceptibility to rainfall-induced instability, consistent with the expected failure mechanisms observed in the field.

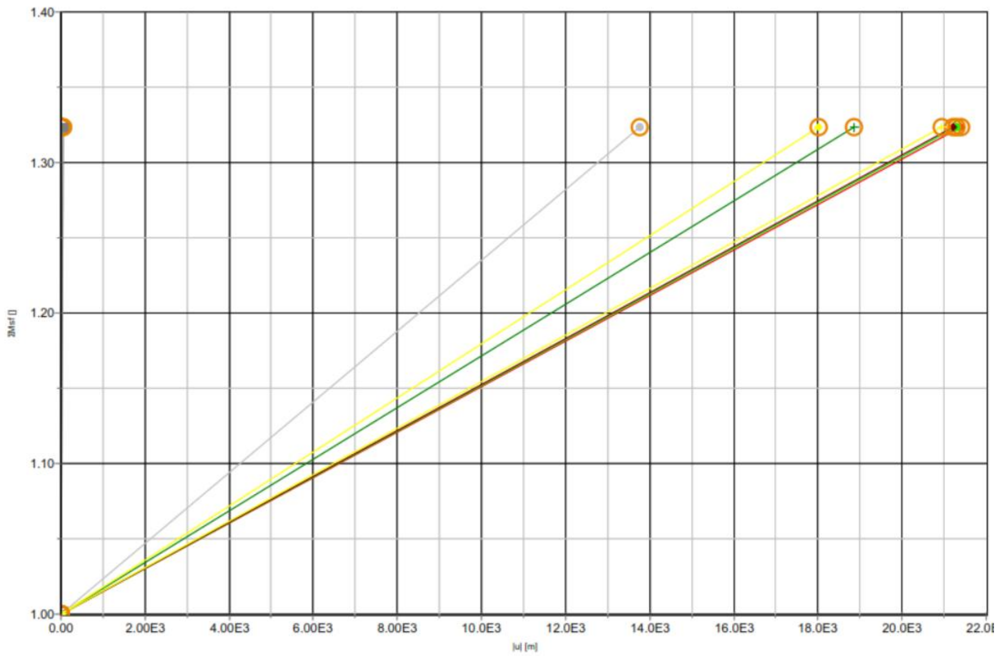

Figure 25. *Relationship between the strength reduction factor (ΣMsf) and total displacement magnitude (|u|).*

The results underline the importance of coupled hydro-mechanical modelling for rainfall-induced landslides. By linking rainfall intensity and duration to pore-pressure build-up and shear strength reduction, FEM simulations provide predictive capability for assessing hazard thresholds and designing mitigation measures.

Chapter five
Results, analysis and remarks

5.1. Soil response to rainfall infiltration

5.1.1. Observation of failure mechanism and displacements

After presenting the procedures adopted for the centrifuge test, it is necessary to discuss in greater detail the process followed to reach the desired acceleration levels. As established in classical centrifuge modelling (Schofield, 1980b)(R. N. Taylor, 1995)(Garnier et al., 2007), the increase in g-level must be progressive in order to avoid abrupt disturbances and to ensure that stress conditions within the soil model develop in a controlled manner.

Following this principle, the container was positioned in the centrifuge and the test commenced at 1g at time 0:00. Subsequently, the acceleration was increased to 5g at 0:04, then to 10g, where it was maintained for 18 minutes.

This incremental process was continued step by step, as documented in Table 9, which records the actual clock time, the elapsed time, the corresponding video sequence, and the gravity level reached. The entire procedure lasted 1 hour and 53 minutes, culminating at 50g. For technical reasons, the rainfall system was activated at 30g, corresponding to 1 hour and 27 minutes into the experiment.

Table 9. *Summary of elapsed time, recorded time, and g-level increments during the centrifuge experiment.*

Real Time (HRS: MINS)	**Record Time (HRS: MINS)**	**Classification**	**Acceleration Level**	**Notes**
11:52	0:00	t_1	1	Start-Spin up
11:56	0:04	t_2	5	Hold per 18 min
12:14	0:22	t_3	10	Hold per 16 min
12:30	0:38	t_4	15	Hold per 16 min
12:46	0:54	t_5	20	Hold per 15 min
13:01	1:09	t_6	25	Hold per 18 min
13:19	1:27	t_7	30	Start rain
13:30	1:38	t_8	30	
13:35	1:43	t_9	52	
13:38	1:46	t_{10}	52	Spin down
13:46	1:53	t_{11}	1	Stop

The interpretation of the slope response was carried out by comparing the contours of the soil surface at the beginning and end of each gravity increment. This approach, widely employed in centrifuge studies of slope stability (Al-Tabbaa & Wood, 1989)(Springman et al., 2001), enables the identification of progressive movements and the evolution of the failure mechanism under controlled boundary conditions. In the present test, the comparison of images showed that between times t_1 and t_2 (Figure 26), corresponding to the increase from 1g to 5g, only negligible displacements could be detected about 0.50 cm, which is consistent with the expectation that at low acceleration levels the stresses are not yet sufficient to mobilize the soil mass.

At 10g, that means t_3, a displacement of approximately 1.63 cm was observed (Figure 27), accompanied by a more pronounced curvature of the slope near the toe. This bulging behaviour, reminiscent of a shallow rotational tendency, has also been described in similar studies as an indicator of the early stages of instability (Take & Bolton, 2002). Between t4 and t5, when the acceleration was increased to 15g, the slope exhibited more significant movement, with displacements of around 4.23 cm (Figure 28). The deformation pattern corresponded to a flow-like failure initiated locally, which then propagated toward the right side of the model.

It must be emphasized that during this stage, water leakage from the rainfall device accelerated the destabilization process, producing failure earlier than anticipated in the design stage, where calculations had estimated initial failure around 50g.

The subsequent increments confirmed the progressive nature of the failure. At 20g (t_5), displacements of 3 cm concentrated again on the right side of the slope (Figure 29), while at 25g (t_6), a further 5.67 cm of movement was recorded (Figure 30). The geometry of the surface deformation at this point suggested the development of a more continuous failure surface, consistent with observations from centrifuge studies on rainfall-induced landslides (Ng et al., 2003)(Take et al., 2004b). At 30g (t_7), when rainfall simulation formally began, visible changes were initially limited (Figure 31). However, by t_8, still under 30g, additional displacements of about 5.64 cm were observed (Figure 32), with failure surfaces exhibiting both curved and planar segments, indicating a compound mechanism.

Finally, from t_9 to t_{11}, as acceleration was increased to 50g, no major additional displacements were recorded, suggesting that the critical phase of failure had already been triggered (Figure 33).

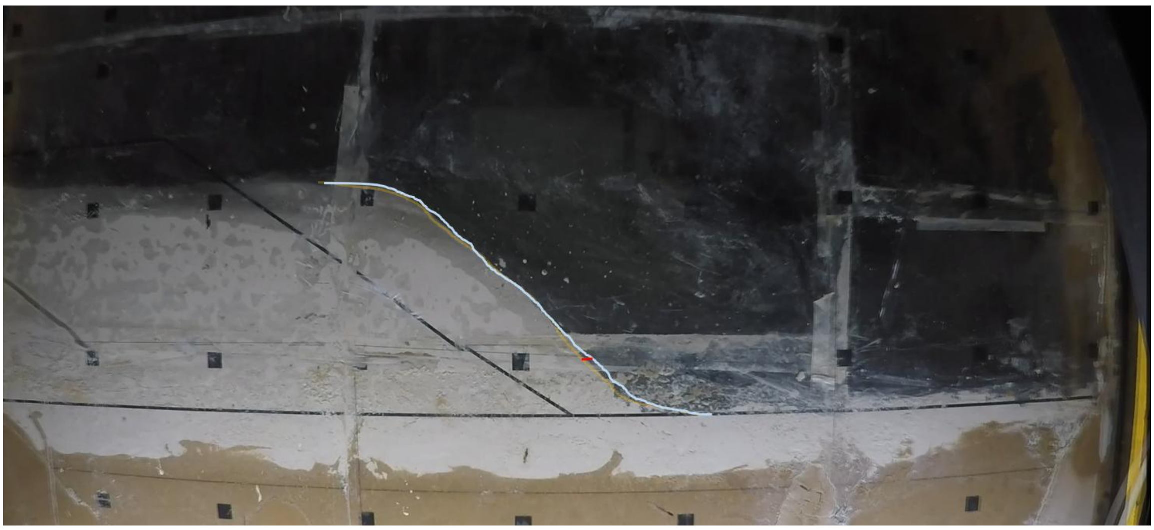

Figure 26. *Time-lapse slope deformation through contour overlays from t_1 (1g) to t_2 (5g).*

Figure 27. *Time-lapse slope deformation through contour overlays from t_3 (10g) until before reaching the t_4 (15g).*

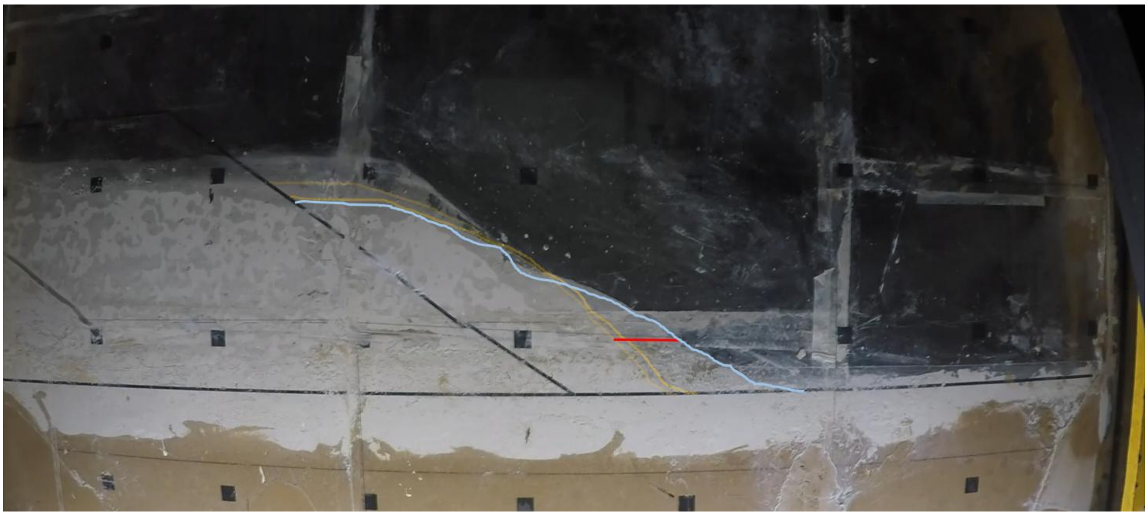

Figure 28. *Time-lapse slope deformation through contour overlays from t_4 (15g) until before reaching the t_5 (20g).*

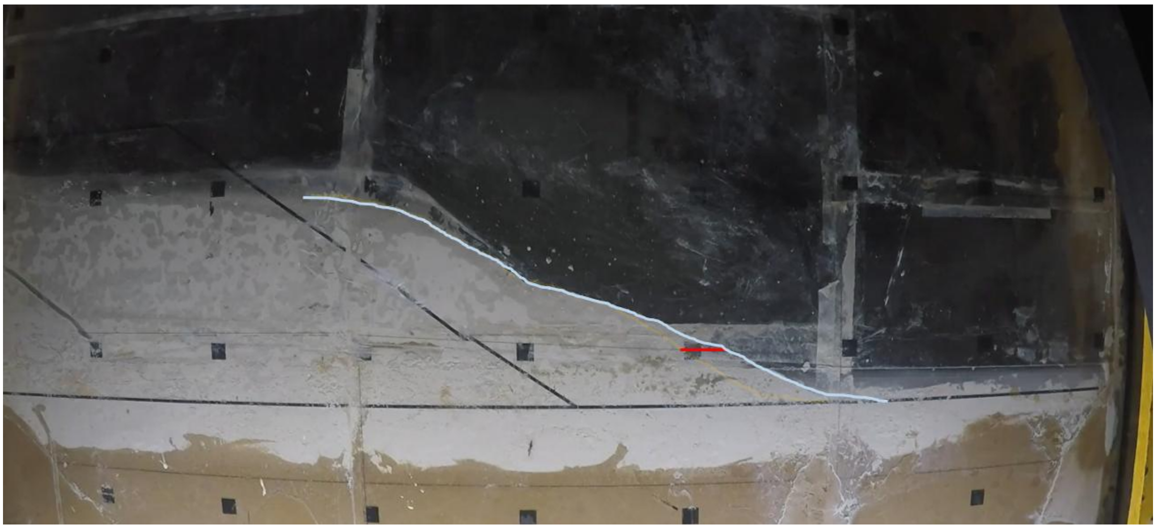

Figure 29. *Time-lapse slope deformation through contour overlays from t_5 (20g) until before reaching the t_6 (25g).*

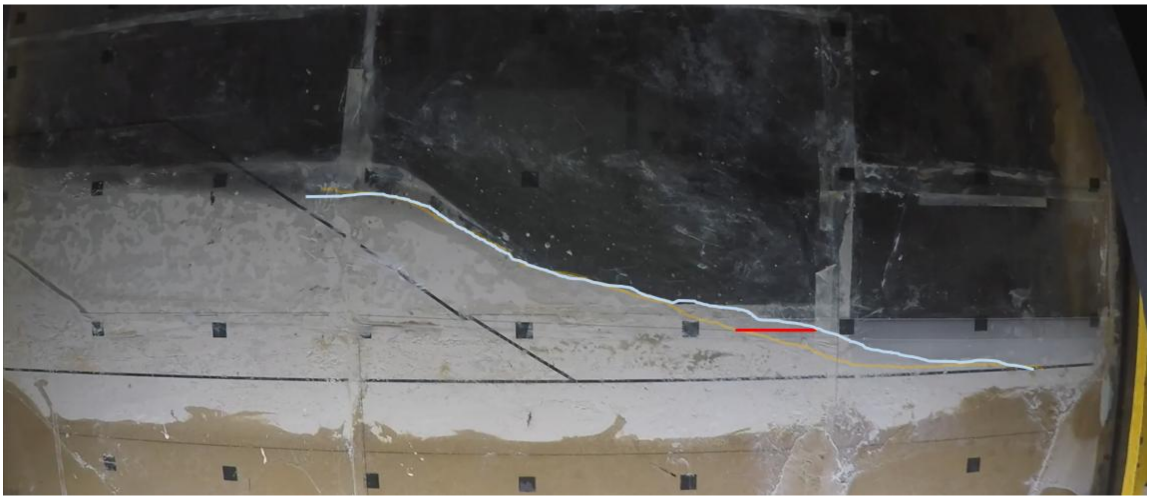

Figure 30. *Time-lapse slope deformation through contour overlays from t_6 (25g) until before reaching the t_7 (30g).*

Figure 31. *Time-lapse slope deformation through contour overlays from t_7 (30g) until before reaching the t_8 (30g). Start of the rain simulation.*

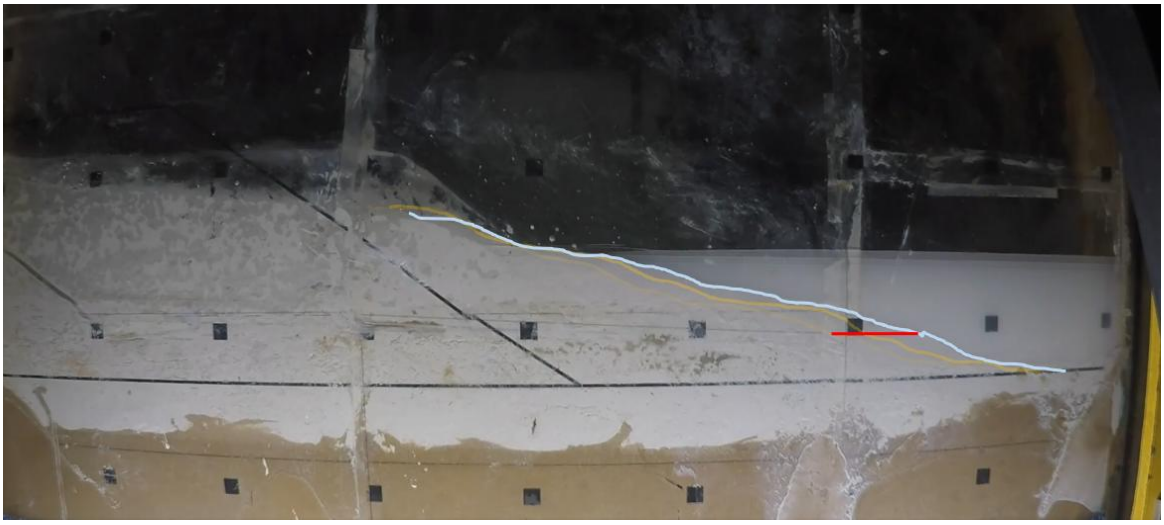

Figure 32. *Time-lapse slope deformation through contour overlays from t_8 (30g) until before reaching the t_9 (50g). Continuing with the rain simulation.*

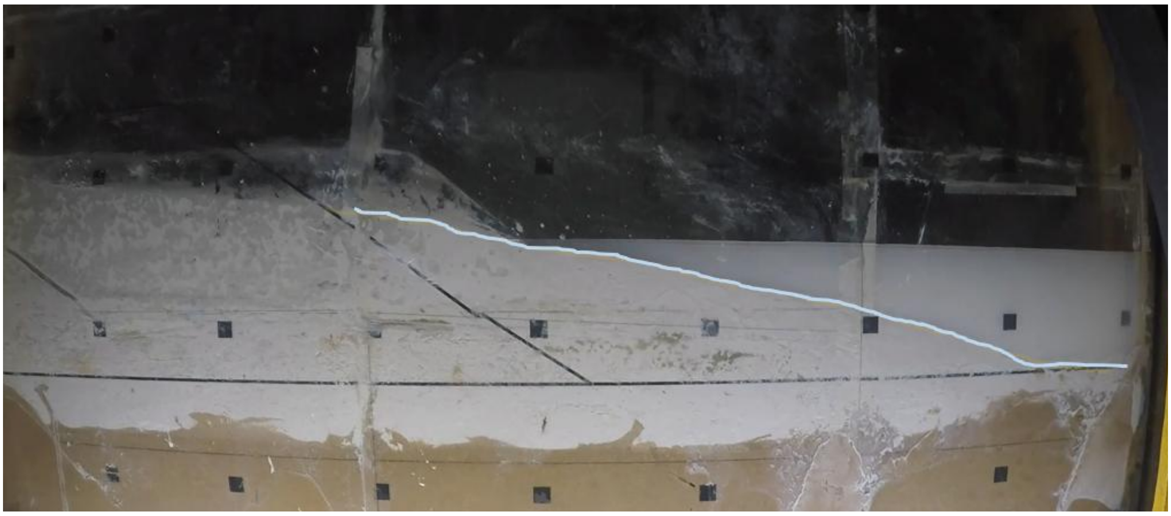

Figure 33. *Time-lapse slope deformation through contour overlays from t_9 (50g) until the end of the test t_{11}. Continuing with the rain simulation.*

5.2. *Interpretation of failure mode in Himera I*

From the beginning of the test (t_1) to its conclusion (t_{11}), cumulative displacements of approximately 22 cm were measured across the slope model. These displacements were not uniform, but rather showed a progressive concentration toward specific zones of weakness, particularly in the lower right portion of the slope, where the toe experienced more accentuated movements.

The failure mechanism, as illustrated in Figure 34, revealed a complex and composite behaviour that combined both rotational and translational components. Initially, the slope exhibited shallow deformations resembling a rotational tendency, which gradually evolved into larger translational movements as the test advanced and higher g-levels were reached. The global failure surface, therefore, did not correspond to a simple geometry but reflected the superposition of localized mechanisms that ultimately joined to form a continuous path of instability.

In addition, the introduction of rainfall simulation at 30g had a decisive influence on the failure process. The infiltration of water accelerated pore pressure build-up and reduced soil strength, enhancing deformation rates and contributing to the onset of failure earlier than initially predicted. The rainfall input, combined with a minor hydraulic leakage in the system, generated conditions that mimicked the sudden loss of stability observed in natural slopes subjected to intense precipitation. This highlights the strong coupling between hydraulic boundary conditions and mechanical response, where even moderate rainfall can trigger significant slope movements under critical stress states. These findings are consistent with established literature on centrifuge modelling of slopes, where compound failure modes are often observed under rainfall infiltration conditions, particularly when hydraulic anomalies such as unintended leakage affect pore water pressures (Gottardi & Butterfield, 1993)(Kimura et al., 2010).

The experiment therefore provides valuable insights, not only by confirming the occurrence of a global failure mechanism within the model, but also by quantifying the magnitude of displacements and identifying the influence of rainfall simulation. Together, these results contribute to a deeper understanding of rainfall-induced landslides under accelerated gravity fields, and they represent a solid basis for the validation of numerical analyses and for illustrating the intricate interaction between hydrological processes and geomechanically response.

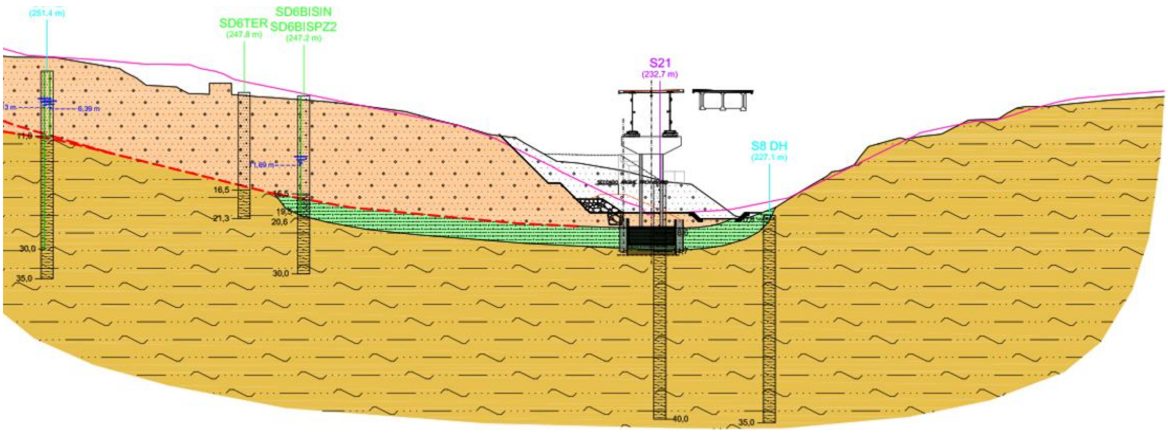

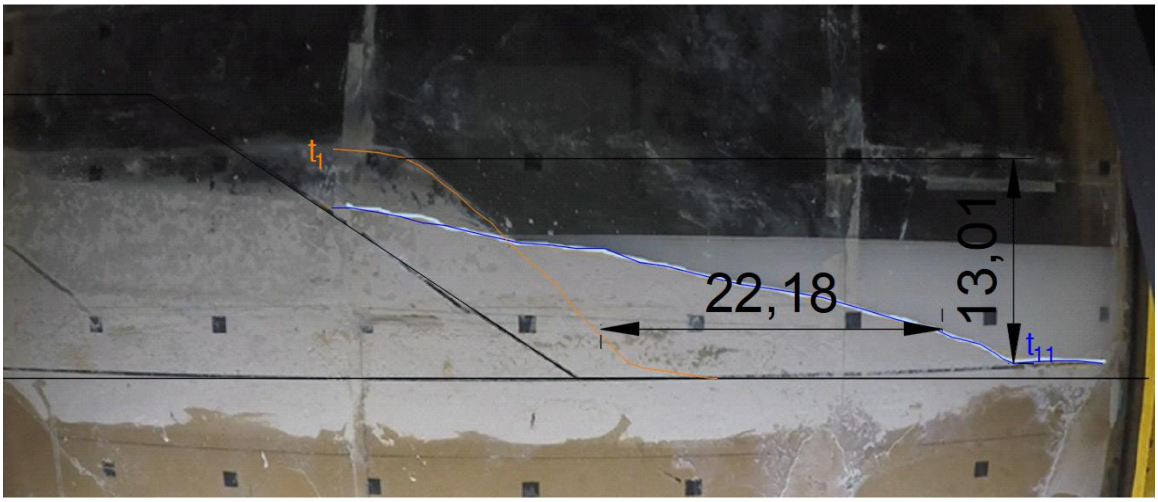

Figure 34. *Comparison between the landslide movement found in the Himera I area after being triggered by rain vs. the result obtained through the centrifuge test with the rain simulation equipment.*

Experimental and modelling results reported in the literature show that the presence of weak layers with a high content of cohesive fines plays a critical role in rainfall-induced slope instabilities. Centrifuge studies (Take et al., 2004) demonstrated that the development of transient pore water pressures in layered soils or heterogeneous hydraulic conditions can trigger a sudden transition from a slow-moving slide into a rapid flow, even without the occurrence of static liquefaction. Similarly, Hudacsek et al. (2015) evidenced that variations in water content and climatic conditions produce cumulative deformations in clayey soils, progressively reducing the available strength. Wang et al. (2010) highlighted that weak layers with apparent cohesion, due to their higher compressibility and permeability compared to underlying strata, concentrate rainfall infiltration and control the evolution of the failure process.

The physical modelling conducted in the geotechnical centrifuge must be interpreted through the corresponding scaling laws to ensure a meaningful extrapolation to prototype conditions. Under N-g scaling, stresses in the small-scale model correctly replicate those of the full-scale slope, but displacements, time of failure initiation, and pore-pressure response must be adjusted using $1/N$, $1/N^2$ and other similarity relations.

For instance, rainfall infiltration processes in a centrifuge do not perfectly reproduce the hydraulic conductivity contrasts or preferential flow paths that may exist in the field, which may lead to differences in the rate of pore-pressure generation. Likewise, localized deformations observed in the model represent analogue mechanisms rather than exact magnitudes of prototype displacements. Despite these limitations, the centrifuge tests successfully reproduced the sequence of instability processes observed in Himera I, allowing the identification of key triggering conditions, deformation patterns and failure mechanisms that informed the subsequent FEM simulations.

In this context, it was observed that the first layer of the slope, composed of 50% clay, 40% sand, and 10% silt, with a water content close to 50%, acted as a weak layer. This condition promoted the accumulation of infiltration water and the increase of localized deformations, accelerating the triggering of the landslide. So, as could be seen the soft first layer presents considerable permeability and compressibility, substantially impacting slope failure behaviour through alterations in the processes of infiltration and deformation when subjected to rainfall. Therefore, the influence of weak layers requires thorough assessment, focusing on the interaction between infiltration, deformation, and failure in slopes under rainfall conditions.

Consequently, the analysis of the clayey layer should address not only the shear strength parameters under saturated conditions, but also its deformation capacity under infiltration, the evolution of pore pressure, and the transition from an initial rotational failure mechanism to a potential progressive slide. These findings consistently underline that cohesive weak layers are the initiation and propagation zones of instability under intense rainfall conditions.

5.3. Comparison with Numerical model

In the Figure 35 presents the finite element analysis (FEM) results obtained in PLAXIS, applying the strength reduction method under rainfall-induced pore pressure increase. The numerical simulation captures the evolution of plastic points and the localization of the failure surface along the orange/yellow soil interface, consistent with the failure geometry documented in both the centrifuge test and the field evidence. The computed safety factor (FS ≈ 1.0) indicates a state of limiting equilibrium, confirming the slope's susceptibility to failure under hydro-mechanical forcing.

Taken together, the three perspectives: field evidence, centrifuge modelling (Figure 34), and FEM analysis (Figure 35) converge toward a coherent interpretation: the landslide was primarily controlled by the mechanical weakness of the superficial deposits and their hydrogeological response to rainfall infiltration. The agreement across scales validates the reliability of the adopted methodology and underlines the critical role of combined experimental–numerical approaches in assessing rainfall-induced slope instability. The three representations provide a complementary perspective on the Himera I landslide, integrating field-scale evidence, physical modelling, and numerical simulation.

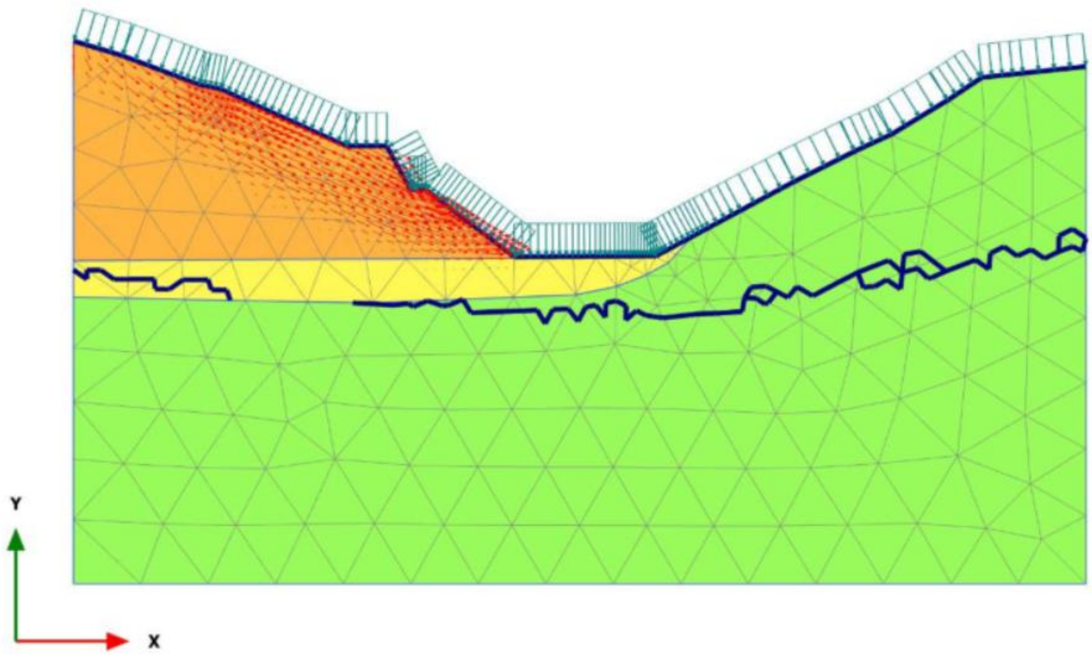

Figure 35. Finite element method (FEM) analysis of the Himera I slope in PLAXIS 2D, illustrating plastic points and failure surface localization under rainfall-induced pore pressure increase.

Chapter six

Documentation of the Physical Model

6.1. Model construction process

The stability verification of the slope was performed over a length of approximately 200 m upstream from the viaduct location Figure 36. Given the mainly cohesive nature of the soils, and consequently their low permeability, a total stress (undrained) condition was considered due to the sudden application of the loading induced by the mass of sliding material from the upper slope.

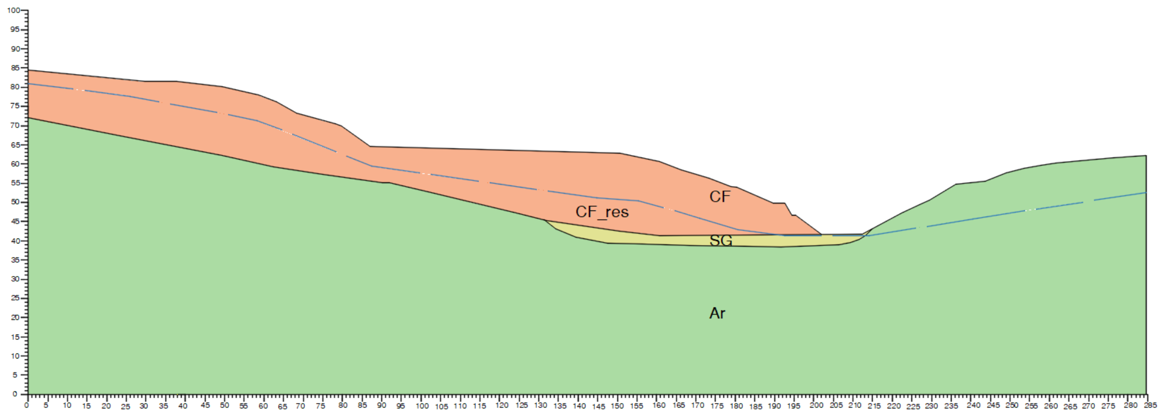

Figure 36. *Location and geological context of the Imera I landslide area, showing the affected section of the viaduct and slope morphology.*

The intense rainfall, combined with the additional load, jointly led to the onset of instability conditions.

To preserve the correct prototype soil behaviour (e.g., identical stress and strain conditions in the model), a centrifuge can be used to increase the gravity field magnitude (by a factor of N) to offset the stress reduction caused by the smaller size.

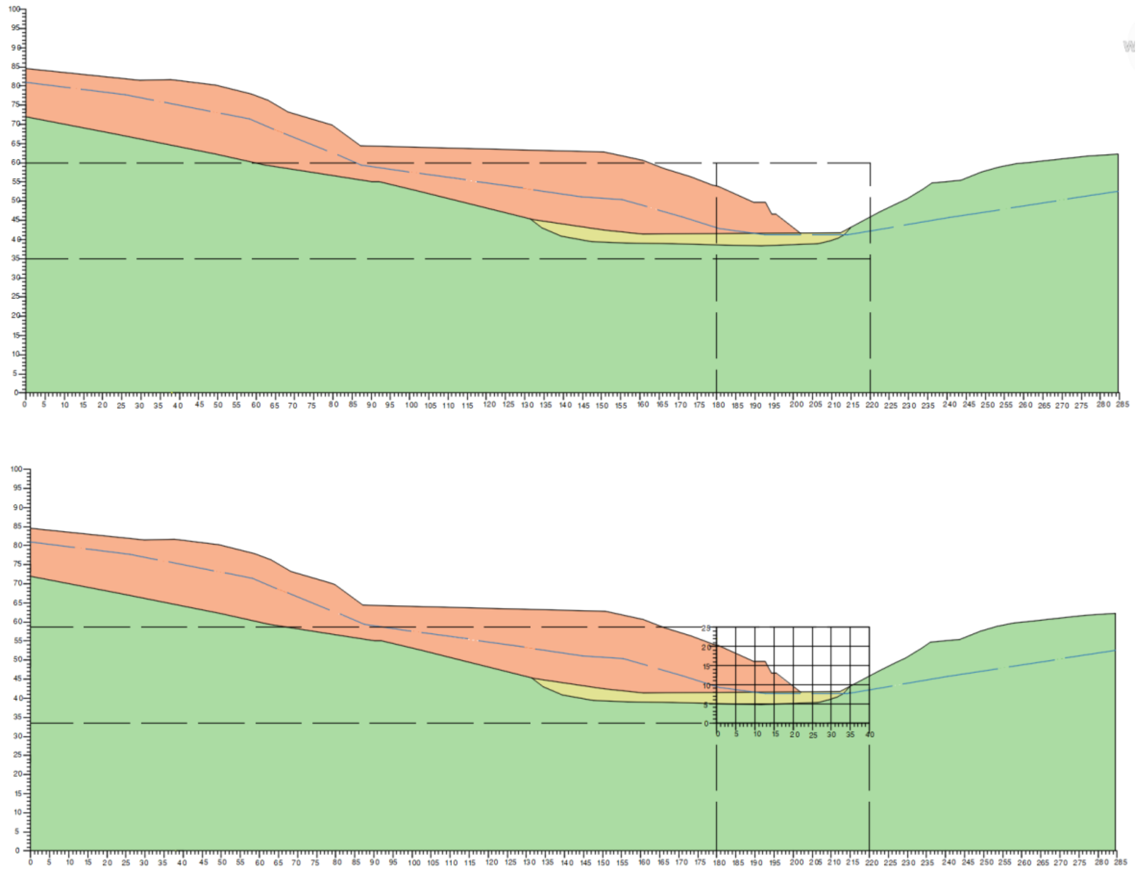

Figure 37. *Construction sequence of the centrifuge model, including drainage layer, sand foundation, and clay deposition under 50-g consolidation.*

Validation of the model was carried out through centrifuge testing using the 3.5 m diameter beam centrifuge and rainfall simulator at the University of Dundee. The model to be tested represents a slope of 1:1.5 ($\beta_0 \approx 36°$) at 1:50 scale under 50-g. Unless otherwise indicated, all subsequent dimensions and properties are given at prototype scale at 50-g (Figure 38).

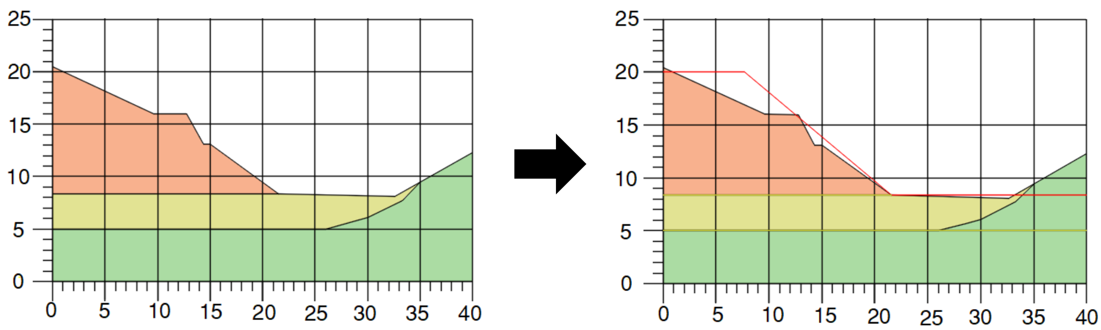

Figure 38. *Pre-final slope configuration of the centrifuge model before rainfall infiltration test, with dimensions scaled at 1:50 under 50-g.*

Based on the measurements of the study area, a case simplification was performed to develop the scale model (Figure 39).

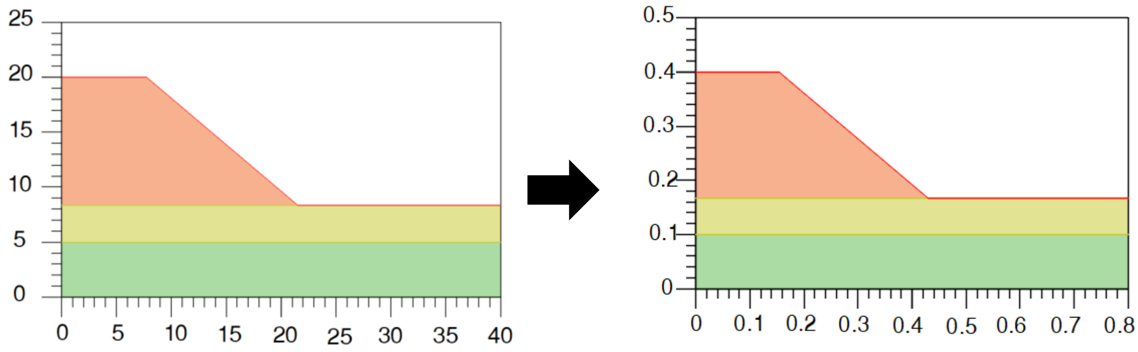

Figure 39. *Final slope configuration of the centrifuge model before rainfall infiltration test, with dimensions scaled at 1:50 under 50-g with the container dimensions.*

6.2. Equipment setup

The established scale considered the container dimensions of W500 × L800 × H550 mm (Figure 40).

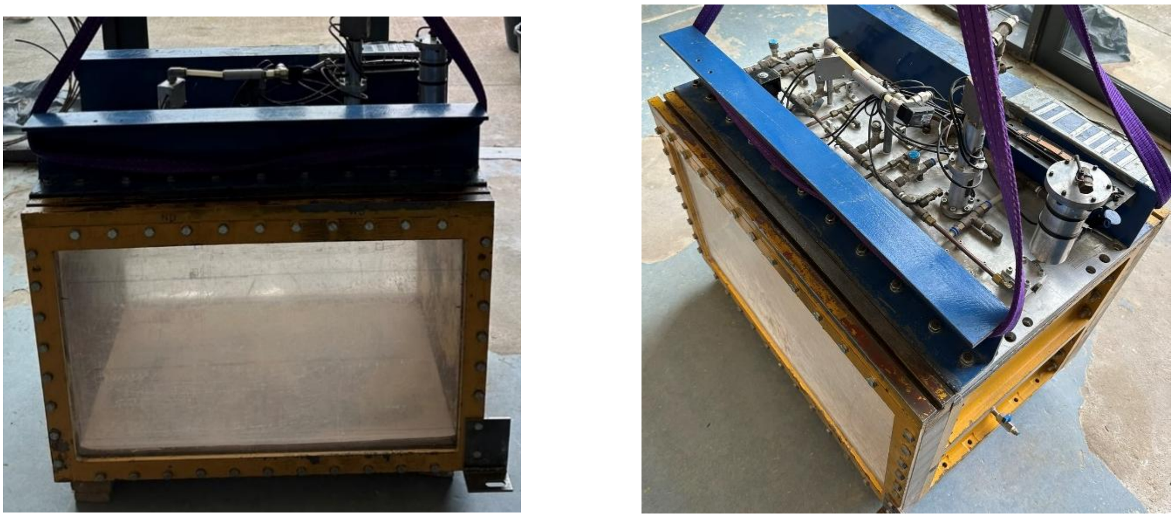

Figure 40. *Experimental setup with rainfall simulator mounted on the centrifuge container, prepared for triggering infiltration-induced failure.*

6.3. Photos of construction and text execution

The construction process will consist of the following steps:

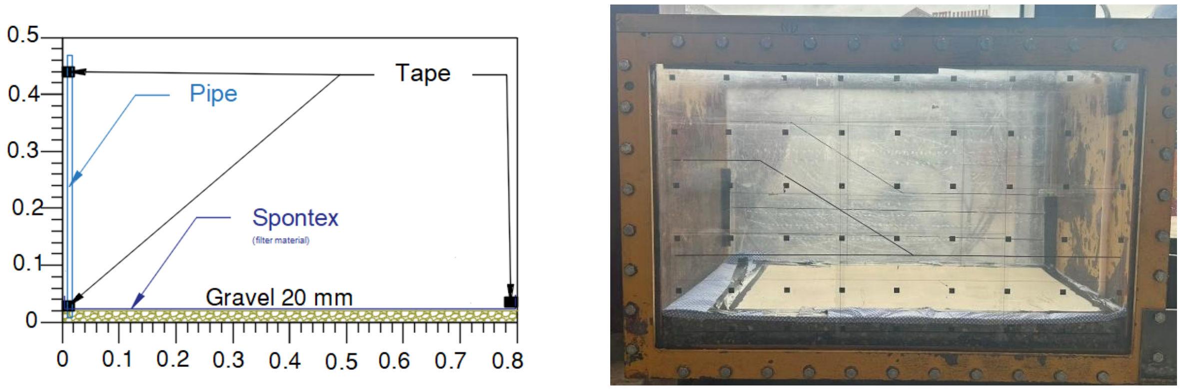

Figure 41. *Experimental setup showing the drainage layer construction with gravel, filter material, and pipe installation in the centrifuge container.*

1. Place the pipe (secured with tape).
2. Place 20 mm of gravel to create the permeable layer allowing drainage during testing.

Place a filter material (Spontex) above the gravel to prevent mixing with the overlying sand while allowing water to pass (secured with tape).

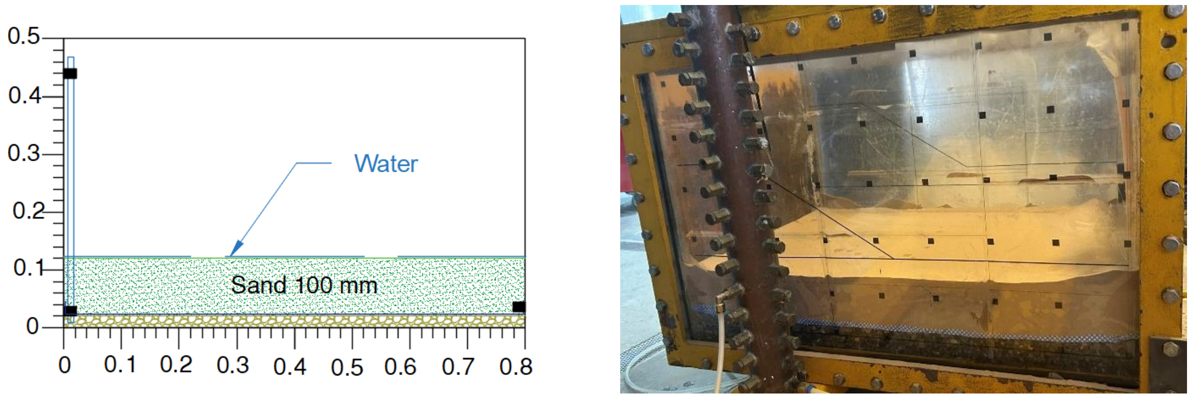

Figure 42. *Experimental setup after deposition of the sand layer and initial water saturation.*

3. Using air pluviation, place 100 mm of HST95 silica sand.
4. Set the water table at the top of the sand layer.

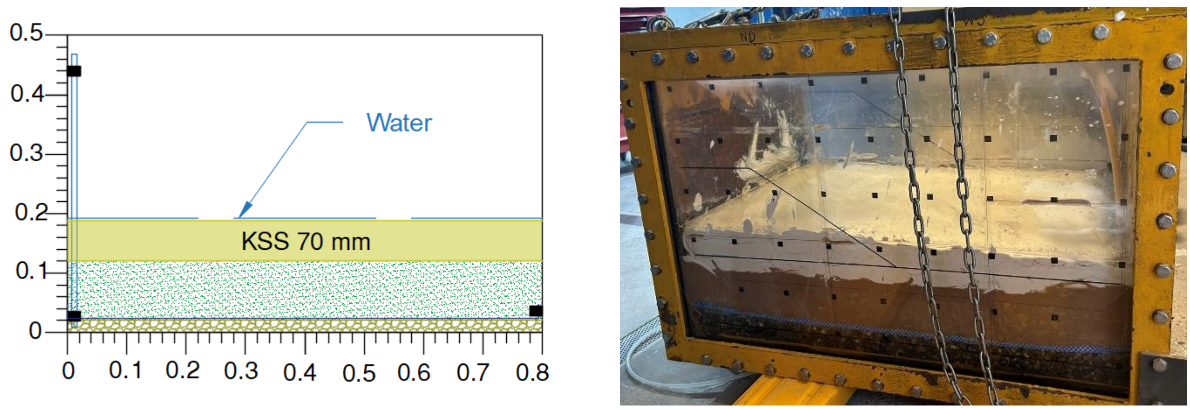

Figure 43. *Experimental setup after slurry deposition of the first clay layer (70 mm thickness) and addition of water.*

5. Place a 70 mm layer of KSS541 clay using slurry deposition.
6. Add a water layer reaching the top of the clay and exceeding it by 1 in (25.4 mm).
7. Spin at 50-g to consolidate the clay (estimated centrifuge time: ~0.5 days).

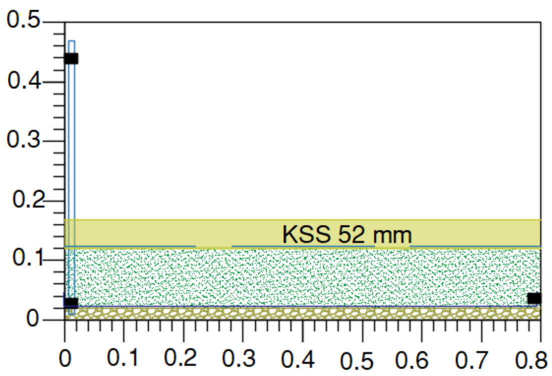

8. After consolidation, expect a 25% height reduction.
9. Remove excess water via the external container valve, ensuring that the water table is maintained at the sand layer elevation by means of the hose.

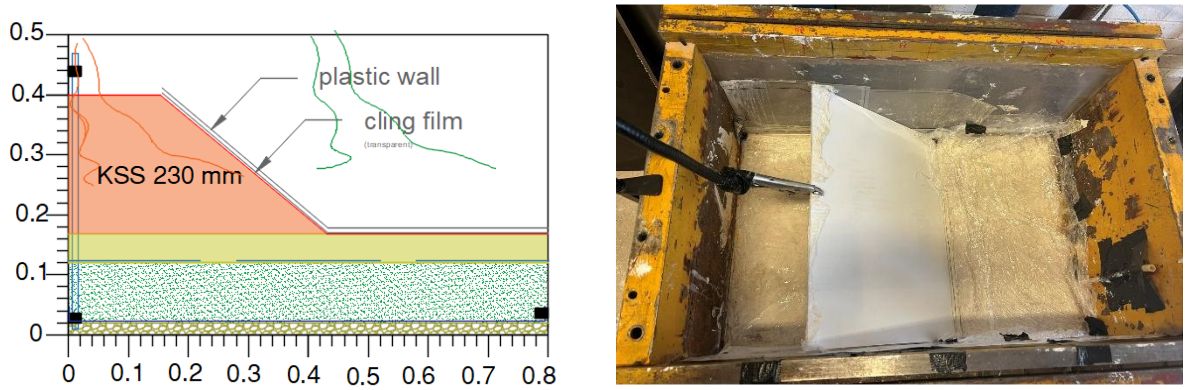

Figure 44. *Experimental setup after deposition of the second clay layer (52 mm thickness), followed by placement of the upper clay slope (230 mm thickness) using plastic wall support.*

10. Using two lamp clamps as external arms, fix cling film and a plastic sheet to form the desired slope.
11. Place KSS541 clay on one side and sand on the other (sand chosen for ease of later removal).

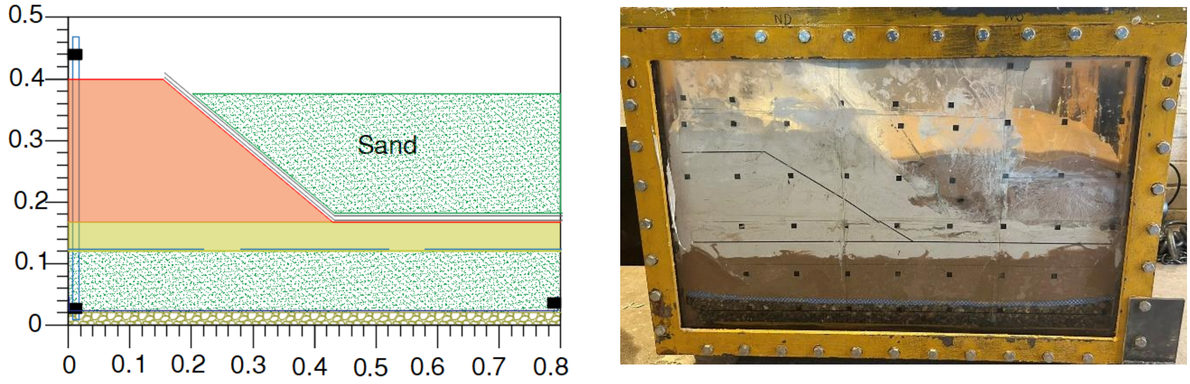

Figure 45. Consolidation stage of the 230 mm clay slope in the centrifuge container under 50-g acceleration.

12. Spin at 50-g to consolidate the 230 mm clay layer (estimated centrifuge time: ~1.7 days).
13. Maintain the water table at the sand layer height using the container's hose control valve.

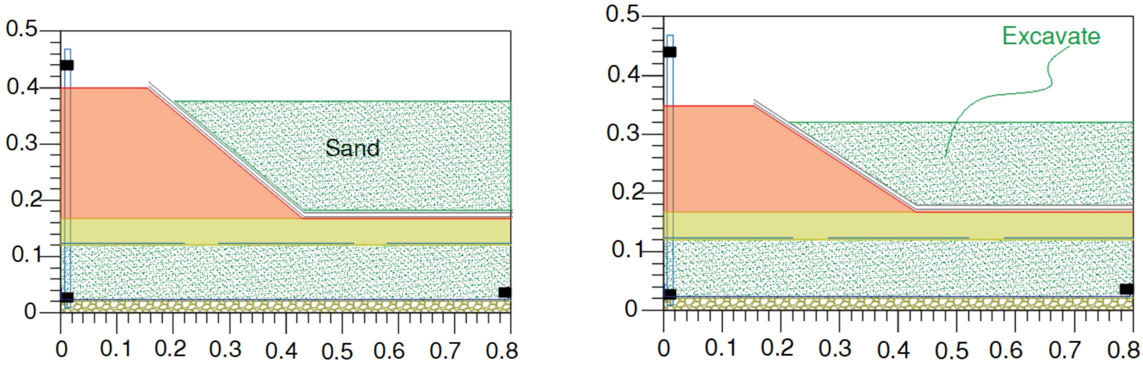

Figure 46. *Excavation of the right-hand sand support after consolidation, exposing the clay slope profile.*

14. After consolidation (25% height reduction), remove the sand from the right-hand side.

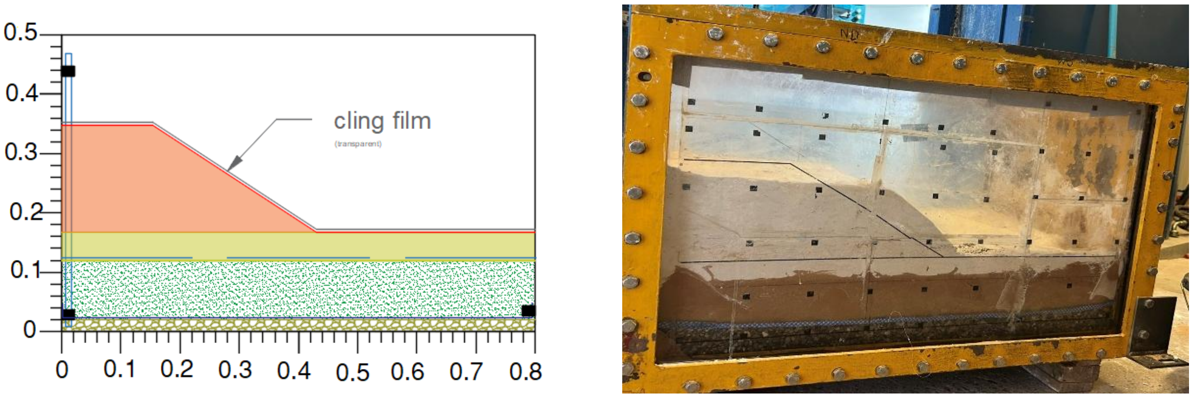

Figure 47. *Experimental setup after removal of the plastic wall, with cling film left in place to preserve the slope configuration.*

15. Carefully remove the plastic wall to avoid altering the slope configuration.
16. Keep the cling film in place to prevent clay drying until the final test.

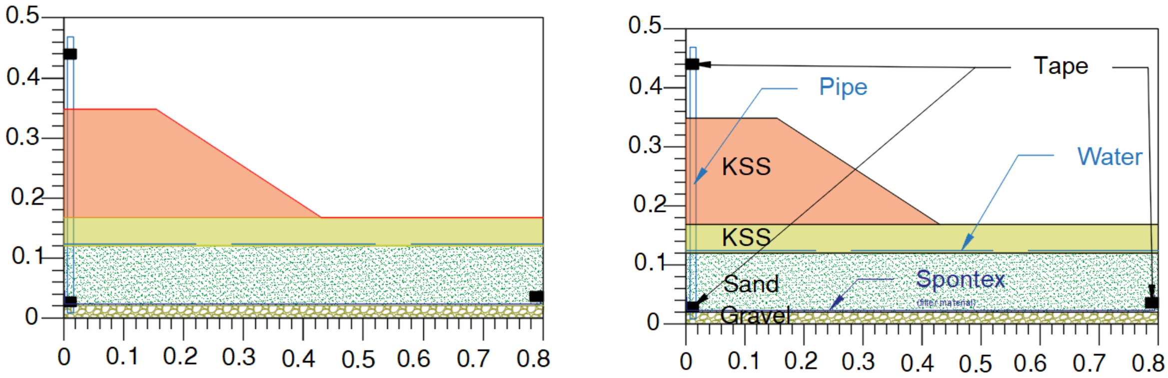

Figure 48. *Final configuration of the slope model in the centrifuge container, including drainage, sand, clay layers, and rainfall simulator setup.*

Figure 49. *Centrifuge apparatus with the container filled with the slope model and rainfall simulator cover installed, ready for testing.*

The final configuration was ready for centrifuge testing.

Chapter seven

Landslide risk – Systematic approaches to assessment and management

7.1. Framework for landslide risk management

7.1.1 General framework

The site observations, construction details, and documented performance of the Himera I infrastructure presented in Chapter 6 provide the contextual basis required to interpret the experimental and numerical results. These elements connect directly with the hazard and risk framework developed in Chapter 7, where the mechanisms identified through centrifuge modelling, FEM simulations, and field evidence are integrated to evaluate the rainfall-induced instability. This transition highlights how the understanding of failure processes supports a coherent assessment of hazard, exposure, and risk for the Himera I site.
According to Fell & Hartford (1997) risk management process can be categorized into three components:

1. Risk analysis
2. Risk assessment, and
3. Risk management.

Risk analysis and risk assessment are sub-sets of risk management and risk analysis is a subset of risk assessment as illustrated in Figure 50.

In contrast, in an engineering standards approach, the level of safety is not known, rather those design, construction and maintenance standards that have proven to be successful in the past, form the bases for decision-making. Standards usually increase if a standards-based engineered facility fails, because failure of an engineered facility, represents to many, failure of engineering: In terms of standards-based approaches, the engineering profession is almost completely in control of the level of safety of engineered facilities. We use the term "almost" to indicate that engineering standards are not solely decided by engineers, the requirements of the courts, economics and public expectation also play a role.

Unfortunately, there is no unified framework to integrate all of the components of the standards-based approach, and the engineering profession often finds itself trying to balance the often-conflicting interests of owners, who pay the engineers fees and the public who would be affected by the failure of the facility. One consequence of this is the enormous legal liability carried by engineers, a liability that in many cases is rather more onerous than that associated with other professions that deal with matters of public safety (Fell & Hartford, 1997).

Conversely, risk-based methods involve acceptance of failure as an inevitable consequence of society's need for engineered facilities. Failure is permissible provided the risks (probability of failure x consequences) are tolerable. Risk based methods, when used for safety evaluations of existing facilities do not involve the concept of "designing for failure", and many of the criticisms of risk-based engineering do not apply.

Risk management techniques provide an integrated approach to safety decision-making and have the advantage that the engineer is not faced with having to determine what is an appropriate level of safety, this is done by those policy makers who are responsible for these matters. The engineers perform the risk analysis and provide a measure of how safe a facility is. How safe it needs to be is determined by the owner and the government body that represents the public (regulators) (Fell & Hartford, 1997).

Engineers can provide various risk management related services in addition to analysing risk; they can even assist decision makers in developing decision analysis techniques and in choosing appropriate decision criteria, without being responsible for the actual decision.

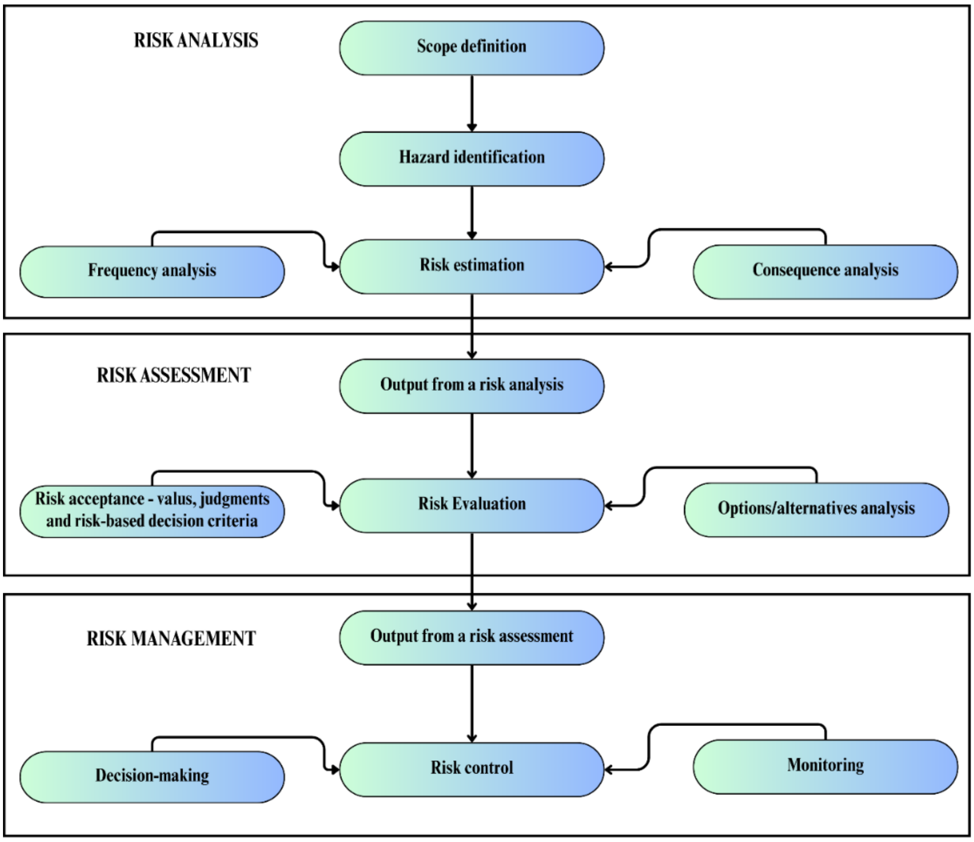

Figure 50. *Risk management process (Fell & Hartford, 1997).*

7.1.2 Landslide risk analysis

Risk analysis can be practiced at various levels of detail, ranging from qualitative evaluations to detailed quantitative risk analyses. Detailed quantitative methods of analysis using event trees and fault trees and incorporating probabilistic formulations of loads and probabilistic ultimate limit state analysis models, provide a basis for measuring how safe a slope is. This type of analysis permits comparison of the analysed risk risk-based decision criteria (Fell & Hartford, 1997).

This is not to say, however, that less detailed, analysis-based methods such as those using geomorphological and/or historic based methods to estimate probability of sliding, are not valid approaches to quantitative risk assessment (Varnes, 1984).

Landslide risk analysis is an iterative process, whereby initially a broad appreciation of the hazard, its probability of occurrence, and the resulting consequences is developed. This screening process permits identification of those issues which appear to contribute most to the total risk and enables those less important issues to be screened out in a systematic, identifiable and rational manner. Those that remain are then subjected to more rigorous analysis, with further even more detailed analysis carried out subsequently if necessary (Fell, 1994).

The engineering analysis of landslide risks has essentially two components, the probability of occurrence and the resulting consequences. The deterministic approach to slope design usually requires assessment of a factor of safety, from the geometry, shear strength and pore pressures. This requires as a prerequisite, an assessment of the likely mechanisms of failure (Fell & Hartford, 1997).

By contrast. landslide risk assessment requires the addressing of a larger number of questions. These include, according to Fell & Hartford (1997):

- what is the slope geometry, geology, groundwater (and surface water) and potential movement mechanisms?
- will a landslide or landslides initiate on the slope, what are the probabilities of the initiation of sliding, and what are the causes (e.g. rainfall, snow melt, freeze, thaw, earthquake, deforestation, construction activity) ?
- where will the landslide(s) be on the slope, what volume, and what mechanisms will be responsible?
- what will be the velocity of movement?
- will there be warning signs (e.g. cracks, movement, which will allow mitigation of the probability of sliding, or of the consequences, by for example, evacuating persons)?
- will the initial movement mobilise to a second phase (which is for example more rapid, e.g. a debris flow)?
- how far, how fast will the landslide move?
- what property and/or persons will be reached by the landslide, and what is their temporal probability?

- what is the vulnerability of the property and persons to the landslide?
- what is the risk to property and persons?

This may seem much more complicated than the standard approach, but in reality, it is only formalizing the thought process and decision framework, and then putting it into a risk context.

Several authors have discussed the specifics of the framework for landslide risk analysis including Varnes (1984), Einstein (1988), Hartlen & Viberg (1988), Christian et al. (1992), Morgan (1991), Morgan et al. (1992), Fell (1994), Anderson et al. (1996), Leroi (1996) and Wu et al. (1996).

When assessing probabilities, it is usually easier, and more likely to be accurate, to consider the conditional probabilities (Fell & Hartford, 1997). For example (adapted from Morgan et al. 1992):

$$R(DI) = P(H) \cdot P(S|H) \cdot P(T|S) \cdot V(L|T)$$

where

$R(DI)$ is the risk (annual probability of loss of life to an individual);

$P(H)$ is the annual probability of the hazardous event (the landslide);

$P(S|H)$ is the probability of spatial impact (of the landslide impacting a building) given the event;

$P(T|S)$ is the probability of temporal impact (e.g. of the building being occupied) given the spatial impact;

$V(L|T)$ is the vulnerability of the individual (probability of loss of life of the individual given impact);

For a case involving property damage the equivalent expression would be:

$$R(PD) = P(H) \cdot P(S|H) \cdot V(P|S) \cdot E$$

where

$R(PD)$ is the risk (annual loss of property value);

$P(H)$ is the annual probability of the hazardous event (the landslide);

$P(S|H)$ is the probability of spatial impact;

$V(P|S)$ is the vulnerability of the property (proportion of property value);

E is the element at risk (e.g. the value of the property);

By assessing risk in this manner, it will be easier to assess the conditional probabilities and vulnerability and allow for different locations within the main body of a landslide or the accumulation zone it moves on to, occupancy patterns, and the effect of warning measures (in allowing persons to flee a potential landslide and hence reduce $V(L|T)$).

When risk is being assessed not in lives lost, but as the cost of damage, e.g. to a building, we need to be specific about what is the "element" at risk. For example, the vulnerability of an "element" consisting of a room in a house situated adjacent to a small landslide might be high, e.g. 0.8, but if the "element" was the house as a whole, which was unlikely to suffer overall damage as a result of the small landslide, the vulnerability might only be low, e.g. 0.1. Even when considering risk as lives potentially lost, the vulnerability of a person who sleeps in that bedroom will be higher than the other occupants of the house (Fell & Hartford, 1997).

The vulnerability of lives and property damage may also be quite different. A house may have similar and high vulnerability to a slow and a rapid landslide, but persons living in the property may have a low vulnerability to the slow landslide (they can move out of the way) but a higher vulnerability to the rapid landslide (Fell & Hartford, 1997).

7.2. Examples of Frameworks for risk assessment for lansliding

7.1.3 Himera I, A19, Sicily, Italy

The problem

On April 10, 2015, a major landslide occurred on the right bank of the Fiume Imera, directly affecting the A19 motorway viaduct between piers 16–22. The reconstruction project focused on re-establishing the viaduct deck; however, the stabilization of the landslide body was not included in the scope. Since then, the area has been subjected to a continuous geomorphological–geotechnical monitoring program with inclinometers and piezometers positioned across the active scarp and riverbed reconfiguration works.

Stratigraphically, the slope is composed of landslide deposits (colluvium/remolded soils) typically 10–15 m thick and reaching up to ~25 m in the upper section, overlying the Numidian Flysch (sandy silts, clays, and marly clays). Groundwater levels were measured at depths of 6–15 m below ground level in dry seasons.

Historical evidence includes a 2005 landslide (multiple rotational movement with successive reactivations), later incorporated into the 2015 mass movement.

The surrounding valley is mapped as a landslide-prone landscape, with repeated evidence of slow-moving flows, complex landslides, and debris slides across clay-rich terrains in the PAI hazard zoning.

Instrumentation includes automated piezometers (e.g., SC2-PZ1, SC2-PZ2, SE3-PZ1, etc.) with known plan coordinates and ground elevations, providing long-term series of groundwater head (*soggiacenza*) from 2016 to 2019/20.

Comments on the nature of landsliding in the Himera I

- Dominant mechanism: Geological cross sections and borehole data indicate a deep-seated rotational–translational composite slide, with reactivation along the contact between landslide debris and Flysch. Residual shear parameters are considered critical along this interface.
- Material and geological control: The clayey Numidian Flysch is highly sensitive to weathering and pore pressure increases, providing the structural weakness for sliding. Overlying landslide debris shows strong thickness variability.
- Triggering factors: Regional evidence confirms that rainfall-induced pore pressure increase is the dominant trigger. The 2015

event coincided with exceptional rainfall accumulation (see Caltavuturo and Scillato rainfall stations).

- Hydrogeology: Automated piezometers confirmed strong seasonal fluctuations; installation depths (e.g., SC3-PZ1 at 24.5 m, SC3-PZ2 at 14 m) enable conversion of *soggiacenza* (depth-to-water) into absolute head elevations.

Risk assessment framework

1) Risk Analysis

Hazard scenarios (H):

- H1 – Reactivation of the deep-seated landslide due to pore pressure build up from prolonged rainfall, mobilizing the main mass down to the riverbed. Supported by sliding surface geometries and the need for residual strength parameters.
- H2 – Shallow slides and debris flows within the upper colluvium during high-intensity storms. Consistent with regional hazard inventories.
- H3 – Toe erosion by the Fiume Imera, which reduces basal support during flood events. Mitigation through river reconfiguration was included in reconstruction works.

Conditional probabilities:

- P(H1): Moderate under seasonal recharge; increases when piezometer time series show higher groundwater levels compared to historic seasonal trends.
- P(H2): Moderate–High during short-duration extreme rainfall events.
- P(H3): Low–Moderate, dependent on river discharge and toe protection measures.

Consequences (C):

- Infrastructure: Reactivation could damage piers/foundations and block access routes.

- Traffic: Possible platform collapse and extended motorway closure.
- Lives: Risk exposure linked to motorway users and maintenance crews.

Vulnerability (V):

- Structural: High if failure surfaces intersect viaduct foundations or approach fills; lower elsewhere. FEM back-analyses already applied residual strengths at sliding interfaces.
- Users: High if failure is sudden without warning; low with effective monitoring and traffic management.

Formally, risk can be expressed as:

$$R(DI)=P(H)\cdot P(S|H)\cdot P(T|S)\cdot V(L|T)$$

for loss of life, and

$$R(PD)=P(H)\cdot P(S|H)\cdot V(P|S)\cdot E$$

for property damage.

2) *Risk Assessment*

- H1: Moderate probability × High consequence → High Risk (deep-seated reactivation affecting critical linear infrastructure).
- H2: Moderate–High probability × Low–Medium consequence → Medium Risk (localized shallow failures).
- H3: Low–Moderate probability × Medium consequence → Medium Risk (toe erosion under flood conditions).

Evidence base includes: (i) geological/stratigraphic cross sections, (ii) regional landslide inventories, and (iii) piezometer time series.

3) Risk Management

Mitigation measures:

- Hydraulic control of slope: sub horizontal drains or drainage wells targeting piezometer depths (14–25 m) to reduce pore pressure; use thresholds on soggiacenza trends as early warning indicators.

- Buttressing and reprofiling in toe zones with reduced confinement, consistent with river reconfiguration works.
- Early warning system: rainfall thresholds (Jan–Apr cumulative) combined with piezometric thresholds (head approaching ground level). Automated piezometers (SC2, SC3, SE-series) already provide time-series data for such alarms.
- Exposure management: emergency plans to temporarily close the motorway when thresholds are exceeded; visual inspections of the riverbed post-floods.

Monitoring

- Maintain and repair sensors with malfunctioning signals (loss of transmission after 2020 noted in some piezometers).
- Establish baseline groundwater head levels for each piezometer and set action thresholds (e.g., 95th percentile of historical wet season levels + daily rate of rise).

Risk matrix for the Himera I slope

Scales used in this case (Table 10):

- Annual probability (P)
    - High: $>1\times10^{-1}$
    - Moderate: 1×10^{-2}–1×10^{-1}
    - Low: 1×10^{-3}–1×10^{-2}
    - Very low: 1×10^{-3}
- Consequence (C) (dominant impact across life, structure, service)
    - Minor (Mnr): negligible repairs, no injuries
    - Moderate (Mod): local repairs, short closure
    - Major (Maj): structural damage, long closure
    - Severe (Sev): collapse, casualties
- Vulnerability (V) (to the specific hazard) Low / Medium / High — combined into consequence where appropriate.
- Risk rating (R): qualitative combination of P × C, used with ALARP:
    - 🔴 Very High / High

- ○ 🟠 Medium
- ○ 🟡 Medium / Low
- ○ 🟢 Low

Table 10. *Summary risk matrix to guidelines for a risk assessment analysis.*

ID	Hazard (H)	Trigger(s) & conditions	P	C	Risk	Key receptors	Primary controls
H1	Deep-seated reactivation along debris–Flysch contact	Prolonged rainfall → pore-pressure rise (head approaching ground level in SC2/SC3/SE series). Possible toe softening near river.	Moderate	Major–Severe	High	Viaduct approaches/piles, traffic users	Sub-horizontal drains/relief wells; toe buttressing; rainfall–piezometer early-warning with traffic management
H2	Shallow slides / debris surges in colluvium	Short-duration high-intensity storms; saturated skins on steep facets	Moderate–High	Minor–Moderate	Medium	Platform/embankment slopes, site access	Surface drainage, berms, local mesh/vegetation, targeted surveillance during storms
H3	Toe erosion / loss of confinement by the F. Imera	River floods, thalweg shifts attacking toe	Low–Moderate	Moderate	Medium	Lower slope sector near river works	Bank protection, check of river works after floods, local buttressing if needed

Chapter eight

Conclusions and recommendations

8.1. Overview

This doctoral research has focused on the rainfall-induced instability of the Himera I slope through an integrated methodology that combined field evidence, advanced numerical modelling with PLAXIS 2D, and physical modelling by means of centrifuge tests. The study has demonstrated the effectiveness of combining different investigative approaches to unravel the complex hydro-mechanical processes that govern rainfall-triggered landslides in clayey slopes supporting linear infrastructure.

The conclusions obtained were the following:

1. The Himera I case represents a rainfall-induced landslide that affected a section of the A19 motorway viaduct in northern Sicily. From a geological standpoint, the slope is composed of clayey–silty deposits overlying weaker colluvial and alluvial strata, with significant lateral variability in stiffness and strength. Geotechnical investigations confirmed low effective cohesion and moderate friction angles, indicating materials with limited resistance under saturated conditions. The hydrogeological setting is strongly controlled by antecedent and triggering rainfall: a prolonged wetting phase in late winter increased pore water pressures and reduced matric suction in the surficial clayey deposits, while an intense rainfall window in early spring acted as the triggering factor, leading to full saturation and the loss of residual strength. Topographically, the left-hand slope sector exhibits steep gradients, berms, and a geometry prone to shallow instability mechanisms. The combined evidence demonstrates that the interaction of stratigraphy, hydrology, and morphology conditioned the failure

process, ultimately resulting in a shallow rotational–translational slide that displaced part of the slope toward the valley and damaged the motorway infrastructure.

2. The finite element analyses carried out with the Mohr–Coulomb constitutive model provided a consistent picture of a slope with very limited stability margin. The Mohr–Coulomb model was considered adequate for the aims of this research because the goal was to identify rainfall-induced triggering mechanisms and reproduce the global instability mode rather than simulate post-peak behaviour. More advanced constitutive models, while capable of capturing stiffness degradation, strain-softening, or stress-path dependency, require extensive laboratory datasets that were not available for Himera I. The ΣM_{sf}–$|u|$ curves obtained from c–φ reduction analyses revealed that the factor of safety stabilizes close to unity, rarely exceeding 1.2–1.3, and with rapid onset of plastic collapse. This finding confirms that the slope is in a condition of critical equilibrium, where even minor increments in pore water pressure can trigger instability. The fully coupled flow–deformation phases further illustrated that antecedent rainfall of moderate intensity over several weeks is sufficient to increase saturation levels and gradually diminish matric suction in the near-surface deposits. When followed by a shorter but more intense triggering rainfall event, the simulations reproduced a sharp rise in pore pressures, with the groundwater head advancing toward the slope surface and the active pore pressure field transitioning from negative to nearly zero. These hydro-mechanical changes are directly associated with the development of a shallow failure mechanism within the upper deposits.

3. The centrifuge modelling at 1:50 scale offered an independent line of validation. The physical model, tested under controlled rainfall conditions, reproduced displacement patterns highly consistent with the numerical results. The observed deformation sequence revealed

the progressive evolution of a rotational–translational slide, affecting the superficial orange clayey deposits and propagating downslope along the contact with the underlying softer stratum. Displacement vectors and surface measurements confirmed the gradual build-up of movements during antecedent wetting, culminating in acceleration and clear surface rupture during the triggering phase. The centrifuge tests not only supported the FEM interpretation but also provided valuable visual evidence of the timing and geometry of failure, complementing the purely computational perspective.

In addition, Figure 51 to Figure ***56*** illustrate the analysis of the slope surface profile at successive time intervals, where the contours were rescaled to quantify displacements corresponding to each increment of the g-level. The results clearly demonstrate that, as the g-level increases, the magnitude of displacements becomes progressively larger. This trend is particularly evident between times t_4 and t_5 under 15g, between t_6 and t_7 at 25g, and between t_8 and t_9 at 30g. Furthermore, Figure 57 not only presents the cumulative displacements in both the x- and y-directions, but also captures the overall kinematic behaviour of the slope, which was prematurely affected by the rainfall simulation. These results once again confirm that rainfall infiltration within the cohesive soil layer acted as the primary triggering mechanism of the landslide.

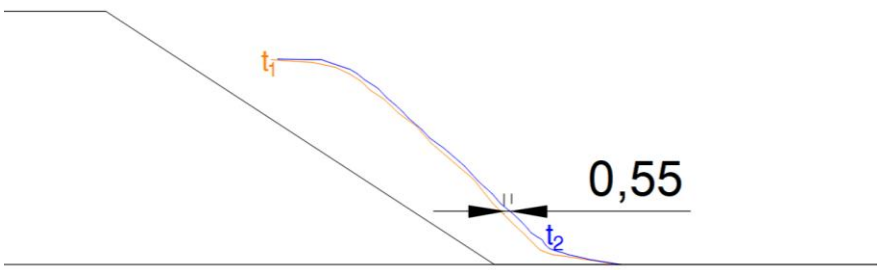

Figure 51. *Measured slope surface displacement between times t_1 and t_2, showing an accumulated downslope movement of 0.55 cm.*

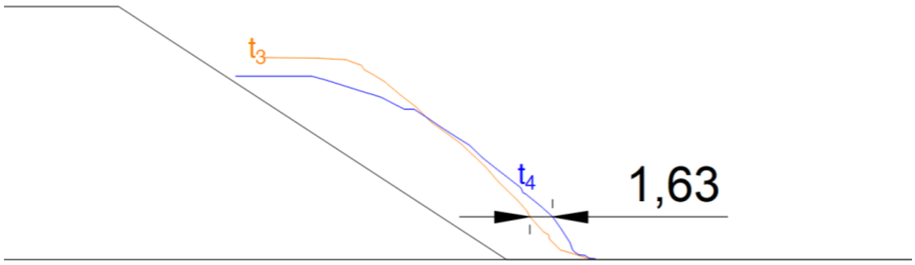

Figure 52. *Measured slope surface displacement between times t_3 and t_4, showing an accumulated downslope movement of 1.63 cm.*

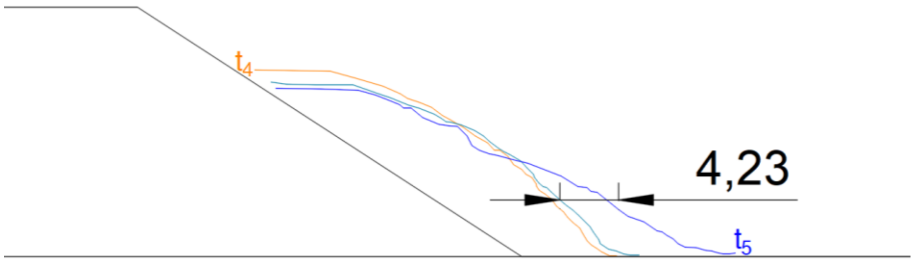

Figure 53. *Measured slope surface displacement between times t_4 and t_5, showing an accumulated downslope movement of 4.23 cm.*

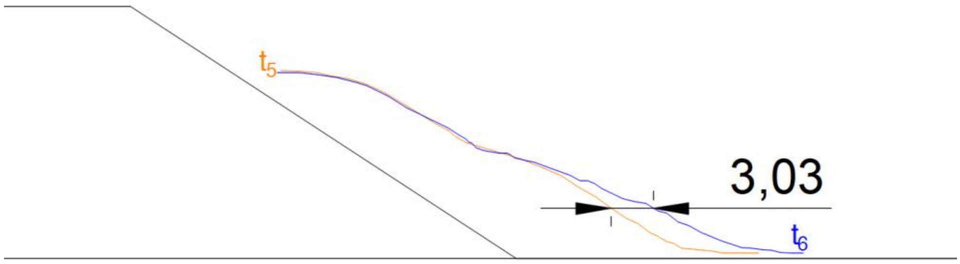

Figure 54. *Measured slope surface displacement between times t_5 and t_6, showing an accumulated downslope movement of 3.03 cm.*

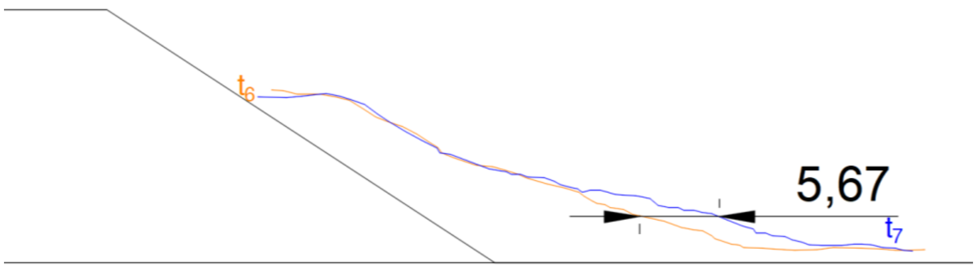

Figure 55. *Measured slope surface displacement between times t_6 and t_7, showing an accumulated downslope movement of 5.67 cm.*

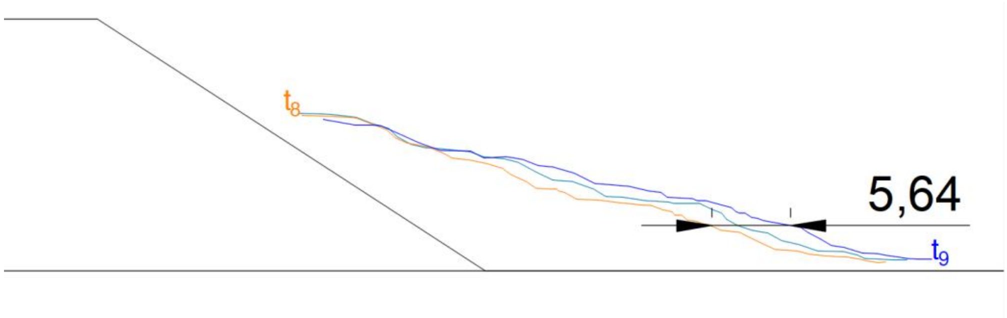

Figure 56. *Measured slope surface displacement between times t_8 and t_9, showing an accumulated downslope movement of 5.64 cm.*

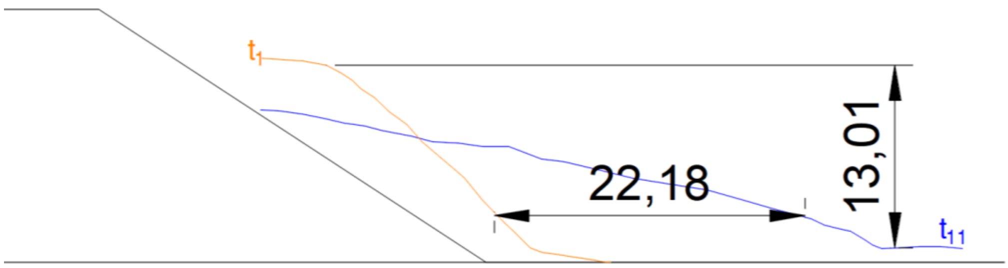

Figure 57. *Measured slope surface displacement between times t_1 and t_{11}, showing an accumulated downslope movement of 22.18 cm in x and 13 cm in y.*

4. The risk analysis carried out in this research underscores the importance of integrating geological, geotechnical and hydrological factors in the assessment of rainfall-induced landslide hazards. From a methodological perspective, the key steps include the identification of potential failure mechanisms, the quantification of triggering factors such as rainfall intensity and antecedent saturation, the estimation of slope safety margins through both empirical and numerical tools, and the evaluation of potential consequences for exposed assets. These elements form the backbone of a systematic risk assessment and provide a practical framework for students, engineers, and practitioners seeking to apply risk-based approaches to slope stability problems.
In the case of the Himera I slope, the risk analysis revealed that the factor of safety remained close to unity under normal conditions, implying an inherently marginally stable system. The rainfall scenarios, reconstructed from field data, demonstrated how sustained antecedent wetting followed by a short but intense

triggering event could rapidly reduce matric suction and elevate pore pressures, ultimately leading to slope failure. The exposure analysis highlighted the severe consequences of such failures when affecting linear infrastructures, in this case the A19 motorway viaduct, with direct impacts on regional connectivity and socio-economic costs.

Overall, the risk assessment confirmed that rainfall infiltration is the dominant hazard driver in this setting and that the consequences of failure are disproportionately high due to the strategic importance of the infrastructure involved. The Himera I case illustrates how combining probabilistic rainfall scenarios, coupled hydro-mechanical modelling, and consequence analysis can yield a holistic risk evaluation. These insights emphasize the necessity for proactive mitigation, such as drainage enhancement, continuous monitoring of pore pressures, and the incorporation of early warning systems. For students and practitioners, the Himera I study provides a reference example of how risk analysis can be operationalized in real-world cases, bridging the gap between theoretical frameworks and applied geotechnical engineering practice.

The integration of both approaches strengthens the conclusion that the Himera I landslide was primarily governed by rainfall infiltration rather than structural defects or seismic inputs. Both numerical simulations and centrifuge experiments converged in identifying the left-hand slope sector as the critical zone, with deformation patterns that closely match the actual landslide geometry documented in the field. The correspondence between physical and numerical observations lends credibility to the adopted modelling framework and enhances confidence in its application to other cases of rainfall-induced instability.

Overall, the thesis demonstrates that slopes with marginal stability (FS $\approx$ 1) can transition into failure rapidly when subjected to sustained rainfall infiltration, highlighting the fragility of natural and engineered slopes in similar geological settings. The results emphasize the importance of incorporating hydro-mechanical coupling in stability assessments, as well as the necessity of preventive drainage measures and continuous monitoring in infrastructure corridors exposed to intense or prolonged rainfall. The methodological framework developed—combining centrifuge testing with finite element back-analysis—represents a robust tool for understanding, predicting, and ultimately mitigating rainfall-induced landslides.

8.2. Recommendations and future work

The following is recommended:

1. A second test in the centrifuge would have included the installation of tensiometers at key locations where slope failure was observed, enabling a more detailed characterization of the failure mechanism and allowing for the establishment of correlations between displacements and suction under rainfall conditions, as the Figure 58 show the comparison with horizontal strain in upper weak-layered and homogeneous slopes in Wang et al.´s work (2010).

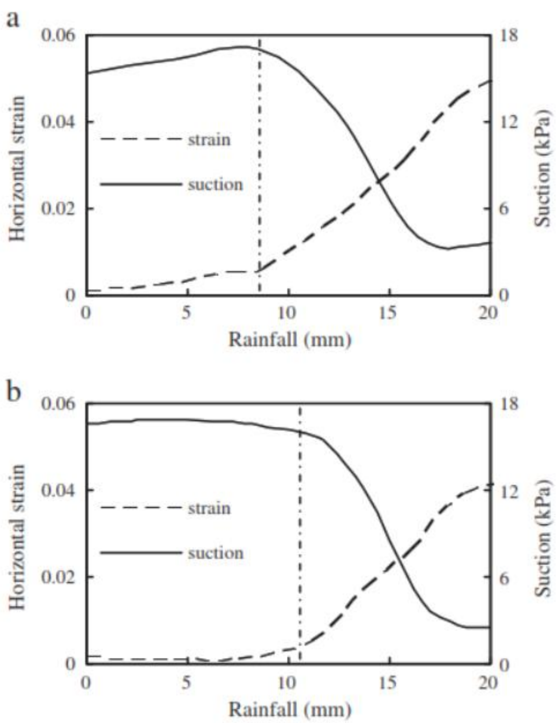

Figure 58. *Soil suction change in comparison with horizontal strain development in upper weak-layered and homogeneous slopes (Wang et al., 2010).*

2. With the rainfall equipment it is recommended to perform a calibration and future configurations. Prior to testing, intensities should be established by catch-tray mapping across the model footprint at the intended g-level(s), repeating for several pump pressures to build a calibration surface (pressure × g → prototype mm h^{-1}) following the procedures above (Whittle et al., 2012)(Fang et al., 2023). Although the central-outlet layout was adopted here for uniform coverage, the modular bolt-pattern permits alternative outlet geometries (e.g., staggered edge-focused or upslope-biased patterns). Exploring these layouts in future work would enable controlled non-uniform rainfall scenarios to study runoff concentration and preferential infiltration, which several authors identify as key to debris-flow initiation and shallow failure thresholds. Designs and evaluation methods in the cited nozzle/pressurized systems provide ready benchmarks for such experiments.

Reference

Abramson, L. W., Lee, T. S., Sharma, S., & Boyce, G. M. (2002). *Slope Stability and Stabilization Methods* (2nd ed.). Wiley. https://doi.org/10.1002/9780470172766

Aleotti, P., & Polloni, G. (2003). The Sarno debris-flow of May 1998: A disaster waiting to happen. In R. Casale & C. Margottini (Eds.), *Floods and landslides: Integrated risk assessment* (pp. 247–260). Springer. https://doi.org/10.1007/978-3-662-05201-3_18

Alger, C. S., & Brabb, E. E. (1985). *Bibliography of United States landslide maps and reports* (Issue Open-File Report 85-585). https://dggs.alaska.gov/pubs/id/11579

Al-Tabbaa, A., & Wood, D. M. (1989). An experimentally based 'bubble' model for clay. *Predictive Soil Mechanics*, 141–152.

Anbalagan, R., & Singh, B. (1996). Landslide hazard and risk assessment mapping of mountainous terrain: A case study from Kumaun Himalaya, India. *Engineering Geology*, *43*(4), 237–246. https://doi.org/10.1016/0013-7952(96)00026-7

Anderson, M. G., Lloyd, D. M., & Richards, K. S. (1996). Land surface–atmosphere interactions and their role in slope stability. *Geomorphology, 15*(1), 3–14. https://doi.org/10.1016/0169-555X(95)00112-J

Antoine, P. (1978). Glissements de terrains et aménagement de la montagne. *Bulletin de La Société Vaudoise Des Sciences Naturelles.*, *74*(353), 1–14.

Baecher, G. B. ., & Christian, J. T. . (2005). *Reliability and Statistics in Geotechnical Engineering*. John Wiley & Sons, Ltd.

Bentley Systems. (2016). *Groundwater flow analysis in PLAXIS – Brief overview (KB0108839)*.

Bentley Systems. (2017). *Safety analysis and displacements (SSR) (KB0110027)*.

Bentley Systems. (2018a). *Fully coupled flow–deformation analysis with staged construction (KB0110083)*.

Bentley Systems. (2018b). *PLAXIS 2D 2018: User Manual*. Bentley Systems. https://www.plaxis.com

Bentley Systems. (2019). *PLAXIS Dynamics manual (v20)*. Bentley Systems.

Bentley Systems. (2023). *PLAXIS 2D 2023: User Manual*. Bentley Systems. https://www.plaxis.com

Bentley Systems. (2024). *PLAXIS 2D datasheet*. Bentley Systems, Inc.

Bernknopf, R. L., Campbell, R. H., Brookshire, D. S., & Shapiro, C. D. (1988). A Probabilistic Approach to Landslide Hazard Mappin in Cincinatti, Ohio, with Applications for Economic Evaluation. . *Bulletin of the Assoc. of Eng. Geologists*, *25*(1).

Bertalot, D. (2013). *Behaviour of shallow foundations on layered soil deposits containing loose saturated sands during earthquakes*. University of Dundee.

Bertolo, P., & Wieczorek, G. F. (2005). Calibration of numerical models for small debris flows in Yosemite Valley, California, USA. *Natural Hazards and Earth System Sciences*, *5*(6), 993–1001. https://doi.org/https://doi.org/10.5194/nhess-5-993-2005, 2005.

Bhattacherjee, D., & Viswanadham, B. V. S. (2018). Development of a rainfall simulator in centrifuge using Modified Mariotte's principle. In *Physical Modelling in Geotechnics, Volume 1* (p. 6). CRC Press.

Bianchini, S., Ciampalini, A., Raspini, F., Bardi, F., Di Traglia, F., Moretti, S., & Casagli, N. (2015). Multi-Temporal Evaluation of Landslide Movements and Impacts on Buildings in San Fratello (Italy) By Means of C-Band and X-Band PSI Data. *Pure and Applied Geophysics*, *172*(11), 3043–3065. https://doi.org/10.1007/s00024-014-0839-2

Boniello, M. A., Capparelli, G., De Rosa, P., & Versace, P. (2010). A methodological approach for the definition of rainfall thresholds for the initiation of landslides. *Natural Hazards and Earth System Sciences*, *10*(4), 847–859. https://doi.org/10.5194/nhess-10-847-2010

Brabb, E. E. (1984). Innovative approaches to landslide hazard mapping. *Proceedings of the 4th International Symposium on Landslides*, *1*, 307–324.

Brabb, E. E., Pampeyan, E. H., & Bonilla, M. G. (1972). *Landslide susceptibility in San Mateo County, California (Map MF-360)*. U.S. Geological Survey. https://doi.org/10.3133/mf360

Brinkgreve, R. B. J., Engin, E., & Swolfs, W. M. (2010). *PLAXIS 2D AE user manual*. PLAXIS BV.

Brunetti, M. T., Peruccacci, S., Rossi, M., Luciani, S., Valigi, D., & Guzzetti, F. (2010). Rainfall thresholds for the possible occurrence of landslides in Italy. *Natural Hazards and Earth System Sciences*, *10*(3), 447–458. https://doi.org/10.5194/nhess-10-447-2010

Caine, N. (1980). The rainfall intensity–duration control of shallow landslides and debris flows. *Geografiska Annaler: Series A, Physical Geography*, *62*(1–2), 23–27. https://doi.org/10.1080/04353676.1980.11879996

Casagli, N., Frodella, W., Morelli, S., Tofani, V., Ciampalini, A., Intrieri, E., Raspini, F., Rossi, G., Tanteri, L., & Lu, P. (2017). Spaceborne, UAV and ground-based remote sensing techniques for landslide mapping, monitoring and early warning. *Geoenvironmental Disasters*, *4*, 9. https://doi.org/10.1186/s40677-017-0073-1

Cascini, L., Sorbino, G., Cuomo, S., & Ferlisi, S. (2008). Forecasting the occurrence of rainfall-induced shallow landslides of the flow-type: The case of Campania region (southern Italy). *Landslides*, *5*(3), 291–301. https://doi.org/10.1007/s10346-008-0113-9

Castelli, F., Castellano, E., Contino, F., & Lentini, V. (2016). A Web-based GIS system for landslide risk zonation: the case of Enna area (Italy). *Proceedings 12th International Symposium on Landslides*, *2*, 595–603.

Christian, J. T., Ladd, C. C., & Baecher, G. B. (1992). Reliability applied to slope stability analysis. *Journal of Geotechnical Engineering*, *118*(3), 577–596. https://doi.org/10.1061/(ASCE)0733-9410(1992)118:3(577)

Ciampalini, A., Cigna, F., Del Ventisette, C., Moretti, S., Liguori, V., & Casagli, N. (2012). Integrated geomorphological mapping in the north-western sector of Agrigento (Italy). *Journal of Maps*, *8*(2), 136–145. https://doi.org/10.1080/17445647.2012.680775

Cooper, M. A. R., & Robson, S. (1996). Theory of close-range photogrammetry. In K. B. Atkinson (Ed.), *Close Range Photogrammetry and Machine Vision*. Whittles.

Correa-Muñoz, N. A., & Higidio-Castro, J. F. (2017). Determination of landslide susceptibility in linear infrastructure. Case: Aqueduct network in Palacé, Popayan (Colombia). *Ingenieria e Investigacion*, *37*(2), 17–24. https://doi.org/10.15446/ing.investig.v37n2.59654

Craig, R. F. (2012). *Craig's Soil Mechanics* (8th ed.). Spon Press. https://doi.org/10.4324/9780203120990

Crosta, G. B., & Frattini, P. (2003). Distributed modelling of shallow landslides triggered by intense rainfall. *Natural Hazards and Earth System Sciences*, *3*(1–2), 81–93. https://doi.org/10.5194/nhess-3-81-2003

Cruden, D. (1996). Cruden,D.M., Varnes, D.J., 1996, Landslide Types and Processes, Special Report , Transportation Research Board, National Academy of Sciences, 247:36-75. *Special Report - National Research Council, Transportation Research Board*, *247*, 76.

Cruden, D. M., & Fell, R. (1997). *Landslide Risk Assessment* (D. M. Cruden & R. Fell, Eds.). A.A. Balkema Publishers.

Cruden, D. M., & Varnes, D. J. (1996). Landslide Types and Processes. In A. K. Turner & R. L. Schuster (Eds.), *Landslides: Investigation and Mitigation* (pp. 36–75). Transportation Research Board, National Research Council.

Davies, M. C. R., & Jones, A. M. (1998). Image acquisition using an on-board film camera. In T. Kimura, O. Kusakabe, & J. Takemura (Eds.), *Centrifuge 98: Proceedings of the International Conference Centrifuge 1998, Tokyo, Japan, 23–25 September 1998* (Vol. 1, pp. 55–61). A.A. Balkema.

Defae, A. H. A., & Knappett, J. A. (2014). Centrifuge modelling of the seismic performance of pile-reinforced slopes. *Journal of Geotechnical and Geoenvironmental Engineering*, *140*(2), 4013009. https://doi.org/10.1061/(ASCE)GT.1943-5606.0000991

Dumas, B., Guéremy, P., Lhenaff, R., & Raffy, T. (1984). Mouvements de Terrain et Risques Associés: Présentation d´un Essai Cartographique. Mouvements de Terrains. *Association Française de Géographie Physique.*, 161–171.

Duncan, J. M., & Wright, S. G. (2005). *Soil Strength and Slope Stability*. Wiley. https://doi.org/10.1002/0471479189

DUTI. (1985). *Détection et Utilisation des Terrains Instables*.

Einstein, H. H. (1988). Special lecture: Landslide risk assessment procedure. *5th International Symposium on Landslides*, 1075–1090.

Einstein, H. H. (1997). Landslide risk - Systematic approaches to assessment and management. In D. Cruden & R. Fell (Eds.), *Landslide Risk Assessment* (pp. 25–50).

Fang, Y., Take, W. A., Zhang, L., & Zhang, F. (2023). Centrifuge modelling of landslides and landslide hazard mitigation. *Geotechnical Frontiers 2023*. https://doi.org/10.1061/9780784484470.001

Fellenius, B. H. (2018). Development of axial pile load transfer curves based on instrumented load tests. *Journal of Geotechnical and Geoenvironmental Engineering*, *144*(2). https://doi.org/10.1061/(ASCE)GT.1943-5606.0001579

Fell, R. (1994). Landslide risk assessment and acceptable risk. *Canadian Geotechnical Journal*, *31*(2), 261–272. https://doi.org/10.1139/t94-031

Fell, R., & Hartford, D. (1997). Landslide risk management. In D. M. Cruden & R. Fell (Eds.), *Landslide Risk Assessment* (pp. 51–109).

Fredlund, D. G., & Rahardjo, H. (1993). *Soil Mechanics for Unsaturated Soils*. John Wiley & Sons.

Frodella, W., Ciampalini, A., Bardi, F., Salvatici, T., Di Traglia, F., Basile, G., & Casagli, N. (2018). A method for assessing and managing landslide residual hazard in urban areas. *Landslides*, *15*(2), 183–197. https://doi.org/10.1007/s10346-017-0875-y

Garnier, J., Gaudin, C., Springman, S., Culligan, P. J., Goodings, D., Konig, D., & Thorel, L. (2007). Catalogue of scaling laws and similitude questions in geotechnical centrifuge modelling. *International Journal of Physical Modelling in Geotechnics*, *7*(3), 1–23.

GeoEngineers. (n.d.). *Slope Stability — Single Free-Body Procedures*.

Gottardi, G., & Butterfield, R. (1993). The displacement of a model rigid footing on sand under general planar loading. *Géotechnique*, *43*(1), 79–93. https://doi.org/10.1680/geot.1993.43.1.79

Guzzetti, F. (2000). Landslide fatalities and the evaluation of landslide risk in Italy. *Engineering Geology*, *58*(2), 89–107. https://doi.org/10.1016/S0013-7952(00)00047-8

Guzzetti, F., Peruccacci, S., Rossi, M., & Stark, C. P. (2005). Rainfall thresholds for the initiation of landslides in central and southern Europe. *Meteorology and Atmospheric Physics*, *98*(3–4), 239–267. https://doi.org/10.1007/s00703-007-0262-7

Guzzetti, F., Peruccacci, S., Rossi, M., & Stark, C. P. (2008). The rainfall intensity–duration control of shallow landslides and debris flows: An update. *Landslides*, *5*(1), 3–17. https://doi.org/10.1007/s10346-007-0112-1

Hartlen, J., & Viberg, L. (1988). General report: Evaluation of slope stability—state of the art. *5th International Symposium on Landslides*.

Hudacsek, P., Take, W. A., Moore, J. R., & Viggiani, G. (2015). Centrifuge modelling of climatic effects on clay embankments. *Canadian Geotechnical Journal*, *52*(6), 727–741. https://doi.org/10.1139/cgj-2014-0111

Humbert, M. (1972). Les mouvements de Terrains. Principes de réalisation d´une carte prévisionelle dans les Alpes. *Bulletin Du B.R.G.M.*, *III*(1), 13–28.

Humbert, M. (1977). Le Castographie ZERMOS. Modalités et établissement des cartes des zones exposées á des riques liés aux mouvements du sol et du sous-sol. *Bulletin Du B.R.G.M.*, *III*(1/2), 5–8.

Hungr, O., Evans, S. G., Bovis, M. J., & Hutchinson, J. N. (2005). A review of the classification of landslides of the flow type. *Environmental and Engineering Geoscience*, *11*(3), 221–238. https://doi.org/10.2113/11.3.221

Ioannou, P. G. (1984). *The economic value of geologic exploration as a risk reduction strategy in underground construction* [Thesis (Ph.D.)]. institute of Technology.

Iverson, R. M. (2000). Landslide triggering by rain infiltration. *Water Resources Research*, *36*(7), 1897–1910. https://doi.org/10.1029/2000WR900090

Khan, A. Q. (2023). *Poster Presentation "The numerical evaluation of the mechanical contribution of plant roots to slope stability under rainfall infiltration."*

Kimura, T. ., Kusakabe, O. ., & Takemura, J. . (2000). *Centrifuge 98*. A A Balkema.

Kimura, T., Saito, A., & Takemura, J. (2010). Centrifuge model test on rainfall-induced slope failure in sandy soil. *Soils and Foundations*, *50*(4), 565–580. https://doi.org/10.3208/sandf.50.565

Knappett, J. A. (2010). *Physical modelling in geotechnics: Centrifuge techniques and scaling considerations*.

Krahn, J. (2004). *Stability Modeling with SLOPE/W: An Engineering Methodology*. GEO-SLOPE International Ltd.

Kutter, B. (1994). Recent advance in centrifuge modelling of seismic shaking. . *Proceeding of the International Conference on Recent Advance in Geotechnical Earthquake Engineering and Soil Dynamic*, 927–942.

Kutter, B. L. (2024). Fundamentals of centrifuge test. *International Conference on Physical Modelling in Geotechnics*.

Lauder, K. (2011). *The Performance of Pipeline Ploughs*. University of Dundee.

Lee, C., Ng, C. W. W., & Wang, Y. (2020). Development of a high-capacity rainfall simulator for centrifuge modelling of rainfall-induced landslides. *Géotechnique*, *70*(5), 443–454. https://doi.org/10.1680/jgeot.17.P.120

Lentini, V., Distefano, G., & Castelli, F. (2018). Consequence analyses induced by landslides along transport infrastructures in the Enna area (South Italy). *Bulletin of Engineering Geology and the Environment*. https://doi.org/10.1007/s10064-018-01360-0

Leonardi, G., Palamara, R., & Suraci, F. (2020). A fuzzy methodology to evaluate the landslide risk in road lifelines. *Transportation Research Procedia*, *45*, 732–739. https://doi.org/10.1016/j.trpro.2020.02.104

Leroi, E. (1996). Landslide risk assessment and acceptable risk. *Canadian Geotechnical Journal*, *33*(3), 361–371.

Lozińska-Stępień, H. (1979). Engineering geological maps at a scale 1:25 000 for regional planning purposes. *Bulletin of the International Association of Engineering Geology - Bulletin de l'Association Internationale de Géologie de l'Ingénieur*, *19*(1), 69–72. https://doi.org/10.1007/BF02600450

LPC. (1978). *Eboulements et chutes de pierres sur les routes. Méthode de Castographie.*

Lupini, J. F., Skinner, A. E., & Vaughan, P. R. (1981). The drained residual strength of cohesive soils. *Géotechnique*, *31*(2), 181–213. https://doi.org/10.1680/geot.1981.31.2.181

Malamud, B. D., Turcotte, D. L., Guzzetti, F., & Reichenbach, P. (2004). Landslide inventories and their statistical properties. *Earth Surface Processes and Landforms*, *29*(6), 687–711. https://doi.org/10.1002/esp.1064

Malgot, J., & Mahr, T. (1979). Engineering Geological Mapping of the West Carpathian Landslide Areas. *Bulletin of the International Association of Engineering Geologists*, *19*, 116–121.

Maugeri, M., & Motta, E. (2011). Effects of Heavy Rainfalls on Slope Behavior: The October 1, 2009 Disaster of Messina (Italy). In *Geotechnical, Geological and Earthquake Engineering* (Vol. 15, pp. 169–190). Springer. https://doi.org/10.1007/978-94-007-0470-1_10

Milne, F. D., Davies, M. C. R., Hamill, G. A., & Rea, H. (2011). Centrifuge modelling of hillslope debris flow initiation. *Catena*, *85*(2), 184–191. https://doi.org/10.1016/j.catena.2010.12.009

Montgomery, D. R., & Dietrich, W. E. (1994). A physically based model for the topographic control on shallow landsliding. *Water Resources Research*, *30*(4), 1153–1171. https://doi.org/10.1029/93WR02979

Morgan, G. C. (1991). Risk assessment for landslides. *Bulletin of the Association of Engineering Geologists*, *28*(1), 49–56.

Morgan, G. C., Rawlings, G. E., & Sobkowicz, J. C. (1992). Evaluating total risk to communities from large debris flows. *Proceedings of the Canadian Geotechnical Conference*, 397–404.

Morgenstern, N. R. (1991). Limitations of stability analysis in geotechnical practice. *Geotechnia*, *61*, 5–19.

Morgenstern, N. R. (1992). The evaluation of slope stability: A25 year perspective in stability and performance of slopes and embankments. *Geotech. Special Publication.*, *II*, 1–26.

Ng, C. W. W., & Shi, Q. (1998). Influence of rainfall intensity and duration on slope stability in unsaturated soils. *Quarterly Journal of Engineering Geology and Hydrogeology*, *31*(2), 105–113. https://doi.org/10.1144/GSL.QJEG.1998.31.P2.04

Ng, C. W. W., Zhan, L. T., Bao, C. G., Fredlund, D. G., & Gong, B. W. (2003). Performance of an unsaturated expansive soil slope subjected to artificial rainfall infiltration. *Géotechnique*, *53*(2), 143–157.

Nilsen, T. H., Wright, R. H., Vlasic, T. C., & Spangle, W. (1979). Relative Slope Stability and Land-use Planning in the San Francisco Bay Region. *U.S.G.S. Professional Paper*, *944*, 99.

Ou, C.-Y. (2006). *Deep Excavation: Theory and Practice*. Taylor & Francis. https://doi.org/10.1201/9781482288469

Ovesen, N. K. (1979). *Centrifuges in soil mechanics* (W. H. Craig, R. G. James, & A. N. Schofield, Eds.). A.A. Balkema.

Peng, J.-B., & Lu, Z.-Y. (2013). FLO-2D simulation of mudflow caused by the 2008 Wenchuan earthquake. *Natural Hazards*, *65*(2), 1393–1407. https://doi.org/10.1007/s11069-012-0419-2

Peng, T., & Lu, X. (2013). FLO-2D simulation of mudflow caused by the 1998 Sarno landslide, Italy. *Natural Hazards*, *65*(3), 1883–1905. https://doi.org/10.1007/s11069-012-0442-9

Petschko, H., Bell, R., Leopold, P., Heiss, G., & Glade, T. (2013). Landslide Inventories for Reliable Susceptibility Maps in Lower Austria. In C. Margottini, P. Canuti, & K. Sassa (Eds.), *Landslide Science and Practice: Landslide Inventory and Susceptibility and Hazard Zoning* (Vol. 1, pp. 281–286). Springer. https://doi.org/10.1007/978-3-642-31325-7_37

Pinargote, K. (2022). *Informe geotécnico del sector PC2: Evaluación de erosión, saturación y estabilidad de taludes.*

PLAXIS BV. (2004). *PLAXIS Scientific manual (v8)*. PLAXIS BV.

Potts, D. M., & Zdravkovi'c, L. (1999). *Finite Element Analysis in Geotechnical Engineering: Theory* (Vol. 1). Thomas Telford. https://doi.org/10.1680/feaiget.28036

Pradhan, A. M. S., Siddique, T., & others. (2022). Fully Coupled Flow-Deformation Modelling for Rainfall-Induced Landslides. *Landslides*, *19*, 551–567. https://doi.org/10.1007/s10346-021-01770-1

Radbruch-Hall, D. H., Colton, R. B., Davies, W. E., Lucchitta, I., Skipp, B. A., & Varnes, D. J. (1982). Landslide Overview Map of the Conterminous United States. *U.S. Geological Survey Professional Paper 1183*, 25.

Rahardjo, H., Rezaur, R. B., Lee, T. T., & Leong, E. C. (2005). Response of a residual soil slope to rainfall. *Canadian Geotechnical Journal*, *42*(2), 340–351. https://doi.org/10.1139/t04-101

Roberds, W. J., Ho, K., & Leung, K. W. (1997). An integrated methodology for risk assessment and risk management for development below potential natural terrain landslides. In D. Cruden & R. Fell (Eds.), *Landslide Risk Assessment* (pp. 333–346).

Schofield, A. N. (1980a). Cambridge Geotechnical Centrifuge Operations. *Géotechnique*, *30*(3), 227–268. https://doi.org/10.1680/geot.1980.30.3.227

Schofield, A. N. (1980b). Cambridge geotechnical centrifuge operations. *Géotechnique*, *30*(3), 227–268.

Schofield, A. N. (1981). Dynamic and earthquake geotechnical centrifuge modelling. *Proceeding of the International Conference on Recent Advance in Geotechnical Earthquake Engineering and Soil Dynamic*, 1081–1100.

Schuster, R. L., & Krizek, R. J. (1978). *Landslides, analysis and control* (R. L. Schuster & R. J. Krizek, Eds.). National Academy of Sciences.

Seed, H. B., & Idriss, I. M. (1982). *Ground motions and soil liquefaction during earthquakes*. Earthquake Engineering Research Institute.

Skempton, A. W. (1985). Residual strength of clays in landslides, folded strata and the laboratory. *Géotechnique*, *35*(1), 3–18. https://doi.org/10.1680/geot.1985.35.1.3

Soulé, J. M. (1980). Engineering-Geologic Mapping and Potential Geologic Hazards in Colorado. *Bulletin of the International Association of Engineering Geologist*, *21*, 121–130.

Springman, S. M., Laue, J., & Kienzler, P. (2001). Centrifuge modelling of slope instabilities. *Proceedings of the International Conference on Slope Stability*, 665–670.

Stewart, D. I. (1989). *Ground effects on in-situ walls in stiff clay*. University of Cambridge, Emmanuel College.

Take, W. A., & Bolton, M. D. (2002). Photographic measurement of deformation in geotechnical models using digital image analysis. *Canadian Geotechnical Journal*, *39*(5), 849–861.

Take, W. A., Bolton, M. D., Wong, P. C. P., & Yeung, F. J. (2004a). Evaluation of landslide triggering mechanisms in model fill slopes. *Landslides*, *1*(3), 173–184. https://doi.org/10.1007/s10346-004-0025-1

Take, W. A., Bolton, M. D., Wong, P. C. P., & Yeung, F. J. (2004b). Evaluation of landslide triggering mechanisms in model fill slopes. *Landslides*, *1*(3), 173–184.

Taylor, F., & Brabb, E. (1986). *Map showing the status of landslide inventory and susceptibility mapping in California.* .

Taylor, R. N. (1995). *Geotechnical centrifuge technology*. Blackie Academic & Professional.

Terzaghi, K., Peck, R. B., & Mesri, G. (1996). *Soil mechanics in engineering practice* (Inc. John Wiley and Sons, Ed.; 3rd ed). John Wiley and Sons, Inc.

Trigila, A. (2007). *Rapporto sulle frane in Italia: Il Progetto IFFI (Inventario dei Fenomeni Franosi in Italia)*. APAT, Agenzia per la Protezione dell'Ambiente e per i Servizi Tecnici.

Tsegaye, E. (2019). *Numerical Modelling of Rainfall-Induced Landslides Using Coupled Hydro-Mechanical Analysis*. Norwegian University of Science and Technology (NTNU).

UNESCO Working Party on World Landslide Inventory. (1993). A suggested method for describing the activity of a landslide. *Bulletin of the International Association of Engineering Geology*, *47*, 53–57.

UNESCO Working Party on World Landslide Inventory (WP/WLI). (1993). A suggested method for describing the activity of a landslide. *Bulletin of the International Association of Engineering Geology*, *47*, 53–57.

Vanmarcke, E. H., & Bohnenblust, H. (1982). *Risk-based decision analysis in dam safety*.

Varnes, D. J. (1978a). *Slope Movement Types and Processes*.

Varnes, D. J. (1978b). Slope Movement Types and Processes. In R. L. Schuster & R. J. Krizek (Eds.), *Landslides: Analysis and Control* (pp. 11–33). Transportation Research Board, National Research Council.

Varnes, D. J. (1984). *Landslide Hazard Zonation: A Review of Principles and Practice, Natural Hazards*.

Viberg, L. (1984). Landslide Risk Mapping in Soft Clays in Scandinavia and Canada. *IVth International Symposium on Landslides* , 325–348.

Wang, R., Zhang, G., Wang, G., & Tang, H. (2010). Centrifuge model tests on clay slopes with weak layers under rainfall conditions. *Applied Clay Science*, *50*(3), 386–394. https://doi.org/10.1016/j.clay.2010.08.011

Wang, S., & Idinger, G. (2021). A device for rainfall simulation in geotechnical centrifuges. *Acta Geotechnica*, *16*(4), 2887–2898. https://doi.org/10.1007/s11440-021-01186-w

Wang, Z., Zhang, W., Gao, X., Liu, H., & Böhlke, T. (2020). Stability analysis of soil slopes based on strain information. *Acta Geotechnica*, *15*(11), 3121–3134. https://doi.org/10.1007/s11440-020-00985-x

Whittle, A. J., Kovacevic, N., Davie, C. T., & O'Brien, A. S. (2012). Centrifuge modelling of rainfall-induced slope instability. *International Journal of Physical Modelling in Geotechnics*, *12*(3), 79–94. https://doi.org/10.1680/ijpmg.12.00009

Wieczorek, G. F. (1982). Map Showing Recently-Active and Dormant Landslides near La Honda, Central Santa Cruz Mountains, California, U.S. In *Misc. Field Studies.* . U.S. Government Printing Office.

Wieczorek, G. F. (1984). Preparing a Detailed Landslide-Inventory Map for Hazard Evaluation and Reduction. *Bulletin of the Association of Engineering Geologists*, *XXI*(3), 337–342.

Won, J., You, K., Jeong, S., & Kim, S. (2005). Coupled effects in stability analysis of pile–slope systems. *Computers and Geotechnics*, *32*(4), 304–315. https://doi.org/10.1016/j.compgeo.2005.02.006

Wood, D. Muir. (2004). *Geotechnical modelling*. Spon Press.

WU, C., WANG, Z. Z., GOH, S. H., & ZHANG, W. (2024). Comparing 2D and 3D slope stability in spatially variable soils using random finite-element method. *Computers and Geotechnics*, *170*, 106324. https://doi.org/10.1016/J.COMPGEO.2024.106324

Wu, T. H., Tang, W. H., & Einstein, H. H. (1996). Landslide hazard and risk assessment. In A. K. Turner & R. L. Schuster (Eds.), *Landslides: Investigation and mitigation* (pp. 106–120). National Academy Press.

Zienkiewicz, O. C., Taylor, R. L., & Fox, D. D. (2014). *The Finite Element Method: Its Basis and Fundamentals* (7th ed.). Butterworth-Heinemann. https://doi.org/10.1016/C2009-0-24909-9

Zienkiewicz, O. C., Taylor, R. L., & Zhu, J. Z. (2013). *The Finite Element Method: Its Basis and Fundamentals* (7th ed.). Butterworth-Heinemann. https://doi.org/10.1016/C2009-0-24909-9